nature COMMUNICATIONS

ARTICLE

Received 15 Jun 2016 | Accepted 27 Mar 2017 | Published 22 May 2017

DOI: 10.1038/ncomms15423 OPEN

Constraining climate sensitivity and continental versus seafloor weathering using an inverse geological carbon cycle model

Joshua Krissansen-Totton[1] & David C. Catling[1]

The relative influences of tectonics, continental weathering and seafloor weathering in controlling the geological carbon cycle are unknown. Here we develop a new carbon cycle model that explicitly captures the kinetics of seafloor weathering to investigate carbon fluxes and the evolution of atmospheric CO_2 and ocean pH since 100 Myr ago. We compare model outputs to proxy data, and rigorously constrain model parameters using Bayesian inverse methods. Assuming our forward model is an accurate representation of the carbon cycle, to fit proxies the temperature dependence of continental weathering must be weaker than commonly assumed. We find that 15–31 °C (1σ) surface warming is required to double the continental weathering flux, versus 3–10 °C in previous work. In addition, continental weatherability has increased 1.7–3.3 times since 100 Myr ago, demanding explanation by uplift and sea-level changes. The average Earth system climate sensitivity is $5.6^{+1.3}_{-1.2}$ K (1σ) per CO_2 doubling, which is notably higher than fast-feedback estimates. These conclusions are robust to assumptions about outgassing, modern fluxes and seafloor weathering kinetics.

[1] Department of Earth and Space Sciences/Astrobiology Program, University of Washington, Seattle, Washington 98195-1310, USA. Correspondence and requests for materials should be addressed to J.K.-T. (email: joshkt@uw.edu).

Determining what controls the geological carbon cycle is crucial for understanding climate stability, planetary habitability and the long-term consequences of anthropogenic carbon emissions. On long timescales, carbon inputs into the atmosphere–ocean system must balance outputs otherwise atmospheric CO_2 would be depleted leading to a runaway icehouse, or CO_2 would accumulate and become excessively abundant within 10–100 Myr ago (ref. 1). Thus, a negative feedback must stabilize the carbon cycle and global climate on geological timescales.

The carbonate–silicate weathering cycle described by Walker *et al.*[2] is widely believed to provide a negative feedback[3]. In this picture, climatic warming from abundant atmospheric CO_2 enhances silicate weathering and delivers more carbon to the ocean where it precipitates to form carbonate rocks. Conversely, climatic cooling due to low CO_2 reduces silicate weathering and dampens CO_2 drawdown. The temperature dependence of silicate weathering effectively provides a natural thermostat to stabilize climate[2].

Although the carbonate–silicate thermostat is now part of textbook Earth science[4], the link between global climate, CO_2 and silicate weathering rates is unclear. Gaillardet *et al.*[5] found no overall correlation between weathering rates and temperature on a global scale. Some regional field studies also fail to find a relationship[6]. Furthermore, strongly temperature-dependent continental weathering is argued to contradict the conventional interpretation of the Phanerozoic strontium isotope record[7]. Weatherability changes due to uplift, lithology and biology have all been proposed as alternative drivers of the carbon cycle[8–11]. Indeed, Walker[12] himself changed his opinion to suspecting greater sensitivity of weathering rate to the aforementioned factors than to CO_2. Some models of the Cenozoic carbon cycle also suggest sizeable weatherability changes for reproducing observed pCO_2 and carbon isotope histories[13].

However, weatherability changes alone do not provide a clear negative feedback to balance the carbon cycle. An alternative or complimentary negative feedback to continental silicate weathering is seafloor weathering[7,14–17]. Seafloor weathering occurs because seawater circulates through upper oceanic crust in low-temperature, off-axis hydrothermal systems. Reactions with basalt release calcium ions, which precipitates calcium carbonate within veins and pores of the oceanic crust[18,19]. If the rate of basalt dissolution and precipitation is linked—directly or indirectly—to the carbon content of the atmosphere–ocean system, then seafloor weathering could provide an important negative feedback.

Here it is useful to think in terms of carbonate alkalinity, $[HCO_3^-] + 2[CO_3^{2-}]$, which—neglecting the small contribution from weak acid anions and water dissociation products—must balance the sum of conservative cations minus conservative anions, $([Na^+] + 2[Mg^{2+}] + 2[Ca^{2+}] + [K^+] + \ldots - [Cl^-] - 2[SO_4^{2-}] - [Br^-] - \ldots)$. Thus, dissolution of basalt, which releases alkaline earth and alkali metal cations, generates carbonate alkalinity to neutralize the positive ions in solution. In other words, carbon speciation adjusts in response to the addition of conservative cations to ensure charge balance.

Caldeira[20] used simple geochemical models to show that the pH dependence of seafloor weathering is too weak to be an important carbon cycle feedback, concluding that continental weathering dominates. However, recent studies challenge this conclusion: Mesozoic-aged oceanic crust has substantially higher carbonate content compared to Cenozoic-aged cores[18], and this elevated carbonate content is due to enhanced Mesozoic carbonate precipitation and not carbonate accumulation later[21]. In addition, these seafloor carbonates can only be explained by alkalinity released from basalt dissolution; alkalinity released from continental weathering is insufficient[16]. Temperature-dependent seafloor weathering could explain both the observed change in seafloor carbonate abundance since the Mesozoic and the strontium isotope record[17]. These studies justify re-examining the importance of seafloor weathering in the global carbon cycle.

Previous attempts to incorporate seafloor weathering into carbon cycle models have produced conflicting results, and temperature dependencies are often omitted[7,20]. Brady and Gíslason[14] conducted experiments to find the pCO_2 dependence and temperature dependence of seafloor weathering rates, which they summarized as:

$$r_{\text{dissolution}} \propto (R_{CO_2})^{\mu} = \left(\frac{pCO_2}{pCO_2^{\text{mod}}}\right)^{\mu} \quad (1)$$

Here R_{CO_2} is the partial pressure of atmospheric CO_2 (pCO_2) relative to preindustrial modern ($pCO_2^{\text{mod}} = 280$ p.p.m.), $\mu = 0.23$ is the best-fit CO_2 dependence and $\mu = 0.32$ is the best-fit temperature dependence. This approximation, with varying values for μ, has been adopted in several subsequent models, which suggest that seafloor weathering was an important negative feedback during at least some of Earth's history[10,15,22].

Subsuming the pH dependence, temperature dependence and ocean chemistry dependence of seafloor weathering into a CO_2 dependence (such as equation (1)) is potentially problematic because it does not explicitly capture dissolution kinetics, and so the value for μ that combines the temperature, pH and ocean chemistry weathering dependencies must be either guessed or fitted (for example, ref. 15). Models such as GEOCARB and its various incarnations[3,23] similarly do not incorporate seafloor weathering accurately because they lack ocean chemistry. Some models attempt to capture dissolution kinetics. However, these models have highly simplified ocean chemistry[24], assume a constant temperature of dissolution[25] or do not reproduce the observed increase[17] in seafloor basalt dissolution[26].

Here we develop a new open source model for testing competing hypotheses about the global carbon cycle. Our model explicitly calculates ocean chemistry and includes pH-dependent and temperature-dependent kinetics based on laboratory and empirical studies. This is an improvement over previous models that subsumed pH dependence and temperature dependence into an overall indirect CO_2 dependence with an arbitrary functional relationship (equation (1)), or only considered pH dependence in isolation[20,25]. In addition, we use a new parameterization linking deep-ocean temperatures to surface temperatures, and thus seafloor weathering to climate. The Cenozoic (66–0 Myr ago) and Mesozoic (252–66 Myr ago) are particularly useful eras to model because of their relatively abundant proxy records of ocean composition and geochemistry. Thus, to validate our model, we apply it the last 100 Myr ago and compare model outputs with these proxies. We also use a Bayesian inversion to constrain model parameters quantitatively, including the temperature sensitivity of continental weathering, climate sensitivity, and continental weatherability changes. This approach makes minimal assumptions about carbon cycle processes. For instance, it is agnostic about whether Cretaceous outgassing was very high or comparable to present levels, and it allows for large changes in weatherability of both silicates and carbonates. Consequently, the novel probability distributions we obtain for parameters of interest are robust to model assumptions.

Results

Definition of parameters. We model the time evolution of the carbon cycle using two separate boxes representing the atmosphere–ocean and the pore-space in the seafloor (Fig. 1), loosely following Caldeira[20]. We track carbon and alkalinity

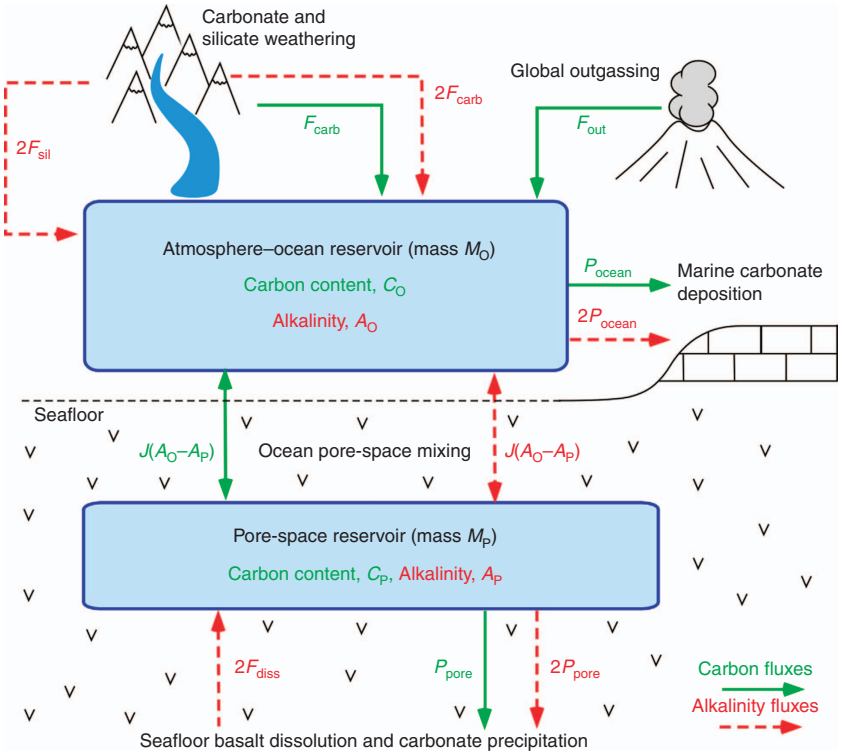

Figure 1 | Schematic representation of the box model used in this study. Carbon fluxes (Tmol C per year) are denoted by solid-green arrows, and alkalinity fluxes (Tmol eq per year) are denoted by red-dashed arrows. The fluxes into/out of the atmosphere–ocean are outgassing, F_{out}, silicate weathering, F_{sil}, carbonate weathering, F_{carb}, and marine carbonate precipitation, P_{ocean}. The fluxes into/out of the pore-space are basalt dissolution, F_{diss}, and pore-space carbonate precipitation, P_{pore}. Alkalinity fluxes are multiplied by two because the uptake or release of one mole of carbon as carbonate is balanced by a cation with a 2+ charge (typically Ca^{2+}). A constant mixing flux, J (kg per year), exchanges carbon and alkalinity between the atmosphere–ocean and pore-space.

fluxes into and between those boxes, and specify a constant mixing flux, J (kg per year) that determines how rapidly the ocean circulates through the pore-space. We assume that the bulk ocean is in equilibrium with the atmosphere. Consequently, our model is only appropriate for timescales greater than the mixing time of the ocean, ~1,000 years.

For many free parameters, we assume a range of values rather than point estimates. Model outputs are presented as distributions over this range of parameter values, which ensures that our results are robust to uncertainties in parameters, as described below. The dynamical equations, flux parameterizations and initial conditions are described in the methods section. Here we summarize the key points necessary to understand the results.

Following Walker *et al.*[2], the continental silicate weathering flux is expressed as:

$$F_{sil} = \omega F_{sil}^{mod} \left(\frac{pCO_2}{pCO_2^{mod}} \right)^{\alpha} \exp(\Delta T_S / T_e) \qquad (2)$$

Here $\Delta T_S = T_S - T_S^{mod}$ is the difference in global mean surface temperatures relative to preindustrial modern, $T_S^{mod} = 285$ K; ω is a dimensionless weatherability factor, F_{sil}^{mod} is the modern silicate weathering flux (Tmol per year) and α is an empirical constant (see Methods). An e-folding temperature, T_e, defines the temperature dependence of weathering, which can be related to an effective activation energy, E_a, as follows:

$$\frac{1}{T_e} \approx \frac{E_a}{RT_S^2} \qquad (3)$$

Here R is the universal gas constant.

In equation (2), we have combined both the direct kinetic temperature dependence and the temperature dependence of runoff in a single exponent. This is justifiable because an exponential kinetic dependence and a linear runoff dependence can be accurately approximated by an overall exponential (Supplementary Fig. 1). Walker *et al.*[2] also combine both effects to obtain an overall temperature dependence of $T_e = 13.7$ K, which corresponds to an effective activation energy of ~50 kJ mol^{-1}. Similarly, field measurements of chemical weathering fluxes from field studies suggest an activation energy of 74 ± 29 kJ mol^{-1} ($T_e = 9.1^{+5.9}_{-2.6}$K (ref. 27)). GEOCARB III effectively uses an overall e-folding temperature of T_e ~9.2 K, combining a direct temperature dependence and runoff coefficient[3]. We initially assume $T_e = 5$–15 K, but later consider a broader range because a weak temperature dependence turns out to be required.

The factor ω represents all so-called 'external' variables affecting weatherability and encompasses changes in land area due to sea-level variations, changes in lithology, relief, biology and palaeogeography. Rather than attempt to explicitly model these different influences (for example, ref. 23), we address the inverse problem: how much does ω have to change to fit proxy data? The simplest approach is to assume a linear change in weatherability since the mid-Cretaceous, as follows,

$$\omega = 1 + W(t/100\,\text{Myr}) \qquad (4)$$

and find W, the unknown change in weatherability. Here t is millions of years ago (Myr ago). We initially assume $W = 0$ to examine the range of possible model outputs for no external weatherability changes. Later, we assume $W = -0.8$ to 0.2, corresponding to mid-Cretaceous weatherability that was between 80% less or 20% greater than modern.

We adopt a parameterized climate model, whereby changes in surface temperature, ΔT_S, are logarithmically related to pCO_2, with corrections for solar luminosity evolution and palaeogeography (see Methods). The climate sensitivity parameter, ΔT_{2x}, has units of Kelvin warming per CO_2 doubling. The Intergovernmental Panel on Climate Change (IPCC)[28] estimated equilibrium climate sensitivity within the range 1.5–4.5 K. We assume $\Delta T_{2x} = 1.5$–8.0 K, which encompasses a broad range.

Approach and context. Parameterizations for carbon cycle processes are uncertain, so we adopted two statistical techniques to extract robust conclusions. First, we ran the forward model for the range of parameters and initial values shown in Tables 1 and 2. Each range was sampled as a uniform distribution, and the forward model was run 10,000 times to build distributions for the time series model outputs such as pCO_2, pH and temperatures. The resulting distributions represent the full range of possible model outcomes given assumed parameterizations and parameter ranges. These distributions were then compared to proxy data, typically binned into 10 Myr ago intervals with large, conservative error bars (Supplementary Methods).

The second approach solved the inverse problem with Markov Chain Monte Carlo (MCMC) techniques using the *emcee* package[29] in python (Supplementary Methods). Here the parameter ranges and initial value ranges define uniform priors (Table 1). A likelihood function describes the goodness-of-fit with proxy data, and the forward model was run 10 million times to obtain posterior probability distributions for the model parameters. The inverse solution gauges the full extent to which proxy data constrain the operation of the carbon cycle. In particular, parameters such as climate sensitivity, weatherability changes and the temperature dependence of silicate weathering can be constrained.

Forward modelling. The forward model was run 10,000 times, repeatedly sampling the parameter ranges of Table 1. First, weatherability was assumed constant ($W = 0$) and a range for the temperature dependence of silicate weathering typically assumed in the literature was adopted ($T_e = 5$–15 K). Figure 2 shows the modelled 90% confidence intervals plotted alongside proxy data. Clearly, the model with commonly assumed ranges for parameters does not fit the data. In particular, deep-ocean temperatures, surface temperatures and seafloor carbonate precipitation at 100 Myr ago are considerably lower than Cretaceous proxies (Fig. 2d,f). Fits with pH and ocean saturation state are also poor.

Next, the calculation was repeated using a weaker temperature dependence of silicate weathering, $T_e = 30$–40 K (Fig. 3). Here the 90% model uncertainty envelopes broadly encompass the proxy data, but the fit is marginal. The model pCO_2 output is consistent with pCO_2 proxies, and the temperature and seafloor precipitation distributions mostly overlap with proxy data error bars. Similarly, if we repeat the calculation a third time with the original temperature dependence of silicate weathering ($T_e = 5$–15 K), but include sizeable weatherability changes ($W = -0.6$ to -0.4, that is, weatherability at 100 Myr ago between 40 and 60% the modern value), then the model plausibly fits the data (Supplementary Fig. 2). Temperature, pCO_2 and precipitation proxies fall broadly within the model uncertainty envelope, although the fits with ocean pH and saturation state are still poor.

The best fit (Fig. 4) is obtained by assuming both weak temperature dependence of silicate weathering ($T_e = 30$–40 K) and a large weatherability change ($W = -0.6$ to -0.4). The median model output then fits temperature and precipitation proxies well, and pCO_2, ocean saturation state and pH all fall within proxy error bars.

From these results, we conclude that either the temperature dependence of silicate weathering is weaker than is commonly assumed, and/or that weatherability has approximately doubled since 100 Myr ago. When both are true, the model best fits the

Table 1 | Parameter ranges and Bayesian Markov Chain Monte Carlo inversion results.

Variable	Prior (uniform)	Nominal model			Michaelis–Menten law	
		Median posterior value	68% Credible interval ($1-\sigma$)	90% Credible interval	Median posterior value	90% Credible interval
CO_2 dependence, α^*	0.2–0.5	0.33	0.24–0.44	0.21–0.48	0.41	0.05–0.91
e-folding temp. dep. of cont. weathering, T_e (K)	5–50	34	22–45	17–48	31	14–48
Relative Cretaceous, weatherability, $1+W$	0.2–1.2	0.42	0.30–0.58	0.24–0.71	0.6	0.31–0.96
Climate sensitivity, ΔT_{2x} (K)	1.5–8.0	5.6	4.4–6.9	3.7–7.5	5.6	3.8–7.6
Relative Cretaceous outgassing, $1+V$	1.2–2.5	1.58	1.34–1.88	1.25–2.1	1.56	1.24–2.1
Carbonate weatherability modifier, $1+C_{WF}$	0.1–2.5	0.36	0.18–0.63	0.13–0.83	0.39	0.13–0.88
Modern outgassing, F_{out}^{mod} (Tmol C per year)	4–10	6.6	4.8–8.8	4.2–9.6	6.5	4.2–9.6
Modern carb. weathering, F_{carb}^{mod} (Tmol C per year)	7–14	11	8.2–12.9	7.4–13.7	11	7.4–13.7
Pore-space circulation time, τ (kyr)	20–1,000	570	239–847	100–949	555	88–945
Carbonate precip. coefficient, n	1.0–2.5	1.66	1.22–2.18	1.1–2.4	1.69	1.1–2.4
Modern seafloor dissolution relative to precipitation, $x^\dagger$	0.5–1.5	1.02	0.68–1.34	0.56–1.45	1.01	0.56–1.45
Surface-deep temp. gradient, a_{grad}	0.8–1.4	0.99	0.88–1.14	0.83–1.25	0.99	0.83–1.25
pH dependence seafloor, γ	0–0.5	0.27	0.11–0.43	0.04–0.48	0.27	0.04–0.48
Temp. dependence seafloor, E_{bas} (kJ mol^{-1})	40–110	75	53–97	45–106	76	45–106
Modern pelagic fraction, f_{PEL}	0.4–0.6	0.49	0.43–0.56	0.41–0.59	0.49	0.41–0.59
Spreading rate dep., β	0.0–1.0	0.47	0.15–0.82	0.05–0.94	0.49	0.05–0.95
Palaeogeography climate parameter, ΔP (K)	0.0–5.0	2.6	0.88–4.2	0.28–4.7	2.5	0.27–4.7

Column 1 shows the variables we wish to constrain using proxy data. Column 2 gives the uniform prior for each variable. These intervals also constitute the ranges assumed in the forward model analysis, unless stated otherwise. Columns 3–5 describe the posterior probability distributions for each variable for the nominal model. Columns 6–7 describe the posterior probability distributions for the modified model where the pCO_2 dependence of continental weathering is parameterized using the Michaelis–Menten law.
*For the Michaelis–Menten law, the prior for α is 0–1.0 (Supplementary Note 6), and so the posterior distribution is different to that of the nominal model.
†This constant defines the initial seafloor dissolution flux relative to the carbonate precipitation flux in the pore-space (see Table 2 for further details and formal definition).

Table 2 | Initial values or initial value ranges assumed in our model.

Variable	Initial value or initial range	References
Modern pore-space carbonate precipitation, P^{mod}_{pore} (Tmol C per year)	0.45*	[18] (see Supplementary Methods)
Modern seafloor dissolution, F^{mod}_{diss} (Tmol C per year)	0.225–0.675†	[16]
Modern outgassing, F^{mod}_{out} (Tmol C per year)	4–10	[23,76]
Modern carb. Weathering, F^{mod}_{carb} (Tmol C per year)	7–14	[77], their Table 2
Preindustrial mean surface temperature, T_S (K)	285	[2]
Modern ocean pH	8.2	[74]
Ocean Ca abundance (mMol kg^{-1})	10.03	Polynomial fit to Tyrrell and Zeebe[75], see Supplementary Fig. 8
Preindustrial atmospheric pCO_2 (p.p.m.)	280	—
Modern fraction pelagic precip. f_{PEL}	0.4–0.6	[78]

*Because we are adopting wide ranges for F^{mod}_{out} and F^{mod}_{carb}, it is unnecessary to include a range for P^{mod}_{pore} because its size relative to outgassing and weathering fluxes already encompasses a wide range (only the relative sizes of carbon cycle fluxes matter for predicting observable variables).
†Here we assume that $F^{mod}_{diss} = xP^{mod}_{pore}$, where $x = 0.5$–1.5. Coogan and Gillis[16] used a geochemical model of pore-space precipitation to show that at least 70% of pore-space precipitation is attributable to alkalinity release from basalt dissolution. Here we conservatively assume a lower limit of 50% instead. The upper limit is 150% to allow for the possibility that pore-space dissolution exceeds pore-space precipitation, and that the excess alkalinity is mixed into the ocean to form marine carbonates.

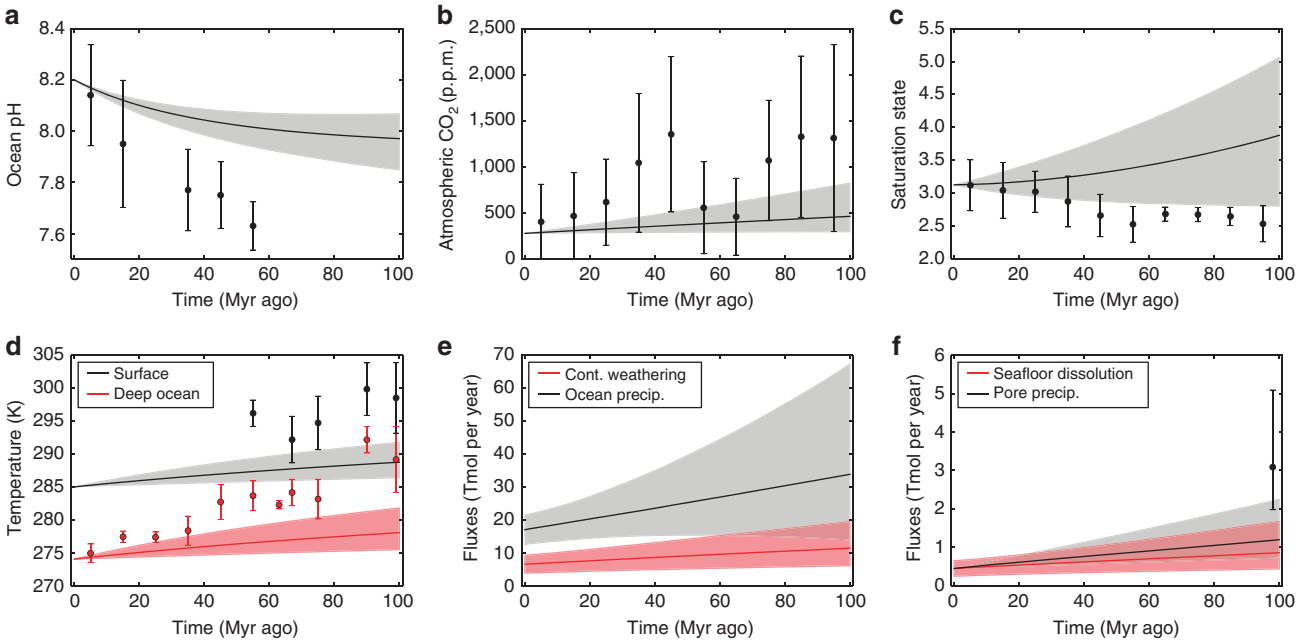

Figure 2 | Carbon cycle model with poor fit to data assuming conventional temperature dependence of continental weathering and no weatherability change. Selected model outputs and geochemical proxy data for a conventional temperature sensitivity range for continental weathering ($T_e = 5$–15 K), and no change in silicate weatherability over the last 100 Myr ago ($W = 0$). Grey- and red-shaded regions represent the model output 90% confidence obtained from 10,000 forward model runs using the parameter ranges described in Table 1. The grey- and red-solid lines are the median model outputs. Black and red dots represent binned geochemical proxy data, and error bars denote the range of binned proxy estimates (see main text for references and explanation). Panels denote (**a**) ocean pH, (**b**) atmospheric pCO_2, (**c**) ocean saturation state, (**d**) mean surface and deep ocean temperatures, (**e**) continental silicate weathering and ocean carbonate precipitation fluxes, and (**f**) seafloor dissolution and pore space carbonate precipitation fluxes. This case is a very poor fit to temperature and pH, and is a relatively poor fit to ocean saturation state and seafloor carbonate precipitation.

data. This result is robust to carbon cycle assumptions because the model distributions were calculated assuming the full parameter ranges in Table 1.

Bayesian MCMC inversion. The forward model results are qualitatively instructive, but Bayesian analysis allows more quantitative conclusions. MCMC techniques generated Fig. 5, which shows 95% credible intervals for the time evolution of carbon cycle variables. MCMC produces a much better fit than forward modelling because the algorithm converges to the maximum-likelihood region of parameter space. The distribution of model outcomes fits every proxy we considered within the 95% interval except one ocean pH data point. Distributions are also plotted for the relative and absolute change in seafloor dissolution, continental silicate weathering and continental carbonate weathering.

Figure 6 shows posterior probability distributions for selected model parameters, and Table 1 shows the best estimates for all parameters with uncertainty. To test the sensitivity of our results to weathering parameterizations, results are reported for both the nominal model (power-law pCO_2 dependence of continental weathering) and a Michaelis–Menten pCO_2 dependence law (Supplementary Note 6). For the nominal model, the temperature

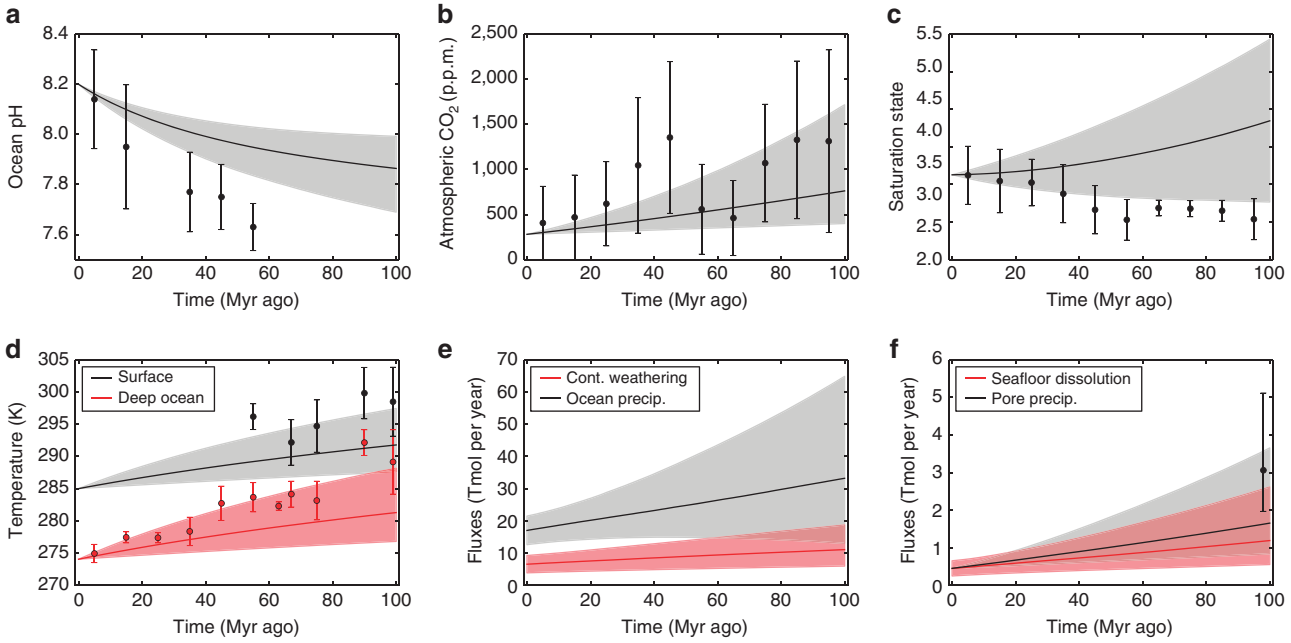

Figure 3 | Carbon cycle model with moderate fit to data assuming weak temperature dependence of continental weathering and no weatherability change. Selected model outputs and geochemical proxy data for a weak temperature dependence for continental weathering ($T_e = 30$–40 K) and no change in silicate weatherability over the last 100 Myr ago ($W = 0$). Grey- and red-shaded regions represent the model output 90% confidence obtained from 10,000 forward model runs using the parameter ranges described in Table 1. The grey- and red-solid lines are the median model outputs. Black and red dots represent binned geochemical proxy data, and error bars denote the range of binned proxy estimates (see main text for references and explanation). Panels denote (**a**) ocean pH, (**b**) atmospheric pCO_2, (**c**) ocean saturation state, (**d**) mean surface and deep ocean temperatures, (**e**) continental silicate weathering and ocean carbonate precipitation fluxes, and (**f**) seafloor dissolution and pore space carbonate precipitation fluxes. Here the model envelopes marginally encompass the proxy data. The upper end of the temperature and seafloor envelopes fit proxies, pCO_2 is an excellent fit, and the saturation state and ocean pH proxies are on the edge of the model envelope.

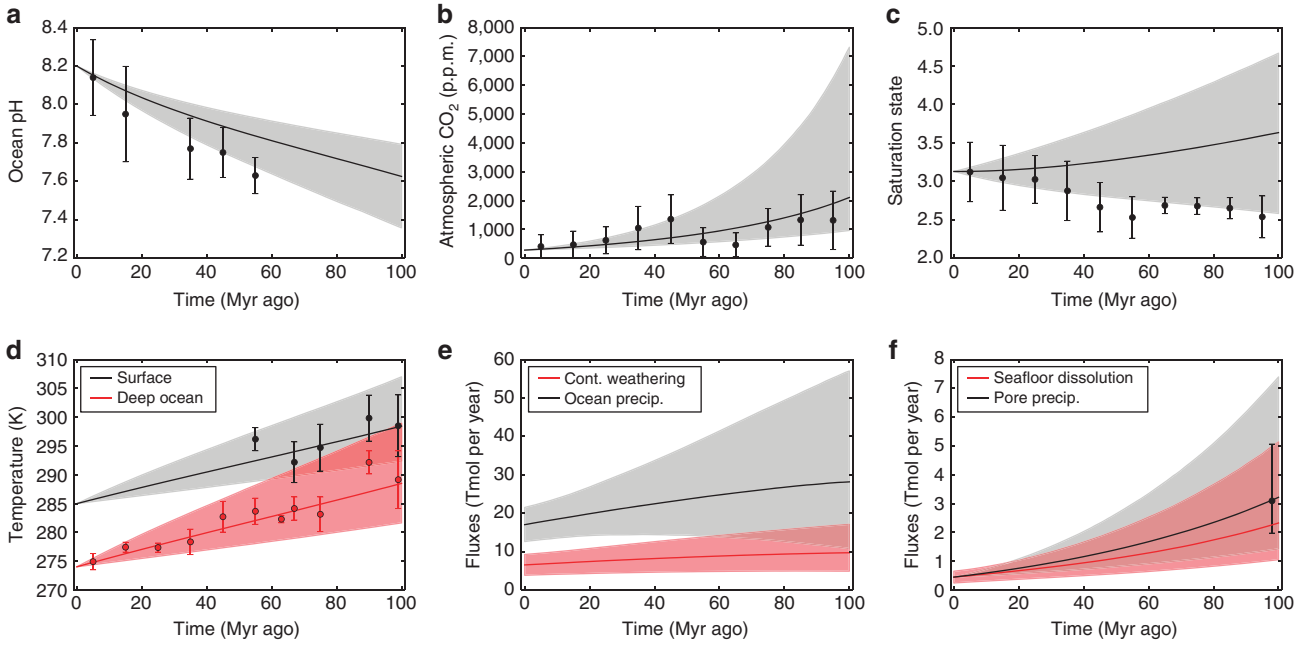

Figure 4 | Carbon cycle model with excellent fit to data assuming weak temperature dependence of continental weathering and a weatherability doubling since 100 Myr ago. Selected model outputs and geochemical proxy data for a weak temperature dependence for continental weathering ($T_e = 30$–40 K) and a 40–60% change in continental weatherability over the last 100 Myr ago ($W = -0.6$ to -0.4). Grey- and red-shaded regions represent the model output 90% confidence obtained from 10,000 forward model runs using the parameter ranges described in Table 1. The grey- and red-solid lines are the median model outputs. Black and red dots represent binned geochemical proxy data, and error bars denote the range of binned proxy estimates (see main text for references and explanation). Panels denote (**a**) ocean pH, (**b**) atmospheric pCO_2, (**c**) ocean saturation state, (**d**) mean surface and deep ocean temperatures, (**e**) continental silicate weathering and ocean carbonate precipitation fluxes, and (**f**) seafloor dissolution and pore space carbonate precipitation fluxes. Here the model envelopes are an excellent fit with proxy data. The median temperature and seafloor precipitation approximately coincide with geochemical proxies, and the saturation state, pH and pCO_2 envelopes all encompass their respective proxies.

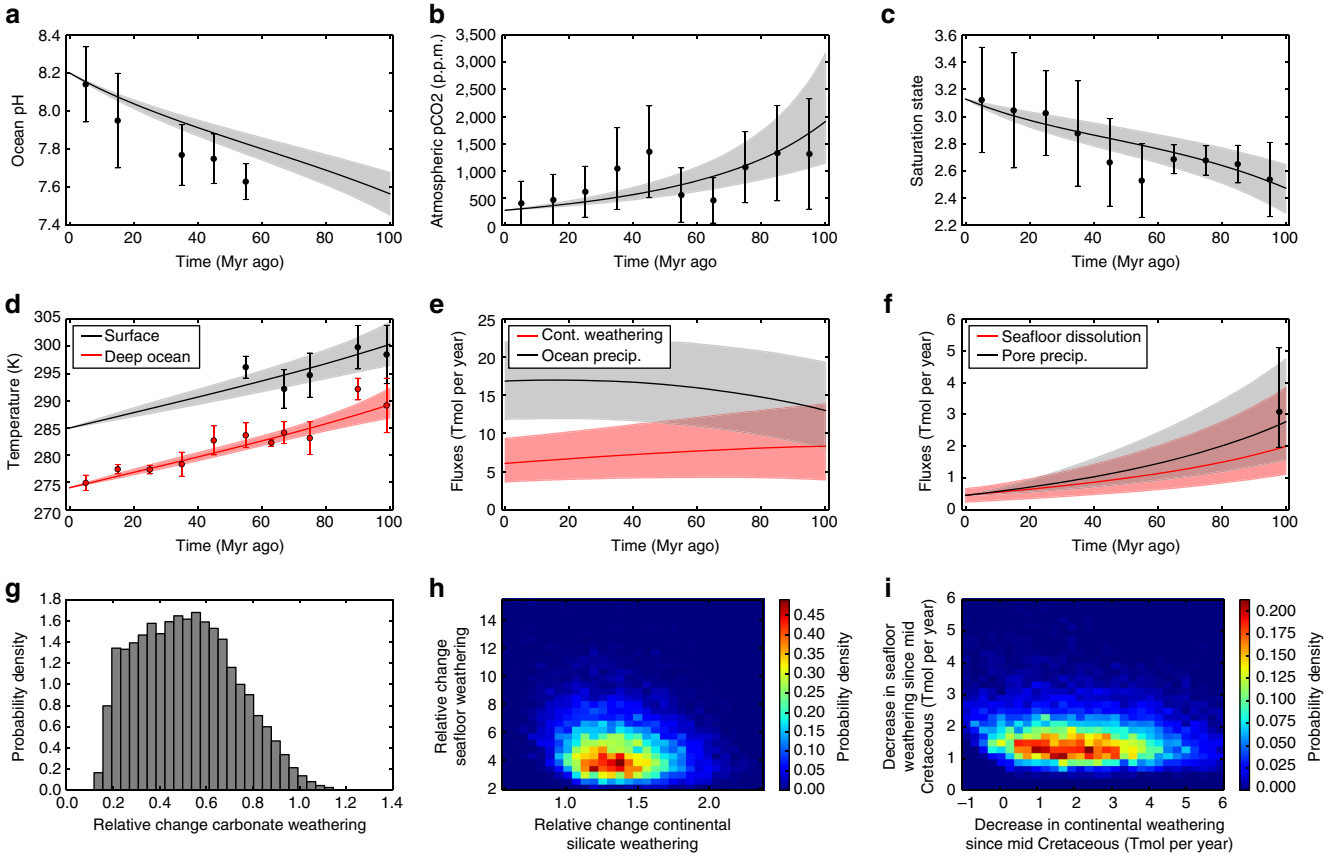

Figure 5 | Carbon cycle model fitted to data with Bayesian inverse analysis. Bayesian Markov Chain Monte Carlo (MCMC) results for the nominal model. (**a**–**f**) Grey- and red-shaded areas show 95% credible intervals for selected model outputs, and solid lines show median model outputs. Black and red circles are geochemical proxies, and error bars denote the range of binned proxy estimates (see main text). Note that the credible intervals encompass the Cretaceous proxies (within uncertainty) in almost all cases. (**g**–**i**) Probability distributions for the relative and absolute change in seafloor dissolution, continental silicate weathering and continental carbonate weathering. Relative changes refer to flux at 100 Myr ago relative to the modern flux.

dependence of silicate weathering is $T_e = 34^{+11}_{-11}$ K (1σ). This corresponds to a low effective activation energy of 20^{+10}_{-5} kJ mol^{-1} (1σ). Note that this effective activation energy incorporates all hydrological cycle feedbacks, not just the direct kinetic effect of temperature. Moreover, there is a 98% probability that $T_e \geq 15$ K ($E_a \leq 45$ kJ mol^{-1}). This suggests that the widely used range[2,3] of $T_e = 5$–15 K is incorrect. Intuitively, continental weathering must be weakly dependent on temperature because otherwise temperatures and pCO_2 would be too low, and ocean pH and saturation state values would be too high compared to geochemical proxies (Fig. 2).

The Bayesian inversion also implies that silicate weatherability in the Cretaceous was $42^{+16}_{-12}\%$ (1σ) of modern weatherability for the nominal model (Fig. 6). In addition, we can say there is a 95% probability that Cretaceous weatherability was $\leq 71\%$ of modern weatherability. This increase in weatherability is required in part because without it, Cretaceous silicate weathering would be too high to allow for the large observed seafloor weathering sink of carbon. But even if seafloor weathering is assumed to be negligible and removed from the likelihood function, then Cretaceous weatherability is $46^{+16}_{-13}\%$ modern weatherability. This small change is surprising because including seafloor weathering and its Cretaceous constraint effectively imposes a decreasing carbon sink, thereby allowing for a larger weatherability increase since 100 Myr ago and a weaker temperature sensitivity of continental weathering. However, the seafloor weathering sink is small compared to continental weathering, and so its omission only subtly affects the inversion. Instead, it is mostly temperature, pCO_2, pH and saturation state proxies that constrain the weatherability change.

The average equilibrium climate sensitivity over the last 100 Myr ago is constrained to $\Delta T_{2x} = 5.6^{+1.3}_{-1.2}$ K per CO_2 doubling (1σ) in the nominal model (Fig. 6). The 90% credible interval extends from 3.7 to 7.5 K, which is much higher than IPCC estimates. Low climate sensitivity is precluded by a lack of fit to pCO_2 and temperature proxies. The inverse analysis also suggests that Cretaceous outgassing was unlikely ($\sim$9% probability) to be greater than double modern outgassing to fit pCO_2 and temperature proxies.

In addition to the nominal model for continental weathering (equation (2)), we repeated the inverse analysis replacing the pCO_2 dependence of continental weathering with the Michaelis–Menten law:

$$F_{sil} = \omega F_{sil}^{mod} \left(\frac{2R_{CO_2}}{1 + R_{CO_2}} \right)^{\alpha} \exp(\Delta T_S / T_e) \qquad (5)$$

Using this modified parameterization, the results described above are largely unchanged (column 2, Fig. 6). The biggest difference between the two models is that the weatherability change required since 100 Myr ago is likely more modest under the Michaelis–Menten law than the nominal model, with a median Cretaceous value of 0.6 rather than 0.42.

Figure 5h shows the joint probability distribution for the relative change in continental silicate and seafloor weathering. We see the relative change in seafloor basalt dissolution at 100 Myr

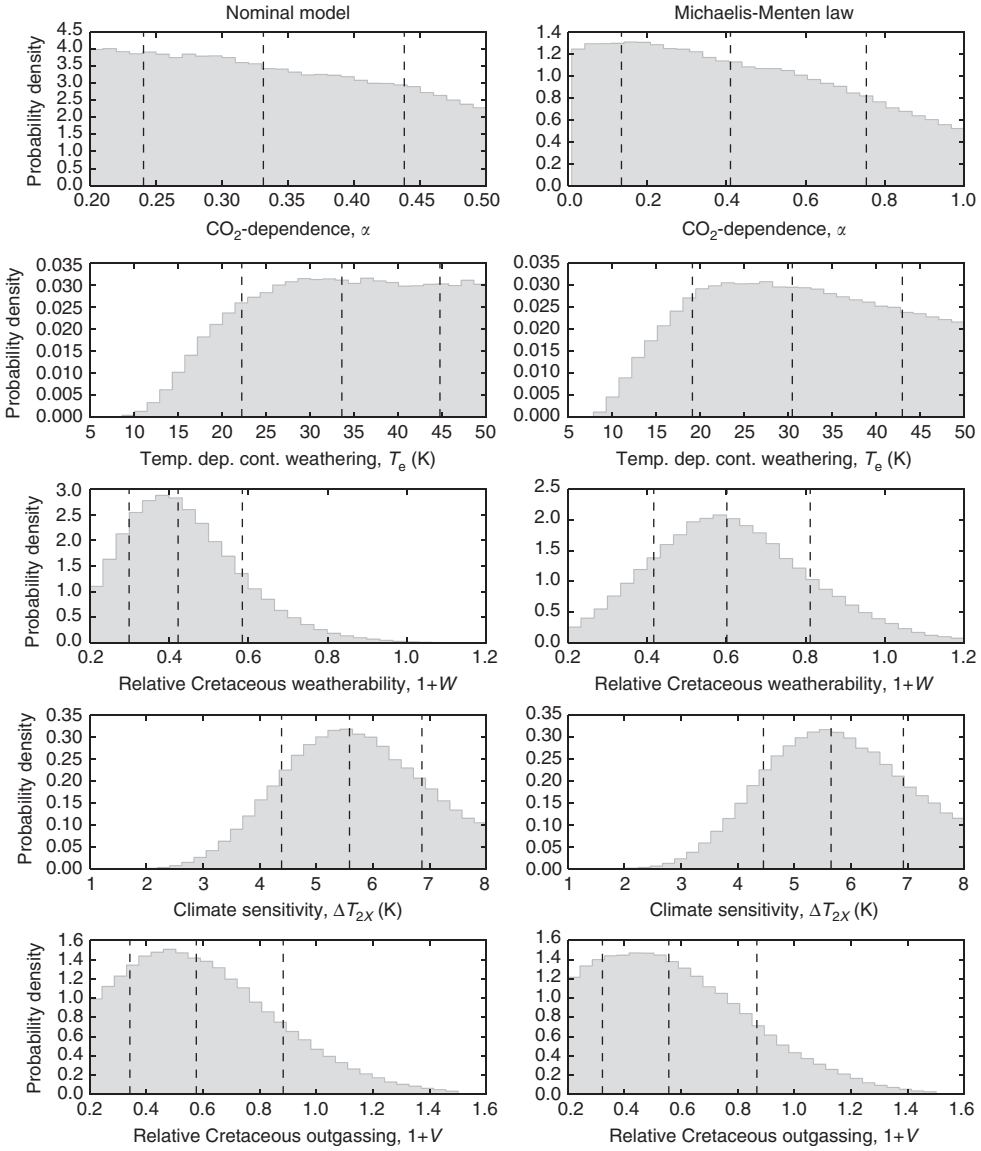

Figure 6 | Posterior probability distributions for selected carbon cycle variables from Bayesian inverse analysis. The first column is the posterior distributions from our nominal model, whereas the second column is distributions from a modified model, where the Michaelis–Menten law is used to describe the pCO_2 dependence of continental weathering. Results for the two parameterizations are similar. Dotted lines represent the median value with 1σ error bars. From the marginal distributions, we conclude that the temperature sensitivity of continental weathering is weak ($T_e > 15$ K), Cretaceous silicate weatherability ($1+W$) was $\sim$half modern weatherability, and the average equilibrium climate sensitivity is $\sim$5.6 K for a CO_2 doubling.

ago is much larger (2.6–9.2x modern, 95% credible interval) than the relative change in continental silicate weathering (0.91–1.9x modern flux, 95% credible interval). We also observe that the continental weathering flux is probably greater than the seafloor weathering flux since 100 Myr ago (Fig. 5e,f). However, we cannot say whether the absolute change in the continental weathering sink is greater than the absolute change in the seafloor weathering sink (Fig. 5i). The carbonate weathering flux at 100 Myr ago was 18–94% the modern flux (95% credible interval, shown in Fig. 5g).

Supplementary Fig. 4 shows posterior probability distributions for variables that can only be tentatively constrained. For example, the retrieval suggests the gradient relating deep-ocean temperatures to surface temperature, a_{grad} (see equation (12)), is $0.99^{+0.15}_{-0.12}$ (1σ), consistent with the linear regression in Fig. 8 (see Methods). The timescale for one ocean volume to circulate through the pore-space is $\sim$0.6 Myr, which suggests extremely short circulation times (for example, ref. 30) are unlikely, but not excluded. The effective activation energy for seafloor basalt dissolution is probably between 53 and 97 kJ mol^{-1} (1σ), in agreement with the 92 ± 7 kJ mol^{-1} value derived by Coogan and Dosso[17], and consistent with the range reported in field studies[31]. The median value of our posterior distribution is considerably higher than experimentally derived activation energies[14], perhaps suggesting that short-term experiments do not accurately capture temperature dependence on geological timescales, although our posterior distribution is sufficiently broad that these experimental activation energies cannot be excluded. Supplementary Fig. 5 shows probability distributions for the remaining variables, which are all unconstrained (flat posterior distributions).

Bayesian analysis sensitivity tests. Error bars for geochemical proxies might underestimate the true uncertainties, so how robust are our results to different proxies? The large weatherability change and weak temperature dependence of continental

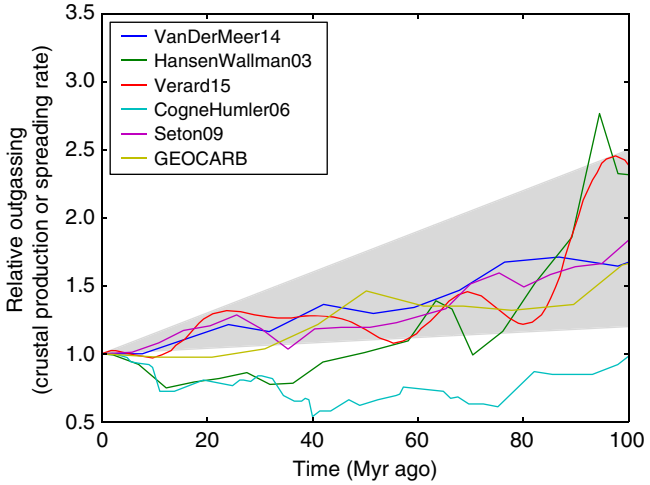

Figure 7 | Global outgassing reconstructions. Reconstructions of crustal production rates or spreading rates, relative to modern. These histories are assumed to reflect global outgassing histories. The studies listed in the legend are given in Supplementary Note 7. The grey region is the range of outgassing histories explored in our model.

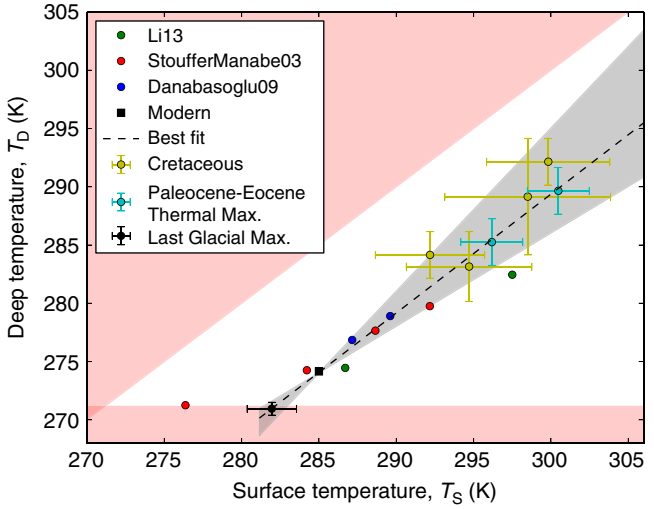

Figure 8 | Linear relationship between global mean surface temperature and deep-ocean temperature. Empirical relationship between deep-ocean temperatures and global mean surface temperatures, as determined by Global Circulation Model (GCM) outputs from the literature (coloured circles) and proxy data (coloured circles with error bars). The red regions are unphysical because the ocean is frozen or the deep ocean is warmer than the surface. The dotted line is the best fit to the proxies, $T_D = 1.02T_S - 16.67$, and the grey-shaded region is the range of T_D-T_S relationships considered in our model. See Supplementary Note 1 for full references, estimation of error bars, and further explanation.

weathering implied by our analysis do not depend on any single proxy. If the inverse analysis is repeated with the temperature, CO_2, pH, saturation state or seafloor weathering constraints individually omitted (equivalent to assuming we have no knowledge of these variables), then the posterior distributions for T_e and $1+W$ are largely unchanged (not shown). In fact, even if any two of those constraints are simultaneously omitted, the conclusions are unchanged. The posterior distributions for T_e and $1+W$ flatten only when three or more proxies are omitted.

In contrast, climate sensitivity results are less robust to proxies. If temperature constraints are omitted from the Bayesian analysis, then climate sensitivity is constrained to $\Delta T_{2x} = 4.5^{+2.1}_{-1.9}$ K, whereas if CO_2 constraints are omitted, then $\Delta T_{2x} = 3.7^{+1.5}_{-1.0}$ K. When both temperature and CO_2 proxy constraints are omitted, the posterior distribution for climate sensitivity becomes approximately flat. Thus, our conclusions regarding climate sensitivity are closely tied to temperature and pCO_2 proxies, as one might expect.

Discussion

Four important findings emerge. First, the e-folding temperature of continental weathering lies between 17 and 48 K (90% credible) compared to the generally assumed 5–15 K. Weak temperature sensitivity of continental weathering has been suggested in previous studies of the Cenozoic and Mesozoic[32], but here we have rigorously constrained the temperature dependence.

While laboratory experiments on silicate weathering show a strong temperature dependence, it is difficult to isolate the temperature dependence in field studies because temperature covaries with other variables that modulate weathering such as precipitation, vegetation, prior soil development and cation leaching[33]. In addition, the global silicate weathering flux is mixture of transport-limited and kinetically limited regimes, and so extrapolating from field studies to a global temperature dependence is challenging. Nonetheless, a growing literature shows weak correlation between silicate weathering rates and temperature and precipitation, but strong correlation with physical erosion, which is controlled by tectonic uplift[34–37]. In addition, reactive transport modelling reveals that weathering of granitic landscapes is mostly controlled by hydrological transport, not kinetics[38]. Hydrological modelling shows that the response of global silicate weathering rates to changes in temperature depends strongly on uplift, and that the overall temperature dependence is dominated by a weak, indirect runoff dependence[8].

Riebe *et al.*[39] used cosmonucleotides and mass balance arguments to infer long-term weathering rates for 42 diverse granitic landscapes. They found silicate weathering is predominantly transport limited, with an effective activation energy of only 14–24 kJ mol^{-1} (T_e = 28–48 K), consistent with our MCMC inversion. Our results thus support the notion that weathering is predominantly transport limited.

On long timescales, runoff rates could modulate erosion, so it is challenging to isolate climatic effects[5,40]. Nonetheless, a weaker silicate weathering feedback might suggest larger swings in temperature over Earth history, though extremes will be dampened by strongly temperature-dependent seafloor weathering and the direct CO_2 dependence of continental weathering.

The second important finding is that silicate rock weatherability at 100 Myr ago was considerably lower than the modern. Kump and Arthur[13] inferred Cenozoic weatherability through time by forcing a carbon cycle model with crustal production, exposed land area and organic burial from proxies. They found that to fit pCO_2 proxies, weatherability as defined here must increase by $\sim$0.3 over the Cenozoic, or equivalently, $1+W = 0.53$ by linear extrapolation. In this study, the 1σ interval for $1+W$ extends from 0.3 to 0.58. Caves *et al.*[41] also calculated the time evolution of weatherability across the Cenozoic and found a secular increase consistent with this study.

Of several possible explanations for weatherability increases, most obviously, mid-Cretaceous sea-level was 85–270 m higher than today[42]. This implies that the continental land area was 10–27% less than modern (Fig. 3.3 in ref. 43). However, given that weatherability may be weaker than linearly related to area[23] and the posterior distribution for the weatherability change (Fig. 6), it is unlikely that sea-level variation alone can account for the required change in weatherability over the last 100 Myr ago.

Weatherability can also increase with continental relief. Greater uplift may result in more physical erosion and enhanced chemical weathering[8,9]. If mid-Cretaceous relief was considerably lower than modern relief, this could explain the required change in weatherability. Berner[23] used $^{87}Sr/^{86}Sr$ ratios and terrigeneous sediment abundances to conclude that continental relief in the mid-Cretaceous was ~60–80% modern (Fig. 2.2 in ref. 23). However, the conventional interpretation of the Sr isotope record has recently been challenged[17,44]. In particular, the Cenozoic $^{87}Sr/^{86}Sr$ record can be reproduced by a simple model of temperature-dependent seafloor weathering so that no changes in continental weatherability are required[17]. Nonetheless, if these nominal changes in relief are accepted, then the combined change in weatherability from sea-level variation and reduced uplift is 0.44–0.72, which could easily explain the weatherability change inferred from our Bayesian analysis.

Changes in lithology, palaeogeography and biology also have an impact on weatherability. Basaltic weathering contributes one-third of the global silicate weathering flux despite only constituting ~10% of the global silicate area[45]. Reconstructions of basaltic area through time vary by methodology[46,47], but recent analyses suggest a basaltic area at 100 Myr ago approximately double the modern area[10], seemingly implying that silicate weatherability was ~30% greater than today. This change has opposite sign to the change implied by our retrieval, suggesting that either the increase in relief since 100 Myr ago compensated for lithology changes, or basaltic weatherability has been overestimated[48]. Palaeogeography changes are one of the primary controls on weathering for much of the Phanerozoic[49], but for the last 100 Myr ago the effect of palaeogeography on weathering fluxes has been relatively muted (Fig. 8 in ref. 49 and Fig. 4 in ref. 50). Biologically mediated changes in weatherability due to the proliferation of angiosperms[51] or the emergence of ectomycorrhizal fungi[11] could also have contributed to the weatherability increase. However, both biological innovations occurred around 100 Myr ago, suggesting that they may not be important for the relevant time span. Consequently, the most probable contributors to the required increase in weatherability over the last 100 Myr ago are lower sea levels and enhanced uplift.

Our third key finding is that average Earth system climate sensitivity since 100 Myr ago is 3.7–7.5 K for a doubling of pCO_2 (90% credible), which is much larger than the IPCC[28] range, 1.5–4.5 K. Our result is broadly consistent with previous estimates of Earth system climate sensitivity based on palaeoclimate data[52,53], and supports the view that the long-term climate sensitivity of the Earth system is greater than the fast-feedback Charnay sensitivity captured by Global Circulation Models (GCMs). In addition, high climate sensitivity could help explain why extremely high pCO_2 (for example, 4,000 p.p.m.) levels are required to reproduce observed Cretaceous equator-to-pole temperature gradients in GCMs[54].

A caveat is that we have neglected other greenhouse gases (GHGs), which could lead to overestimating climate sensitivity. Indeed, Earth system models suggest that other GHGs may have contributed significantly (2–3 K) to Cretaceous and Eocene warmth[55]. However, this increase in GHG abundances is largely a vegetation response to warmer temperatures, and GHG feedbacks such as this are already implicitly captured in our overall pCO_2-dependent climate sensitivity. In principle, the omission of methane forcings could affect our results, but the changes in methane flux would have to be substantial to reduce our inferred climate sensitivity. The warming from other GHGs is only ~0.5 K from changes in boundary conditions between the Early Eocene and Late Cretaceous[55].

Fourth, although the continental weathering flux was probably larger than the seafloor weathering flux since 100 Myr ago (Fig. 5e,f), it is difficult to directly compare the importance of the two feedbacks. The temperature dependence of continental weathering is likely weak, but both the temperature dependence of seafloor weathering and the direct pCO_2 dependence of continental weathering are poorly constrained (Fig. 6; Supplementary Fig. 4). Consequently, we cannot say whether the absolute change in continental weathering since 100 Myr ago is greater or less than the change in seafloor weathering (Fig. 5i). In addition, conclusions regarding low-temperature sensitivity of continental weathering, weatherability changes and climate sensitivity hold irrespective of assumptions about seafloor weathering; these conclusions arise primarily from the fit to temperature, pCO_2, saturation state and pH proxies.

With that said, the temperature dependence of continental weathering ($E_a = 20^{+10}_{-5}$ kJ mol^{-1}) is weak compared to seafloor weathering ($E_{bas} = 75^{+22}_{-21}$ kJ mol^{-1}), and a secular decline in spreading rates over Earth history would imply more dominant seafloor weathering fluxes at earlier times since continental weathering has no direct spreading rate dependence. Taken together, these observations suggest that seafloor weathering feedback may have been an important feedback at earlier times in Earth's history.

All of our conclusions—to varying degrees—depend on the fidelity of proxies. We have attempted to minimize this source of error by adopting the broadest possible range of proxy estimates for pCO_2, temperature, saturation state, pH and the seafloor weathering sink (see Methods). The sensitivity analysis in the results section shows that the low-temperature sensitivity of continental weathering and the large weatherability increase since 100 Myr ago are robust. Even if current estimates of two proxies are highly uncertain or flawed, the remaining proxies tell a mutually consistent story on continental weathering. However, the same is not true for climate sensitivity. If proxies overestimate global mean temperatures in the Cretaceous, then Earth system climate sensitivity may be lower than our inverse analysis suggests. The same is true if real Cretaceous pCO_2 was much higher than proxy estimates.

To some extent, conclusions are sensitive to the mechanistic assumptions in our forward model. For example, the simple functional forms adopted for many biogeochemical fluxes and the reduction of spatially heterogeneous processes to zeroth order, globally averaged equations could influence our results. However, wherever possible, we used parameterizations that have a fundamental physical basis, such as the logarithmic dependence of climate on pCO_2 and the Arrhenius-style temperature dependence of weathering. In instances where the physical basis is uncertain, we adopted generalized power laws with widely varying exponents to describe relationships between variables, and introduced free parameters to account for unknown processes. Column 2 of Fig. 6, and Supplementary Note 6 explore the sensitivity of our results to different continental weathering parameterizations. We find that none of the key conclusions are changed by using different functional forms. Nonetheless, our quantitative estimates of key variables could be refined by better mechanistic understanding carbon cycle relationships. Specifically, the magnitude of the weatherability increase since 100 Myr ago is moderately sensitive to the choice of continental weathering function (Fig. 6; Supplementary Note 6).

Another potential limitation is that we are imposing linear trends in some model parameters, thereby potentially underfitting the data and underestimating the uncertainties in retrieved parameters. In Supplementary Note 5, we repeat our analysis with a simplified data set to show that our conclusions are robust to these linearity assumptions. Supplementary Note 4 also shows that possible changes in K-feldspar uptake[16] in the seafloor do not change our qualitative conclusions.

In summary, we presented a new geological carbon cycle model, which includes ocean chemistry and the kinetics of seafloor weathering, and applied it to the last 100 Myr ago. Model outputs were compared to proxies for temperature, atmospheric CO_2, seafloor carbonate content, ocean pH and ocean saturation state. A MCMC inversion rigorously constrained carbon cycle parameters given these data. Assuming that proxies are accurate and that our forward model accurately parameterizes the carbon cycle, we report five key conclusions. First, the temperature dependence of continental silicate weathering is considerably weaker than commonly assumed. Most carbon cycle models use an effective activation energy to $\sim$50–100 kJ mol^{-1}, whereas our results imply $E_a = 20^{+10}_{-5}$ kJ mol^{-1}, which suggests that continental silicate weathering is less effective at buffering climate against changes in outgassing or insolation. Second, mid-Cretaceous continental weatherability was 30–58% of modern weatherability (1σ), although the precise magnitude of the change is sensitive to the functional form adopted for continental weathering. This increase in weatherability since 100 Myr ago is best explained by continental uplift and sea-level decline. Third, the average Earth system climate sensitivity is $\Delta T_{2x} = 5.6^{+1.3}_{-1.2}$ K for a CO_2 doubling (1σ). This is considerably higher than fast-feedback estimates for the modern climate, and could explain why extremely high pCO_2 levels are required to reproduce greenhouse climates in GCMs. This result is derived assuming methane variations are fully captured by temperature-dependent feedbacks, and it is sensitive to uncertain temperature proxies. Fourth, Cretaceous outgassing was unlikely ($\sim$9% probability) to be greater than double modern outgassing. Finally, continental weathering is probably the dominant carbon sink throughout the last 100 Myr ago, and introducing seafloor weathering into our model has a relatively small effect on the inverse modelling results. However, the strong temperature sensitivity and spreading rate dependence of seafloor weathering implies that it could have been a dominant carbon sink earlier in Earth history.

Methods

Model description. Python code for the model is available open source from the first author's website. The time evolution of the carbon cycle is described by the following set of equations:

$$\begin{aligned}
\frac{dC_O}{dt} &= \frac{-J(C_O - C_P)}{M_O} + \frac{F_{out}}{M_O} + \frac{F_{carb}}{M_O} - \frac{P_{ocean}}{M_O} \\
\frac{dA_O}{dt} &= \frac{-J(A_O - A_P)}{M_O} + 2\frac{F_{sil}}{M_O} + 2\frac{F_{carb}}{M_O} - 2\frac{P_{ocean}}{M_O} \\
\frac{dC_P}{dt} &= \frac{J(C_O - C_P)}{M_P} - \frac{P_{pore}}{M_P} \\
\frac{dA_P}{dt} &= \frac{J(A_O - A_P)}{M_P} + 2\frac{F_{diss}}{M_P} - 2\frac{P_{pore}}{M_P}
\end{aligned} \quad (6)$$

Here C_O and C_P are the concentrations of carbon (Tmol C kg^{-1}) in the atmosphere–ocean and pore-space, respectively. The carbon concentration in the pore-space is equivalent to the dissolved inorganic carbon (DIC) abundance, $C_P = DIC_P$, whereas carbon in the atmosphere–ocean reservoir is equal to marine DIC plus atmospheric carbon, $C_O = DIC_O + pCO_2 \times s$, where s is a scaling factor equal to the ratio of total number of moles in the atmosphere divided by the mass of the ocean, $s = (1.8\times10^{20})/M_O$. Similarly, $A_O = ALK_O$ and $A_P = ALK_P$ are the carbonate alkalinities in the atmosphere–ocean and pore-space, respectively (Tmol eq kg^{-1}). The global outgassing flux (Tmol C per year) is specified by F_{out}, whereas the rates of continental silicate weathering and carbonate weathering are F_{sil} and F_{carb}, respectively (Tmol C per year). Seafloor weathering from basalt dissolution (Tmol eq per year) is F_{diss}, and the precipitation flux of carbonates (Tmol C per year) in the ocean and pore-space are given by P_{ocean} and P_{pore}, respectively. The mass of the ocean and the pore space is given by $M_O = 1.35\times10^{21}$ kg and $M_P = 1.35\times10^{19}$ kg, respectively[20]. We assume a range for J of $1.4\times10^{15} - 6.8\times10^{16}$ kg per year, which implies the time to circulate one ocean volume through the pore-space is between $\tau = 20$ and $\tau = 1{,}000$ kyr, consistent with estimates from Johnson and Pruis[56] and Caldeira[20].

A common simplification in carbon cycle modelling is to neglect carbonate weathering[15,22,24]. This is justified on the grounds that carbonate weathering does not constitute a net carbon source. On long timescales, the carbon consumption from silicate and seafloor weathering must balance carbon outgassing (plus any imbalance in organic weathering and burial), and this balance determines atmospheric CO_2 and climate. However, the saturation state of the ocean is affected by carbonate weathering, and so we include carbonate weathering to model ocean chemistry. We do not track crustal or mantle reservoirs, and the atmospheric reservoir of CO_2 is set by equilibrium partitioning with the ocean (see below). Because we are not tracking fluxes between the atmosphere and ocean, continental silicate weathering is not a carbon source or sink; the release of cations (alkalinity) from silicate dissolution does not directly add carbon to the combined atmosphere–ocean system. Instead, the cations consume carbon indirectly when they later precipitate as marine carbonates.

There is no surface ocean box in our model. This is because we are only interested in the changes in properties of the bulk ocean, which are determined by varying boundary conditions not by the deep-surface partitioning. In addition, we are focused on timescales $>10^6$ years, and so the dynamics of deep-surface ocean mixing are unimportant. If we were to partition the ocean into surface and deep, the main difference would be differential temperature dependence of carbon speciation. We also do not include organic carbon weathering and burial. This is justifiable because the negative feedback from oxidative weathering ensures they are approximately balanced[57]. Empirically, the carbon isotope record reveals that the organic burial fraction has changed by only $\sim$10% over the last 100 Myr ago[58]. Consequently, the change in the organic burial flux is likely modest and so the omission of organic carbon will not affect our conclusions.

The functional forms for the flux terms not already described in the main text are presented below.

Continental silicate weathering. The continental weathering parameterization was described in the main text except for the coefficient α in equation (2). This coefficient is assumed to be 0.2–0.5 (ref. 59). Strictly speaking, soil pCO_2 should replace atmospheric pCO_2 in equation (2) because soil pCO_2 determines soil pH, and therefore silicate dissolution rates. However, if modest changes in maximum biological productivity are allowed, then the range of CO_2 dependencies from the term $\left(pCO_2/pCO_2^{mod}\right)^{\alpha}$, with α varying from 0.2 to 0.5, is broadly equivalent to replacing atmospheric pCO_2 with soil pCO_2 (ref. 60; see Supplementary Fig. 6). Consequently, we retain atmospheric pCO_2 and pCO_2^{mod} in equation (2). To test the sensitivity of our results to weathering parameterizations, in addition to the pCO_2 power-law dependence in equation (2), we also consider a Michaelis–Menten law in the main text (see results).

The range adopted for relative Cretaceous weatherability, $1 + W$, is based on literature estimates[10,23,43,47,49] of how external factors may have affected weatherability, and extending the range in either direction does not markedly change our results. The weatherability factor, ω, can also be interpreted as the sensitivity of the weathering response to changes in pCO_2 and temperature. For example, an increase in ω implies that an increase in surface temperature will result in a larger change in the continental weathering flux, F_{sil}.

Continental carbonate weathering. We assume that carbonate weathering has the same functional form as silicate weathering, except for an additional dimensionless multiplicative factor, ω_{carb}, to allow for the possibility that carbonate weathering is subject to different temperature dependence, CO_2 dependence and weatherability factors:

$$F_{carb} = \omega_{carb}\ \omega F_{carb}^{mod}\left(\frac{pCO_2}{pCO_2^{mod}}\right)^{\alpha} \exp(\Delta T_S/T_e) \quad (7)$$

The carbonate weatherability factor is defined as follows:

$$\omega_{carb} = (1 + C_{WF}t/100\ \text{Myr}) \quad (8)$$

We assume a range of values for C_{WF} from -0.9 to 1.5 to allow for large differences between carbonate weathering and silicate weathering. For example, carbonates may have a lower effective activation energy compared to silicates because carbonate weathering is sensitive to runoff, whereas silicate weathering is sensitive to both runoff and a kinetic temperature effect[7,25]. Carbonate weathering may also have a different response to changes in uplift[23], or varying fluxes due to changes in the crustal reservoir of carbonates. It should be noted that changes in carbonate weathering only affect saturation state; the changes in CO_2, temperature and ocean pH due to carbonate weathering changes are negligible. This is because—as explained above—temperature and CO_2 are set by the balance between outgassing and silicate weathering plus seafloor weathering. Consequently, any conclusions drawn about those variables are unaffected by our formulation for carbonate weathering.

Climate model. To relate ΔT_S to pCO_2, we adopt the following climate model:

$$\Delta T_S = \Delta T_{2x}\left(\frac{ln\left(pCO_2/pCO_2^{mod}\right)}{\ln(2)} - \frac{t}{228\ \text{Myr}}\right) + \Delta P\left(\frac{t}{100\ \text{Myr}}\right) \quad (9)$$

Here ΔT_{2x} is the climate sensitivity parameter, ΔP is a palaeogeography parameter and the second term accounts for solar luminosity changes (Supplementary Note 2). We divide by ln(2) so that ΔT_{2x} has conventional units of Kelvin warming per CO_2

doubling. Supplementary Fig. 9 compares different climate parameterizations and GCM results from the literature and illustrates why equation (9) is suitable. The parameter ΔP is the secular cooling (in K) since the mid-Cretaceous due to palaeogeography changes. A review of GCM studies concluded that $\Delta P = 0$–3.0 K (ref. 52). We assume $\Delta P = 0$–5.0 K to be conservative, noting that some models suggest 5 K of warming from an Eocene continental configuration[61].

Outgassing. Estimates of Cenozoic and Mesozoic outgassing histories vary substantially. Figure 7 shows a variety of outgassing reconstructions from the literature expressed as crustal production or spreading rates, which are assumed to covary with global outgassing. Generally, these reconstructions suggest that global outgassing at 100 Ma was between 1.5x and 2.5x modern outgassing. This conclusion is based on several independent lines of evidence including reconstructions of plate extent and plate motion, seismic imaging of subducted plates, and reconstructions of seafloor age and depth (see Supplementary Note 7 for a summary of outgassing estimates with references). The outlying reconstruction in Figure 7 (aqua curve) is disputed because it uses a contentious crustal age distribution[42].

For simplicity, we assume a linear global outgassing history:

$$F_{\mathrm{out}} = F_{\mathrm{out}}^{\mathrm{mod}}(1 + Vt/100\ \mathrm{Myr}) \tag{10}$$

Here $F_{\mathrm{out}}^{\mathrm{mod}}$ is modern outgassing (Tmol C per year), t is time (in Myr ago) and V is a dimensionless scaling factor. Using crustal production or spreading rate as a proxy for global outgassing is a simplification because it ignores subaerial metamorphism and hot spot volcanism (for example, ref. 62). Given the uncertainty in these other contributions, we adopt a very broad range of outgassing histories since 100 Myr ago by assuming $V = 0.2$–1.5. Thus, we allow mid-Cretaceous outgassing to range from 20 to 150% greater than modern.

Basalt dissolution and seafloor weathering. The temperature dependence of seafloor weathering uses the following Arrhenius-style expression[17]:

$$F_{\mathrm{diss}} \propto \exp\left(-E_{\mathrm{bas}}/RT_{\mathrm{pore}}\right) \tag{11}$$

Here E_{bas} (kJ mol^{-1}) is the effective activation energy of basalt dissolution, R is the universal gas constant and T_{pore} is the pore-space temperature. Coogan and Dosso[17] reported an empirically derived activation energy of $E_{\mathrm{bas}} = 92 \pm 7$ kJ mol^{-1}, whereas experimental studies[14,31] of basalt dissolution suggest activation energies between 42 and 109 kJ mol^{-1}. We adopt a range of activation energies from $E_{\mathrm{bas}} = 40$ to110 kJ mol^{-1}.

Because Cenozoic and Mesozoic pore-space temperatures are controlled by deep-ocean temperature[17], we must determine the link between global mean surface temperatures and deep-ocean temperatures. Figure 8 shows mean global surface temperatures plotted against deep-ocean temperatures using output from fully coupled atmosphere–ocean GCMs and palaeoclimate proxy data (see Supplementary Note 1 for details). The relationship is described by an empirical linear fit:

$$T_{\mathrm{D}} = a_{\mathrm{grad}} T_{\mathrm{S}} + b_{\mathrm{int}} \tag{12}$$

Here T_{D} (K) is the mean deep-ocean temperature and T_{S} (K) is the mean surface temperature. The best-fit gradient and intercept are $a_{\mathrm{grad}} = 1.02$ and $b_{\mathrm{int}} = -16.7$, respectively. However, we assume a broad gradient range $a_{\mathrm{grad}} = 0.8$–1.4, whereas the intercept, $b_{\mathrm{int}} = 274.037 - a_{\mathrm{grad}} \times 285$ is chosen to ensure consistency with modern conditions. Figure 8 shows the range of possible $T_{\mathrm{D}} \propto T_{\mathrm{S}}$ relationships used in this study.

Our parameterization of deep-ocean temperature improves upon Brady and Gíslason[14] because ours is based on an ensemble of GCM results and globally averaged palaeoclimate proxies rather than a single climate model. In addition, Brady and Gíslason[14] overestimated the dependence of deep-ocean temperature on surface climate because their parameterization is based on a single near-equatorial latitude of 6.7°. The relationship between globally averaged abyssal temperatures and surface climate is more muted than the relationship with equatorial abyssal temperatures. This can be seen in our Fig. 8 and in Fig. 12 of Manabe and Bryan[63], despite the model of the latter being the basis for the Brady and Gíslason[14] parameterization.

To relate the pore-space temperature to the deep-ocean temperature, we adopt empirical results[17]. Oxygen isotopes indicate that for both the Cenozoic and Mesozoic, the mean pore-space temperature of seafloor carbonate precipitation is consistently $\sim$9 K warmer than the minimum temperature of seafloor carbonate precipitation (deep-ocean temperatures). Consequently, we assume $T_{\mathrm{pore}} = T_{\mathrm{D}} + 9$. This modification has a very minor effect on the model output because it is largely the change in temperature, and not its absolute value, that controls variations in the seafloor weathering flux.

Quantifying the pH dependence of seafloor weathering is more challenging because most experiments either fail to separate the pH and direct CO_2 effect[14], focus on individual minerals rather than whole-rock dissolution rates[64,65], or do not explore the full pH range relevant to seafloor weathering[66].

Gudbrandsson *et al.*[67] measure whole-rock crystalline basalt dissolution rates for $2 < \mathrm{pH} < 11$. They find that Ca release is a U-shape function of pH (their Fig. 8), where the minimum of the 'U' at 25 °C is somewhere between pH = 7 and pH = 9, depending on the assumptions made about the reactive surface area (experimental results are sparse and so are fitted with an analytic model of dissolution). Given the uncertainty in this dissolution curve, it is difficult to predict the sign of the dissolution change for a modest change in ocean pH. For example, a decline in pH from 8.2 to 7.4—which is approximately the change from the modern ocean to mid-Cretaceous—predicts a 20% decrease in Ca release according to one Gudbrandsson *et al.*[67], their Fig. 8f fit, and a 7% increase in Ca release according to the alternative Gudbrandsson *et al.*[67], their Fig. 8e fit. Either way, the change in dissolution is minor, and so a possible first order approximation is to assume basalt dissolution on the seafloor is independent of pH for the Mesozoic and Cenozoic.

However, the Gudbrandsson *et al.*[67] experiments may not accurately capture the pH dependence of seafloor weathering because they were not done in seawater and did not include carbon chemistry. Some experimental studies[65,68] show that olivine dissolution is CO_2-dependent at high pH values, ostensibly because abundant carbonate ions protect Si–O bonds, thereby decreasing dissolution with increasing DIC. In contrast, Golubev *et al.*[64] studied the effect of CO_2 on dissolution rates for a range of pH values and found that forsterite, diopside and hornblende do not have CO_2-dependent dissolution rates at any pH. Unfortunately, however, Golubev *et al.*[64] did not consider plagioclase, so their results cannot easily be extrapolated to the basaltic seafloor. Wolff-Boenisch *et al.*[66] showed that the CO_2 dependence of crystalline basalt is independent of CO_2 at low pH levels, but did not repeat the experiment at high pH values.

We allow for the possibility of pH dependence by setting the rate of dissolution proportional to $[\mathrm{H}^+]_{\mathrm{P}}^{\gamma}$, where γ varies from 0 (no pH dependence) to 0.5 (strong pH dependence dominated by basaltic glass dissolution):

$$F_{\mathrm{diss}} = k_{\mathrm{diss}} \left(\frac{F_{\mathrm{out}}}{F_{\mathrm{out}}^{\mathrm{mod}}}\right)^{\beta} \exp\left(-E_{\mathrm{bas}}/RT_{\mathrm{pore}}\right) \left(\frac{[\mathrm{H}^+]_{\mathrm{P}}}{[\mathrm{H}^+]_{\mathrm{P}}^{\mathrm{mod}}}\right)^{\gamma} \tag{13}$$

Here k_{diss} is a proportionality constant chosen to match the modern flux, $[\mathrm{H}^+]_{\mathrm{P}}$ is the hydrogen ion molality in the pore-space and $[\mathrm{H}^+]_{\mathrm{P}}^{\mathrm{mod}}$ is the modern molality. Because dissolution is dependent on crustal production and crustal production is proportional to global outgassing, we assume dissolution is dependent on outgassing with some unknown power–law relationship, defined by $\beta = 0$–1.

Better knowledge of the pH dependence, temperature dependence and CO_2 dependence of basalt dissolution would improve our constraints on the carbon cycle. Specifically, whole-rock dissolution experiments performed at high pH that separate the effects of pH and DIC would allow for more precise parameterizations of seafloor weathering.

Precipitation fluxes. The precipitation flux of marine carbonates, P_{ocean}, is the sum of the fluxes of shelf carbonates, P_{shelf}, and pelagic carbonates, P_{pelagic}:

$$P_{\mathrm{ocean}} = P_{\mathrm{shelf}} + P_{\mathrm{pelagic}} \tag{14}$$

Following Ridgwell[69], the shelf precipitation flux is given by:

$$P_{\mathrm{shelf}} = k_{\mathrm{shelf}} \frac{A_{\mathrm{shelf}}}{A_{\mathrm{shelf}}^{\mathrm{mod}}} (\Omega_{\mathrm{O}} - 1)^{n} \tag{15}$$

Here Ω_{O} is the saturation state of the ocean (defined below by equation (20)), A_{shelf} is the area of continental shelf available for carbonate precipitation, with $A_{\mathrm{shelf}}^{\mathrm{mod}}$ denoting the modern shelf area, and k_{shelf} is a proportionality constant. Shelf area is approximated by a polynomial fit (Supplementary Fig. 7) to reconstructed tropical shelf area from Walker *et al.*[70]. The exponent n defines the proportionality between the saturation state of the ocean and the precipitation flux. This is typically taken to be 1.7 based on the latitudinal dependence of carbonate accumulation and saturation state[71]. Rather than consider calcite and aragonite precipitation separately, we instead allow n to vary widely from 1.0 to 2.5.

The pelagic carbonate flux depends on the calcite compensation depth (CCD), Z_{CCD} (km), which can be calculated using the following equation[72]:

$$Z_{\mathrm{CCD}} = 4 + 6.25 \ln(\Omega_{\mathrm{O}}) \tag{16}$$

Pelagic carbonate deposition is proportional to the fractional area above the CCD, $f(Z_{\mathrm{CCD}})$, which can be approximated by an exponential fit to hypsometric data[73]:

$$P_{\mathrm{pelagic}} \propto f(Z_{\mathrm{CCD}}) = 0.07 \exp(Z_{\mathrm{CCD}}/2.2) \tag{17}$$

Equations (14–17) can then be combined to give the total ocean precipitation flux:

$$P_{\mathrm{ocean}} = k_{\mathrm{shelf}} \frac{A_{\mathrm{shelf}}}{A_{\mathrm{shelf}}^{\mathrm{mod}}} (\Omega_{\mathrm{O}} - 1)^{n} + k_{\mathrm{pelagic}} \Omega_{\mathrm{O}}^{2.84} \tag{18}$$

The proportionality constants k_{shelf} and k_{pelagic} are chosen to reproduce the modern partitioning between shelf and pelagic carbonates (see below). Here the precise functional form of equation (18) only matters for determining ocean saturation state; carbon fluxes, pCO_2 and temperatures are unaffected.

The pore-space carbonate precipitation flux is analogous to shelf precipitation except that there is no area dependence:

$$P_{\mathrm{pore}} = k_{\mathrm{pore}} (\Omega_{\mathrm{P}} - 1)^{n} \tag{19}$$

Here Ω_{P} is the saturation state of the pore-space and k_{pore} is a proportionality constant chosen to reproduce the modern flux. The exponent n is the same as for shelf precipitation. Repeating the inverse analysis allowing different exponents for

shelf and seafloor carbonate precipitation does not change results substantially (not shown).

Finally, the saturation state of the ocean and the pore-space are defined as follows:

$$\Omega_O = \frac{[Ca^{2+}][CO_3^{2-}]_O}{K_{sp}} \text{ and } \Omega_P = \frac{[Ca^{2+}][CO_3^{2-}]_P}{K_{sp}} \quad (20)$$

Here $K_{sp} = K_{sp}(T)$ is the temperature-dependent solubility product from Pilson[74]. Supplementary Methods explain how the solubility product is calculated.

Ocean chemistry. Alkalinity and DIC have the following standard definitions in our model, where ALK is often referred to as 'carbonate alkalinity' in the literature:

$$\begin{aligned} DIC &= [CO_3^{2-}] + [HCO_3^-] + [CO_2aq] \\ ALK &= 2[CO_3^{2-}] + [HCO_3^-] \end{aligned} \quad (21)$$

Given carbon and alkalinity in the atmosphere–ocean (C_O, ALK_O) or the pore-space (C_P, ALK_P), we can calculate ocean chemistry using the following set of equations[74]:

$$[CO_2aq] = pCO_2 \times H_{CO_2} \quad (22)$$

$$[HCO_3^-] = \frac{[CO_2aq] \times K_1^*}{[H^+]} \quad (23)$$

$$[CO_3^{2-}] = \frac{[HCO_3^-] \times K_2^*}{[H^+]} \quad (24)$$

$$\frac{ALK}{K_1^* K_2^*}\left(1 + \frac{s}{H_{CO_2}}\right)[H^+]^2 + \frac{(ALK - C)}{K_2^*}[H^+] + (ALK - 2C) = 0 \quad (25)$$

$$pH = -\log_{10}([H^+]) \quad (26)$$

Here H_{CO2} is the Henry's law constant for CO_2, $[CO_2aq]$ is the sum of the concentrations of free CO_2 and H_2CO_3, and K_1^* and K_2^* are the first and second apparent dissociation constants of carbonic acid, respectively. Temperature-dependent expressions for these constants can be found in Supplementary Methods. The set of equations described above must be solved separately for the ocean and the pore-space by substituting the generic carbon concentration and alkalinity (C, ALK) for (C_O, ALK_O) and (C_P, ALK_P), respectively. The scaling factor, s, is defined above with respect to equation (6). Equation (25) is derived by combining equations (21), (23) and (24) (Supplementary Methods). This quadratic can be solved to find $[H^+]$. Once this is known, then equations (22), (23) and (24) define the remaining carbon chemistry variables.

Rather than attempt to model the complexities of calcium and magnesium cycling in our model, we impose observed changes in $[Ca^{2+}]$ abundances from seawater inclusions[75]. In our model, changes in alkalinity are driven purely by weathering and carbonate precipitation. Thus, by imposing $[Ca^{2+}]$ variations, we are effectively assuming that observed $[Ca^{2+}]$ changes are offset by changes in other cations and anions, such that they have no direct effect on alkalinity, for example, magnesium exchange with the seafloor. We fit a third-order polynomial to the $[Ca^{2+}]$ reconstruction in Tyrrell and Zeebe[75] to achieve the fast computation times necessary for Bayesian inversion (Supplementary Fig. 8).

Initial conditions and numerical solution. Table 2 shows all the initial values assumed in our model or ranges for variables that are uncertain. All other initial values are fully determined by the variables in this table.

The system of differential equations describing the carbon cycle (equation (6)) was solved in Python using the ordinary differential equation integrator in the *SciPy* module. Model outputs were compared with equivalent steady-state calculations and were always in agreement to within a few per cent or better (Supplementary Note 3). This validates the numerical integration and implies that the time-dependent model is always in quasi steady state. In addition, the integrated flux imbalance over 100 Myr ago equals the change in the carbon reservoirs to within ~2% or better in every case, confirming that mass is being conserved in our model.

Proxies. The geochemical proxies plotted in Figs 2–5, and Supplementary Figs 2, 15 and 16 are described in Supplementary Methods. For each variable, we searched the literature for the broadest possible range of proxy estimates. Proxies were typically binned into 10 Myr ago intervals, and for each interval the best estimate was taken to be the midpoint of the full range of proxy estimates, while the 1σ uncertainty in the best estimate spanned the full range (Supplementary Figs 10–13). This conservative approach helps ensure that our conclusions are robust to uncertainties in different proxy methods.

Data availability. The binned proxy data used as inputs for this analysis along with the carbon cycle model code are available on the website of the first author. www.krisstott.com

References

1. Berner, R. A. & Caldeira, K. The need for mass balance and feedback in the geochemical carbon cycle. *Geology* **25,** 955–956 (1997).
2. Walker, J. C., Hays, P. & Kasting, J. F. A negative feedback mechanism for the long-term stabilization of Earth's surface temperature. *J. Geophys. Res. Oceans* **86,** 9776–9782 (1981).
3. Berner, R. A. & Kothavala, Z. GEOCARB III: a revised model of atmospheric CO_2 over Phanerozoic time. *Am. J. Sci.* **301,** 182–204 (2001).
4. Kump, L. R., Kasting, J. F. & Crane, R. G. *The Earth System* 3rd edn (Prentice Hall PTR, 2010).
5. Gaillardet, J., Dupré, B., Louvat, P. & Allegre, C. Global silicate weathering and CO_2 consumption rates deduced from the chemistry of large rivers. *Chem. Geol.* **159,** 3–30 (1999).
6. Huh, Y. & Edmond, J. M. The fluvial geochemistry of the rivers of Eastern Siberia: III. Tributaries of the Lena and Anabar draining the basement terrain of the Siberian Craton and the Trans-Baikal Highlands. *Geochim. Cosmochim. Acta* **63,** 967–987 (1999).
7. Francois, L. M. & Walker, J. Modelling the Phanerozoic carbon cycle and climate: constraints from the '7Sr/' rSr isotopic ratio of seawater. *Am. J. Sci.* **292,** 135 (1992).
8. Maher, K. & Chamberlain, C. Hydrologic regulation of chemical weathering and the geologic carbon cycle. *Science* **343,** 1502–1504 (2014).
9. Raymo, M. & Ruddiman, W. F. Tectonic forcing of late Cenozoic climate. *Nature* **359,** 117–122 (1992).
10. Mills, B., Daines, S. J. & Lenton, T. M. Changing tectonic controls on the long-term carbon cycle from Mesozoic to present. *Geochem. Geophys. Geosyst.* **15,** 4866–4884 (2014).
11. Taylor, L., Banwart, S., Leake, J. & Beerling, D. J. Modeling the evolutionary rise of ectomycorrhiza on sub-surface weathering environments and the geochemical carbon cycle. *Am. J. Sci.* **311,** 369–403 (2011).
12. Walker, J. C. *Biogeochemistry of Global Change* 3–28 (Springer, 1993).
13. Kump, L. R. & Arthur, M. A. *Tectonic Uplift and Climate Change.* (ed. Ruddiman, W.) 399–426 (Plenum Publishing, 1997).
14. Brady, P. V. & Gíslason, S. R. Seafloor weathering controls on atmospheric CO_2 and global climate. *Geochim. Cosmochim. Acta* **61,** 965–973 (1997).
15. Sleep, N. H. & Zahnle, K. Carbon dioxide cycling and implications for climate on ancient Earth. *J. Geophys. Res. Planets* **106,** 1373–1399 (2001).
16. Coogan, L. A. & Gillis, K. M. Evidence that low-temperature oceanic hydrothermal systems play an important role in the silicate-carbonate weathering cycle and long-term climate regulation. *Geochem. Geophys. Geosys.* **14,** 1771–1786 (2013).
17. Coogan, L. A. & Dosso, S. E. Alteration of ocean crust provides a strong temperature dependent feedback on the geological carbon cycle and is a primary driver of the Sr-isotopic composition of seawater. *Earth Planet. Sci. Lett.* **415,** 38–46 (2015).
18. Gillis, K. & Coogan, L. Secular variation in carbon uptake into the ocean crust. *Earth. Planet. Sci. Lett.* **302,** 385–392 (2011).
19. Alt, J. C. & Teagle, D. A. The uptake of carbon during alteration of ocean crust. *Geochim. Cosmochim. Acta* **63,** 1527–1535 (1999).
20. Caldeira, K. Long-term control of atmospheric carbon dioxide; low-temperature seafloor alteration or terrestrial silicate-rock weathering? *Am. J. Sci.* **295,** 1077–1114 (1995).
21. Coogan, L. A., Parrish, R. R. & Roberts, N. M. Early hydrothermal carbon uptake by the upper oceanic crust: insight from *in situ* U-Pb dating. *Geology* **44,** 147–150 (2016).
22. Foley, B. J. The role of plate tectonic-climate coupling and exposed land area in the development of habitable climates on rocky planets. *Astrophys. J.* **812,** 36 (2015).
23. Berner, R. A. *The Phanerozoic Carbon Cycle: CO_2 and O_2* (Oxford Univ. Press, 2004).
24. Abbot, D. S., Cowan, N. B. & Ciesla, F. J. Indication of insensitivity of planetary weathering behavior and habitable zone to surface land fraction. *Astrophys. J.* **756,** 178 (2012).
25. Le Hir, G., Ramstein, G., Donnadieu, Y. & Goddéris, Y. Scenario for the evolution of atmospheric pCO_2 during a snowball Earth. *Geology* **36,** 47–50 (2008).
26. Arvidson, R. S., Mackenzie, F. T. & Guidry, M. W. Geologic history of seawater: A MAGic approach to carbon chemistry and ocean ventilation. *Chem. Geol.* **362,** 287–304 (2013).
27. West, A. J., Galy, A. & Bickle, M. Tectonic and climatic controls on silicate weathering. *Earth Planet. Sci. Lett.* **235,** 211–228 (2005).
28. IPCC. *Climate Change 2013: the Physical Science Basis: Working Group I Contribution to the Fifth Assessment Report of the Intergovernmental Panel on Climate Change* (Cambridge Univ. Press (2014).
29. Foreman-Mackey, D., Hogg, D. W., Lang, D. & Goodman, J. emcee: the MCMC hammer. *Publ. Astron. Soc. Pac.* **125,** 306 (2013).

30. Nielsen, S. G. *et al.* Hydrothermal fluid fluxes calculated from the isotopic mass balance of thallium in the ocean crust. *Earth Planet. Sci. Lett.* **251,** 120–133 (2006).
31. White, A. F. & Buss, H. L. in *Surface and Ground Water, Weathering and Soils, Treatise on Geochemistry* 2nd edn (ed. Drever, J. I.) 115–155 (Elsevier, 2014).
32. Tajika, E. Carbon cycle and climate change during the Cretaceous inferred from a biogeochemical carbon cycle model. *Island Arc* **8,** 293–303 (1999).
33. Kump, L. R., Brantley, S. L. & Arthur, M. A. Chemical weathering, atmospheric CO_2, and climate. *Annu. Rev. Earth. Planet. Sci.* **28,** 611–667 (2000).
34. Hren, M. T., Hilley, G. E. & Chamberlain, C. P. The relationship between tectonic uplift and chemical weathering rates in the Washington Cascades: field measurements and model predictions. *Am. J. Sci.* **307,** 1041–1063 (2007).
35. Eiriksdottir, E. S., Gislason, S. R. & Oelkers, E. H. Does temperature or runoff control the feedback between chemical denudation and climate? Insights from NE Iceland. *Geochim. Cosmochim. Acta* **107,** 65–81 (2013).
36. Riebe, C. S., Kirchner, J. W., Granger, D. E. & Finkel, R. C. Strong tectonic and weak climatic control of long-term chemical weathering rates. *Geology* **29,** 511–514 (2001).
37. Von Blanckenburg, F. The control mechanisms of erosion and weathering at basin scale from cosmogenic nuclides in river sediment. *Earth Planet. Sci. Lett.* **237,** 462–479 (2005).
38. Maher, K. The dependence of chemical weathering rates on fluid residence time. *Earth Planet. Sci. Lett.* **294,** 101–110 (2010).
39. Riebe, C. S., Kirchner, J. W. & Finkel, R. C. Erosional and climatic effects on long-term chemical weathering rates in granitic landscapes spanning diverse climate regimes. *Earth Planet. Sci. Lett.* **224,** 547–562 (2004).
40. West, A. J. Thickness of the chemical weathering zone and implications for erosional and climatic drivers of weathering and for carbon-cycle feedbacks. *Geology* **40,** 811–814 (2012).
41. Caves, J. K., Jost, A. B., Lau, K. V. & Maher, K. Cenozoic carbon cycle imbalances and a variable weathering feedback. *Earth Planet. Sci. Lett.* **450,** 152–163 (2016).
42. Müller, R. D., Sdrolias, M., Gaina, C., Steinberger, B. & Heine, C. Long-term sea-level fluctuations driven by ocean basin dynamics. *Science* **319,** 1357–1362 (2008).
43. Skelton, P. W. *The Cretaceous World* (Cambridge Univ. Press, 2003).
44. Kashiwagi, H., Ogawa, Y. & Shikazono, N. Relationship between weathering, mountain uplift, and climate during the Cenozoic as deduced from the global carbon–strontium cycle model. *Palaeogeogr. Palaeoclimatol. Palaeoecol.* **270,** 139–149 (2008).
45. Dessert, C., Dupré, B., Gaillardet, J., François, L. M. & Allegre, C. J. Basalt weathering laws and the impact of basalt weathering on the global carbon cycle. *Chem. Geol.* **202,** 257–273 (2003).
46. Li, G. & Elderfield, H. Evolution of carbon cycle over the past 100 million years. *Geochim. Cosmochim. Acta* **103,** 11–25 (2013).
47. Bluth, G. J. & Kump, L. R. Phanerozoic paleogeology. *Am. J. Sci.* **291,** 284–308 (1991).
48. Jacobson, A. D., Andrews, M. G., Lehn, G. O. & Holmden, C. Silicate versus carbonate weathering in Iceland: new insights from Ca isotopes. *Earth Planet. Sci. Lett.* **416,** 132–142 (2015).
49. Goddéris, Y., Donnadieu, Y., Le Hir, G., Lefebvre, V. & Nardin, E. The role of palaeogeography in the Phanerozoic history of atmospheric CO_2 and climate. *Earth Sci. Rev.* **128,** 122–138 (2014).
50. Gibbs, M. T., Bluth, G. J., Fawcett, P. J. & Kump, L. R. Global chemical erosion over the last 250My: Variations due to changes in paleogeography, paleoclimate, and paleogeology. *Am. J. Sci.* **299,** 611–651 (1999).
51. Volk, T. Rise of angiosperms as a factor in long-term climatic cooling. *Geology* **17,** 107–110 (1989).
52. Royer, D., Pagani, M. & Beerling, D. Geobiological constraints on Earth system sensitivity to CO_2 during the Cretaceous and Cenozoic. *Geobiology* **10,** 298–310 (2012).
53. Park, J. & Royer, D. L. Geologic constraints on the glacial amplification of Phanerozoic climate sensitivity. *Am. J. Sci.* **311,** 1–26 (2011).
54. Pagani, M., Huber, M. & Sageman, B. in *Treatise on Geochemistry* 2nd edn (eds Holland, H. D. & Turekian, K. K.) 281–304 (Elsevier, 2014).
55. Beerling, D. J., Fox, A., Stevenson, D. S. & Valdes, P. J. Enhanced chemistry-climate feedbacks in past greenhouse worlds. *Proc. Natl Acad. Sci. USA* **108,** 9770–9775 (2011).
56. Johnson, H. P. & Pruis, M. J. Fluxes of fluid and heat from the oceanic crustal reservoir. *Earth Planet. Sci. Lett.* **216,** 565–574 (2003).
57. François, L. M., Walker, J. C. & Opdyke, B. N. The history of global weathering and the chemical evolution of the ocean-atmosphere system. *Evol. Earth Planets*. (eds Takahashi, E., Jeanloz, R. & Rubie, D.) 143–159 (American Geophysical Union, Washington DC, USA, 1993).
58. Katz, M. E. *et al.* Biological overprint of the geological carbon cycle. *Mar. Geol.* **217,** 323–338 (2005).
59. Schwartzman, D. *Life, Temperature, and the Earth: the Self-Organizing Biosphere* (Columbia Univ. Press, 2002).
60. Volk, T. Feedbacks between weathering and atmospheric CO2 over the last 100 million years. *Am. J. Sci.* **287,** 763–779 (1987).
61. Caballero, R. & Huber, M. State-dependent climate sensitivity in past warm climates and its implications for future climate projections. *Proc. Natl Acad. Sci. USA* **110,** 14162–14167 (2013).
62. Kashiwagi, H. Atmospheric carbon dioxide and climate change since the Late Jurassic (150Ma) derived from a global carbon cycle model. *Palaeogeogr. Palaeoclimatol. Palaeoecol.* **454,** 82–90 (2016).
63. Manabe, S. & Bryan, K. CO_2-induced change in a coupled ocean-atmosphere model and its paleoclimatic implications. *J. Geophys. Res. Oceans* **90,** 11689–11707 (1985).
64. Golubev, S. V., Pokrovsky, O. S. & Schott, J. Experimental determination of the effect of dissolved CO_2 on the dissolution kinetics of Mg and Ca silicates at 25 C. *Chem. Geol.* **217,** 227–238 (2005).
65. Pokrovsky, O. S. & Schott, J. Kinetics and mechanism of forsterite dissolution at 25 C and pH from 1 to 12. *Geochim. Cosmochim. Acta* **64,** 3313–3325 (2000).
66. Wolff-Boenisch, D., Wenau, S., Gislason, S. R. & Oelkers, E. H. Dissolution of basalts and peridotite in seawater, in the presence of ligands, and CO_2: implications for mineral sequestration of carbon dioxide. *Geochim. Cosmochim. Acta* **75,** 5510–5525 (2011).
67. Gudbrandsson, S., Wolff-Boenisch, D., Gislason, S. R. & Oelkers, E. H. An experimental study of crystalline basalt dissolution from 2 pH 11 and temperatures from 5 to 75° C. *Geochim. Cosmochim. Acta* **75,** 5496–5509 (2011).
68. Wogelius, R. A. & Walther, J. V. Olivine dissolution at 25 C: effects of pH, CO_2, and organic acids. *Geochim. Cosmochim. Acta* **55,** 943–954 (1991).
69. Ridgwell, A. A mid Mesozoic revolution in the regulation of ocean chemistry. *Mar. Geol.* **217,** 339–357 (2005).
70. Walker, L. J., Wilkinson, B. H. & Ivany, L. C. Continental drift and Phanerozoic carbonate accumulation in shallow-shelf and deep-marine settings. *J. Geol.* **110,** 75–87 (2002).
71. Opdyke, B. N. & Wilkinson, B. H. Carbonate mineral saturation state and cratonic limestone accumulation. *Am. J. Sci.* **293,** 217–217 (1993).
72. Broecker, W. S. & Takahashi, T. The relationship between lysocline depth and in situ carbonate ion concentration. *Deep Sea Res.* **25,** 65–95 (1978).
73. Sclater, J. G., Boyle, E. & Edmond, J. M. *Deep Drilling Results in the Atlantic Ocean: Continental Margins and Paleoenvironment*. (eds Talwani, M., Hay, W. & Ryan, W. B. F.) 235–248 (American Geophysical Union, Washington DC, USA, 1979).
74. Pilson, M. E. *An Introduction to the Chemistry of the Sea* (Prentice-Hall, Inc., 1998).
75. Tyrrell, T. & Zeebe, R. E. History of carbonate ion concentration over the last 100 million years. *Geochim. Cosmochim. Acta* **68,** 3521–3530 (2004).
76. Lee, C.-T. A. & Lackey, J. S. Global continental arc flare-ups and their relation to long-term greenhouse conditions. *Elements* **11,** 125–130 (2015).
77. Hartmann, J., Jansen, N., Dürr, H. H., Kempe, S. & Köhler, P. Global CO_2-consumption by chemical weathering: what is the contribution of highly active weathering regions? *Glob. Planet. Change* **69,** 185–194 (2009).
78. Iglesias-Rodriguez, M. D. *et al.* Progress made in study of ocean's calcium carbonate budget. *EOS* **83,** 365–375 (2002).

Acknowledgements

We thank Dorian Abbott, Lee Kump and the two anonymous reviewers whose comments greatly improved the manuscript. We also thank Giada Arney, Laurence Coogan, James Kasting, Rodrigo Luger and Chris Reinhard for helpful discussions. This work was supported by NASA Exobiology Program grant NNX15AL23G awarded to D.C.C. and by the NASA Astrobiology Institute's Virtual Planetary Laboratory, grant NNA13AA93A. J.K.-T. is supported by NASA Headquarters under the NASA Earth and Space Science Fellowship program, grant NNX15AR63H.

Author contributions

Both authors contributed to the conception of this project and the drafting of the manuscript. J.K.-T. created the model and performed the analysis.

Additional information

Supplementary Information accompanies this paper at http://www.nature.com/naturecommunications

Competing interests: The authors declare no competing financial interests.

How to cite this article: Krissansen-Totton, J. *et al.* Constraining climate sensitivity and continental versus seafloor weathering using an inverse geological carbon cycle model. *Nat. Commun.* **8,** 15423 doi: 10.1038/ncomms15423 (2017).

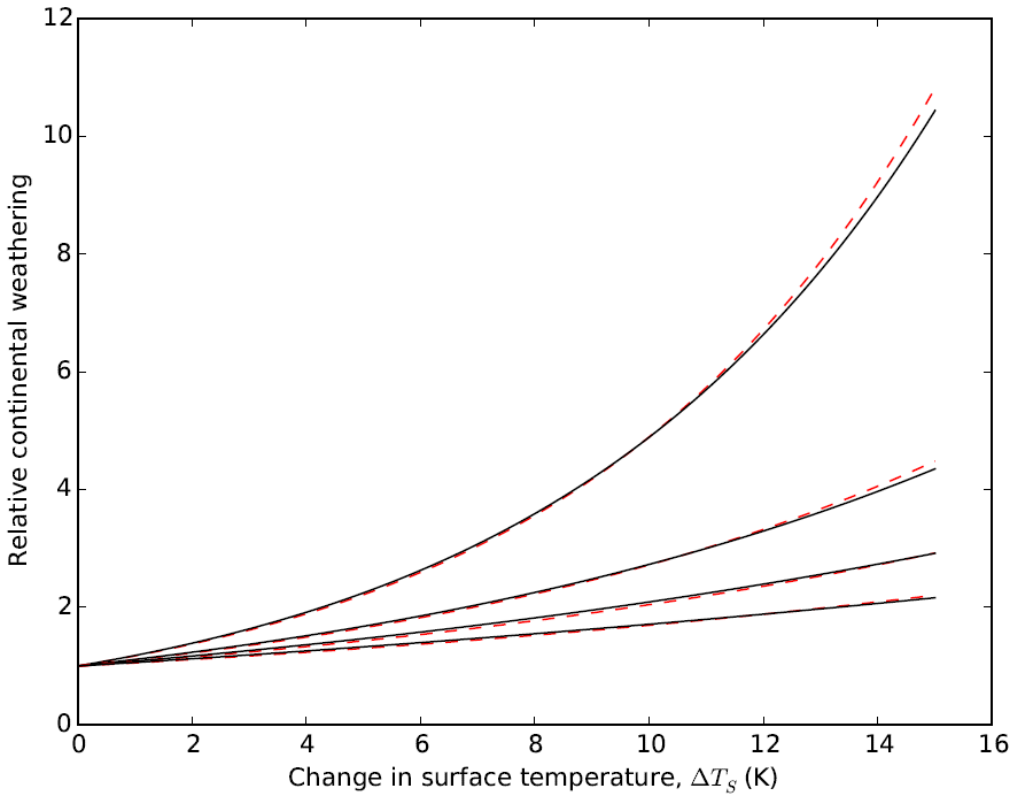

Supplementary Figure 1: This figure justifies the omission of a linear runoff dependence in our continental weathering function. The four black lines are defined by the function relative weathering = $\exp(\Delta T_S/T_e)(1+0.04\times\Delta T_S)$, where the lines have effective temperatures of T_e = 8, 15, 25, and 50 K. The four red dashed lines are exponentials, relative weathering = $\exp(\Delta T_S/T_e)$, with effective temperatures chosen to fit the black lines (T_e = 6.3, 10, 14, 19 K). We see that for the range of temperature variations we are considering, any weathering function with a runoff term can be fitted with a single exponential, and hence it is appropriate to model the overall temperature dependence of continental weathering using an exponential.

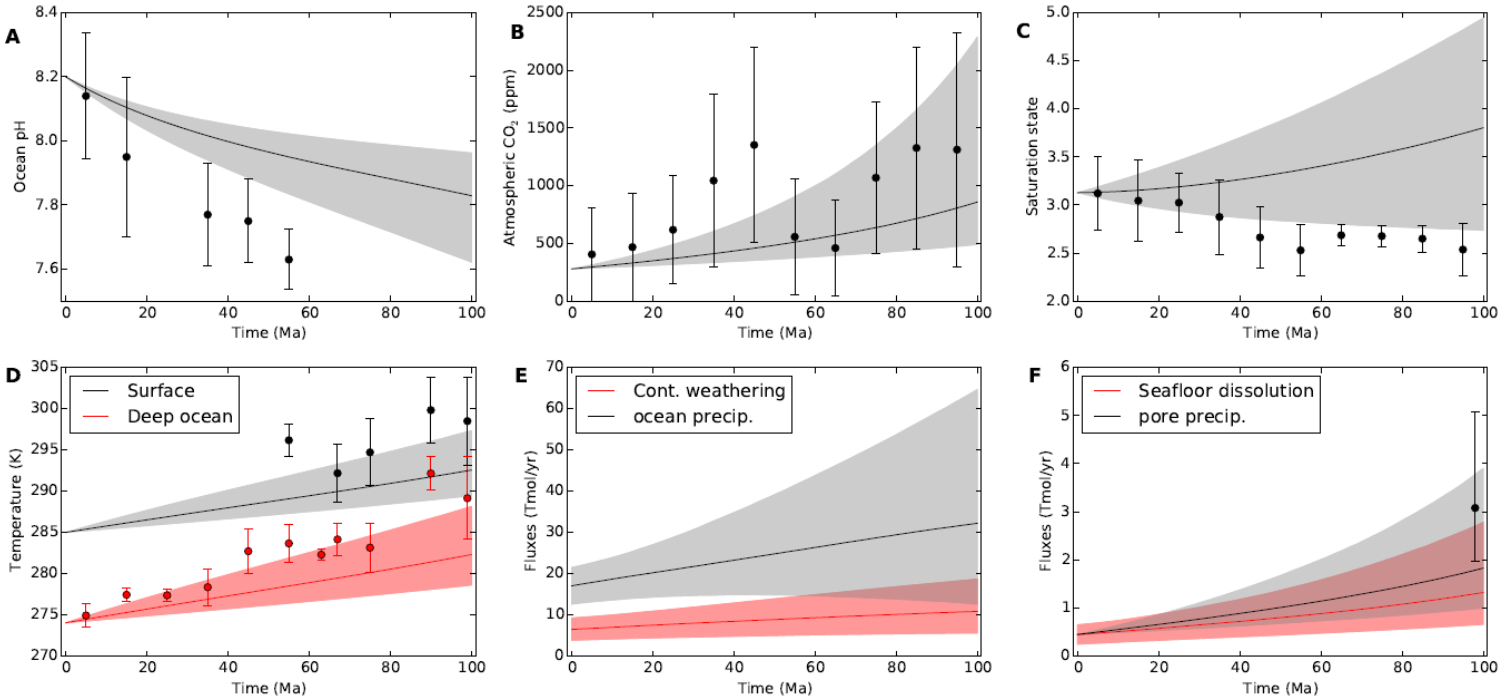

Supplementary Figure 2: Selected model outputs and geochemical proxy data for a conventional temperature sensitivity range for continental weathering ($T_e = 5$ to 15 K) and a 40-60% change in continental weatherability over the last 100 Ma (W=-0.6 to -0.4). Grey and red shaded regions represent the model output 90% confidence obtained from 10,000 forward model runs using the parameter ranges described in Table 1. The grey and red solid lines are the median model outputs. Black and red dots represent binned geochemical proxy data, and error bars denote the range of binned proxy estimates (see main text for references and explanation). Here, the model envelopes marginally encompass the proxy data. The upper end of the temperature and seafloor envelopes fit proxies, pCO_2 is an excellent fit, and the saturation state and pH proxies are slightly outside the envelope.

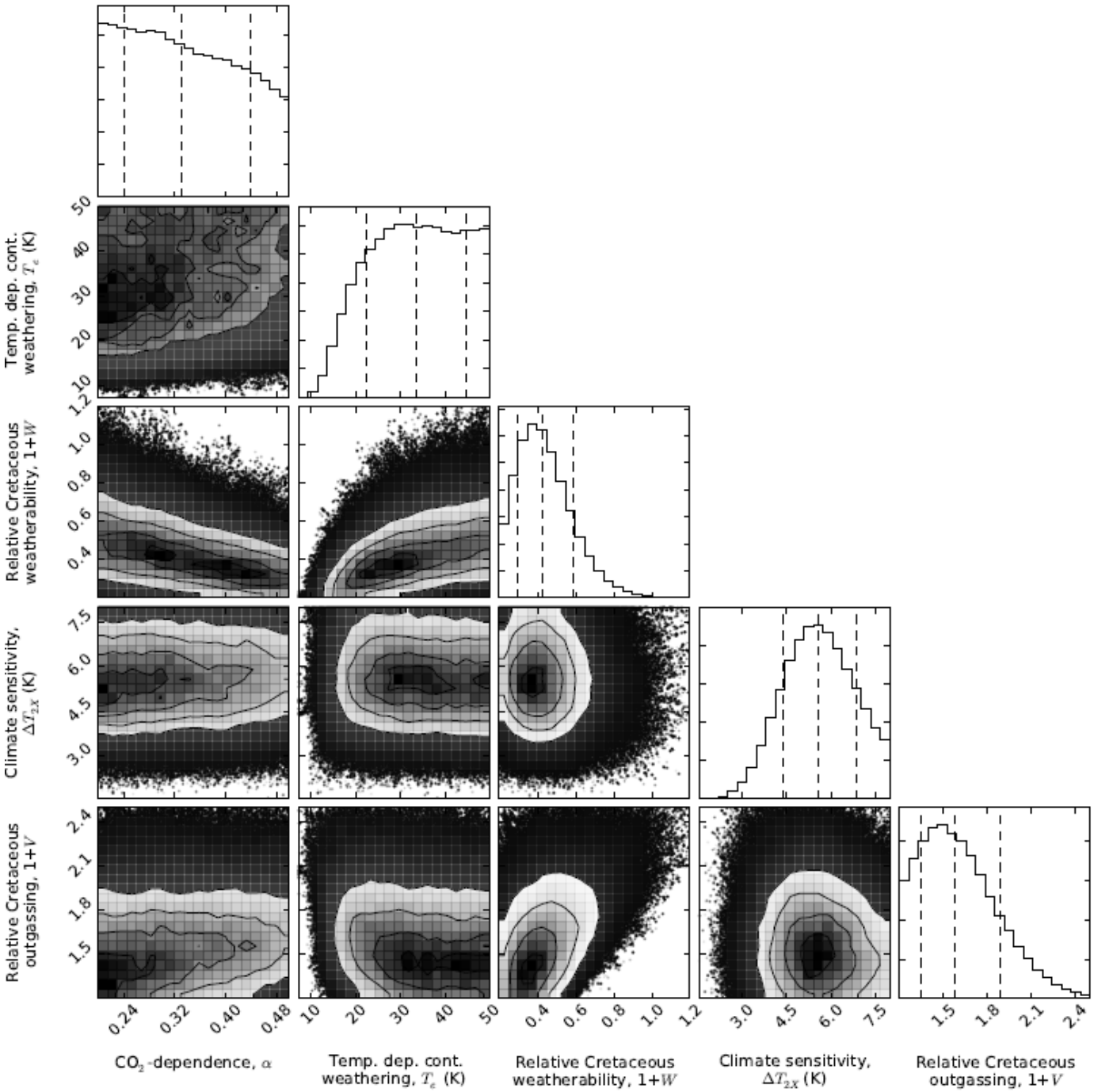

Supplementary Figure 3: Posterior probability distributions for selected carbon cycle variables from Bayesian MCMC analysis. The outer diagonal elements are the marginal distributions, identical to Fig. 6 in the main text (Column 1, nominal model), where dotted lines denote median values and 1σ error bars. The off-diagonal elements are joint probability distributions, which show how each pair of variables co-varies. The joint distributions show degeneracies that could be resolved with better data. For example, there is a positive correlation between Cretaceous weatherability and Cretaceous outgassing; if outgassing at 100 Ma was high, then the weatherability change was necessarily modest, and vice versa. This degeneracy highlights uncertainty surrounding Cretaceous climate: whether high pCO_2 levels were caused by enhanced outgassing or reduced CO_2 sinks. If either variable could be constrained by data, then the retrieval would be more informative.

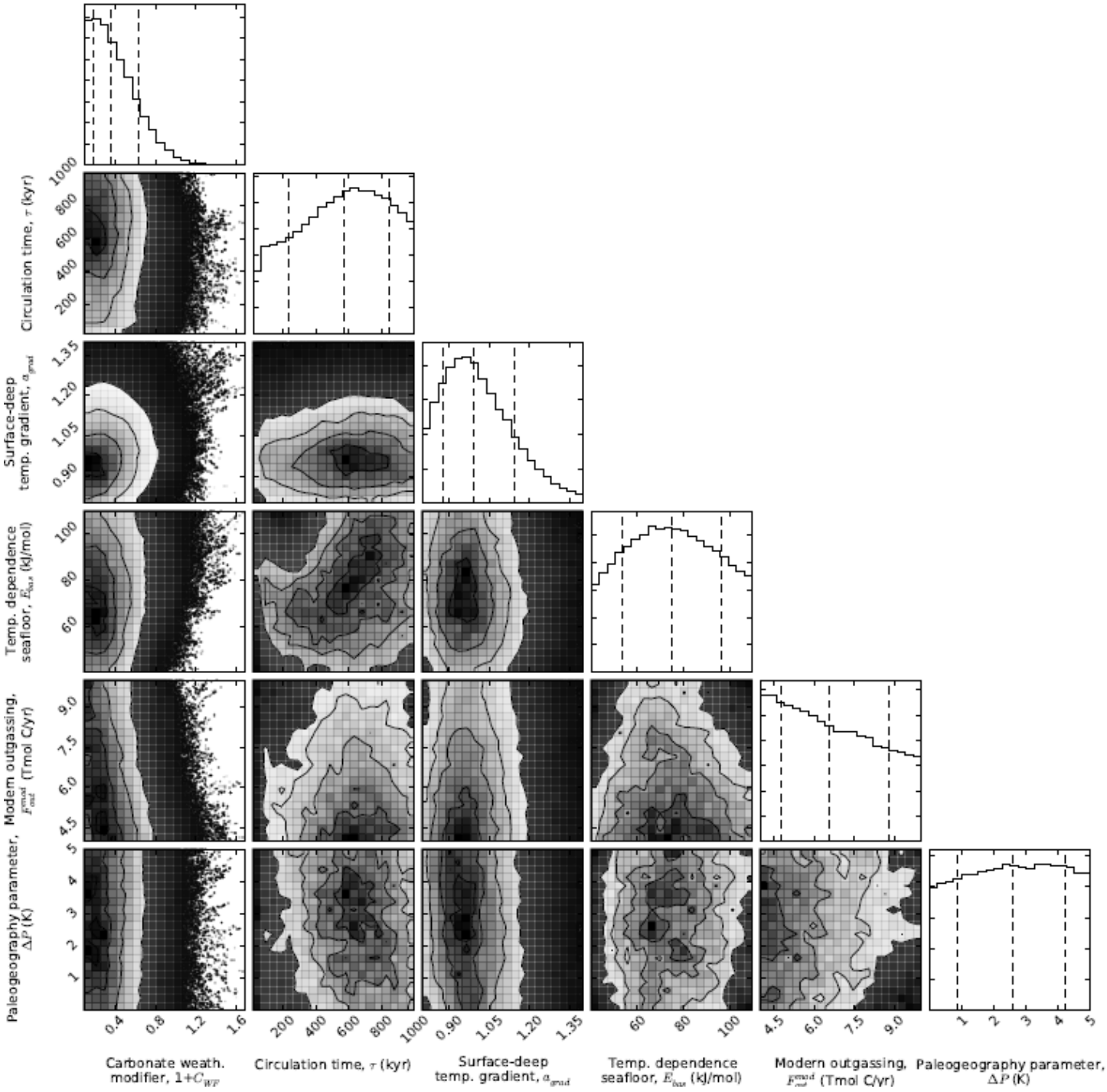

Supplementary Figure 4: Posterior distributions for variables that were omitted from Fig. 6. The outer diagonal elements are the marginal distributions, and the off-diagonal elements are joint probability distributions, which show how each pair of variables co-varies. Dotted lines represent the median value with 1σ error bars. Marginal distributions place tentative constraints on pore-space circulation time, the relationship between deep ocean and surface temperatures, and the effective activation energy for seafloor dissolution.

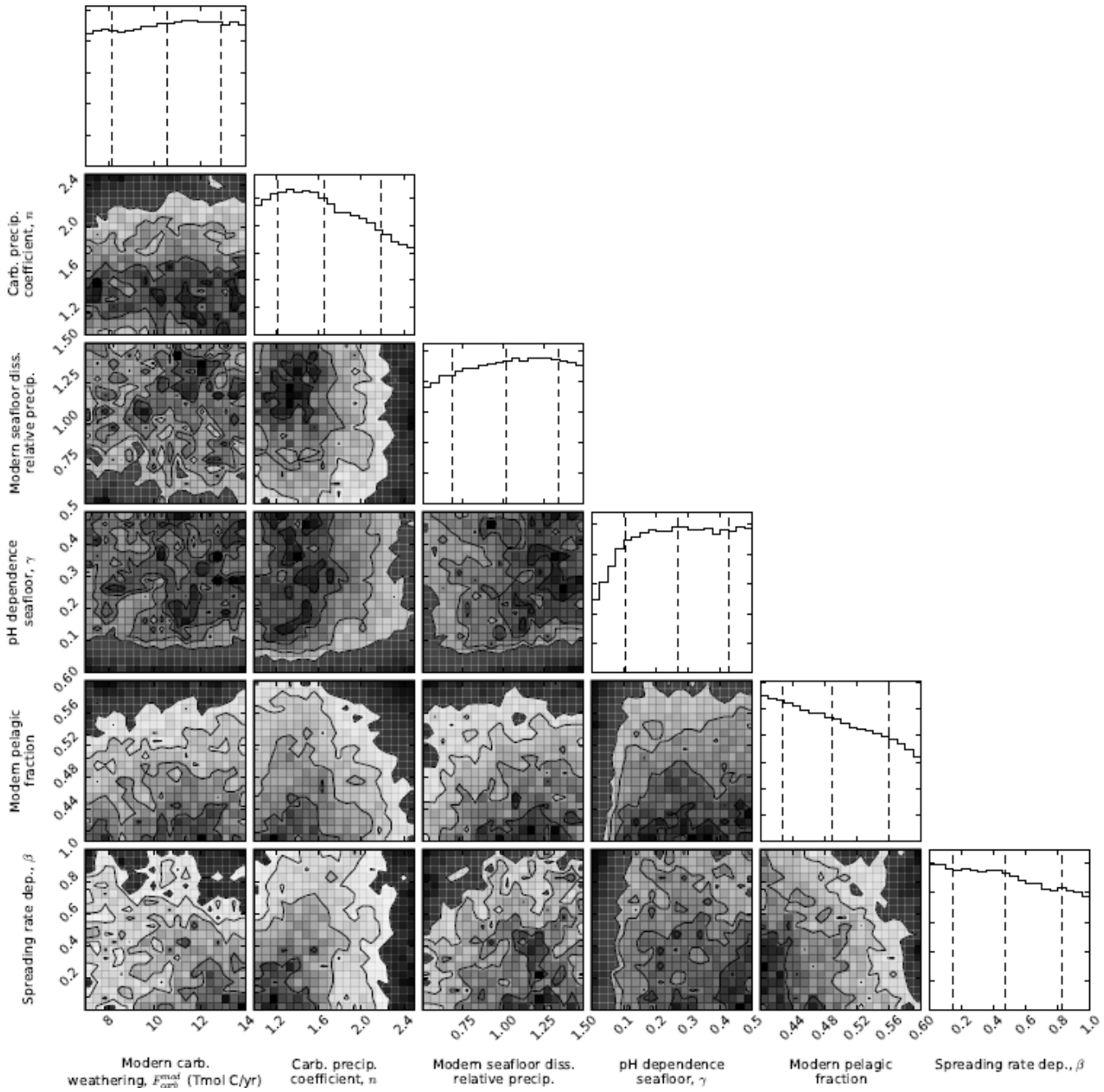

Supplementary Figure 5: Posterior distributions for variables that were omitted from Fig. 6, and supplementary figures 3 and 4. The outer diagonal elements are the marginal distributions, and the off-diagonal elements are joint probability distributions, which show how each pair of variables co-varies. Dotted lines represent the median value with 1σ error bars. Here the marginal distributions are relatively flat, indicating that these variables are not constrained by the data.

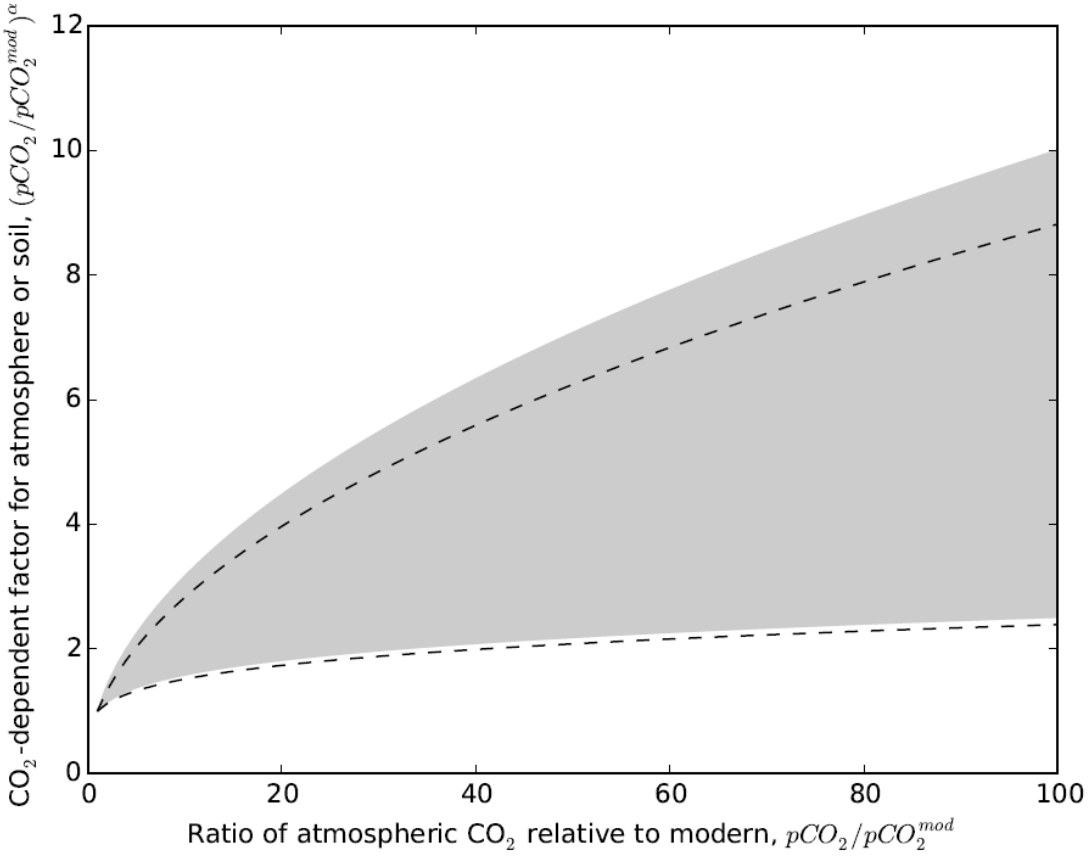

Supplementary Figure 6: Comparison of $\left(\mathrm{pCO_2}/\mathrm{pCO_2^{mod}}\right)^{\alpha}$ factor in equation (2) using pCO_2 values for the atmosphere or soil. The grey shaded region is the range of $\left(\mathrm{pCO_2}/\mathrm{pCO_2^{mod}}\right)^{\alpha}$ assumed in our model, where α =0.2-0.5. The black dotted lines bound the range of curves if soil pCO_2 is used instead, adopting the model of Volk[1] to link soil and atmospheric pCO_2, and assuming a maximum biosphere productivity of 4 times the modern productivity. We see that for our purposes it is valid to use atmospheric CO_2 in equation (2) rather than soil pCO_2.

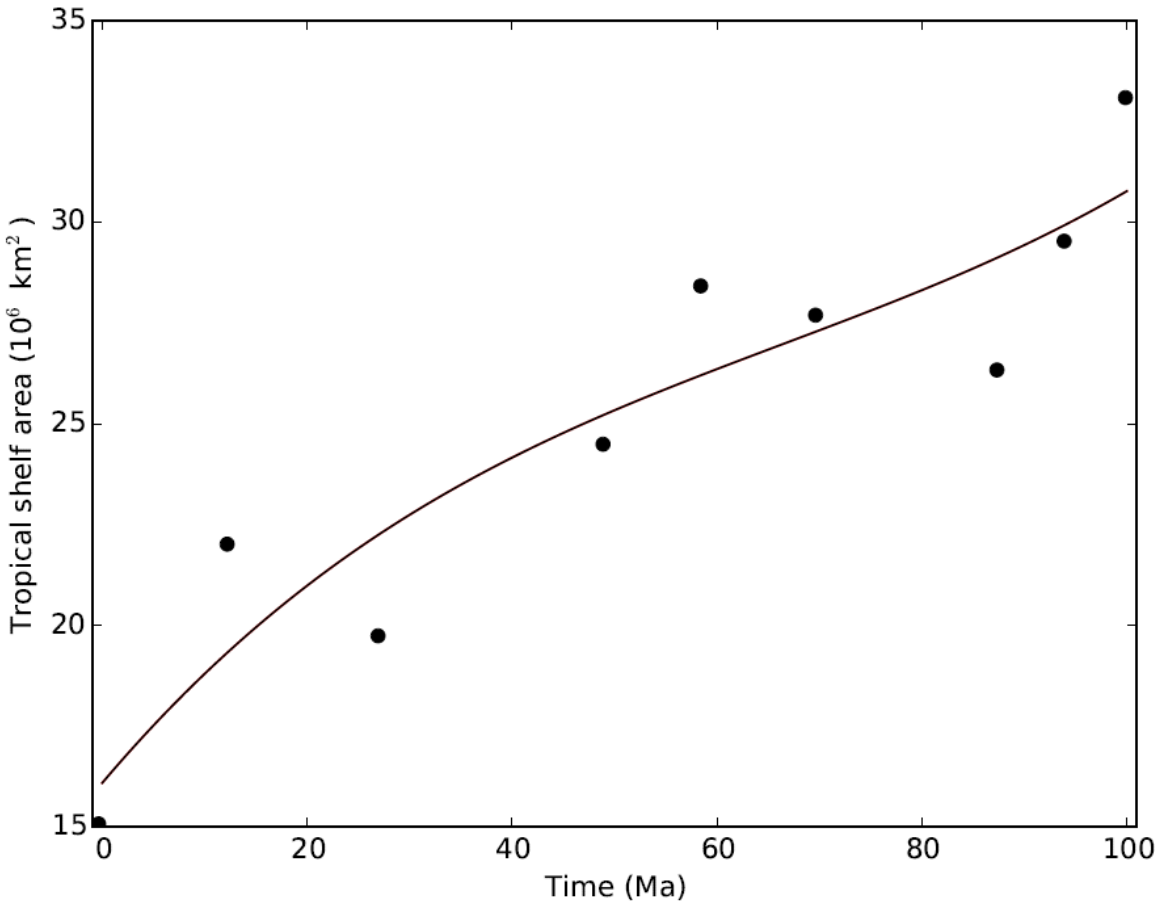

Supplementary Figure 7: Tropical shelf area estimates from Walker *et al.*[2] (circles) with the polynomial fit used in this study (solid line). The vast majority of shelf carbonates precipitate in tropical latitudes (0-30 degrees), and so we use reconstructed tropical shelf area to represent A_{shelf}. The fit is given by $A_{\text{shelf}} = 1.54\times10^{-23}t^3 - 3.072\times10^{-15}t^2 + 2.9997\times10^{-7}t + 16.089$

Here, t is in years since the present, and A_{shelf} is in 10^6 km^2.

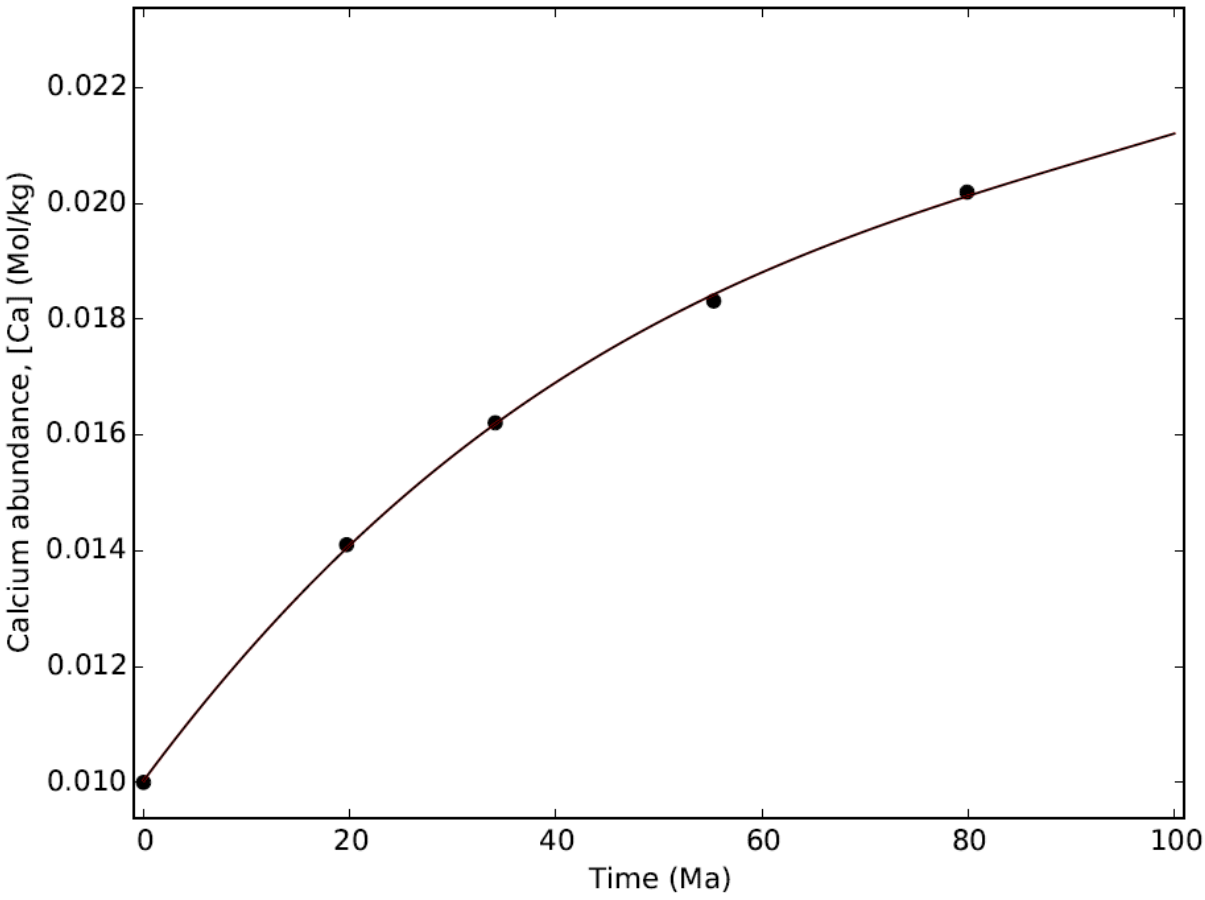

Supplementary Figure 8: Dissolved calcium ion abundance estimates from Tyrrell and Zeebe[3] for the last 100 Ma (circles) with the polynomial fit used in this study (solid line):

$$\left[\mathrm{Ca}^{2+}\right] = 7.00658\times10^{-27}t^3 - 1.9847\times10^{-18}t^2 + 2.4016\times10^{-10}t + 0.0100278$$

Here, t is in years since the present, and [Ca^{2+}] is in mol kg^{-1}. This expression was used for the calcium abundance in both the ocean and the pore-space.

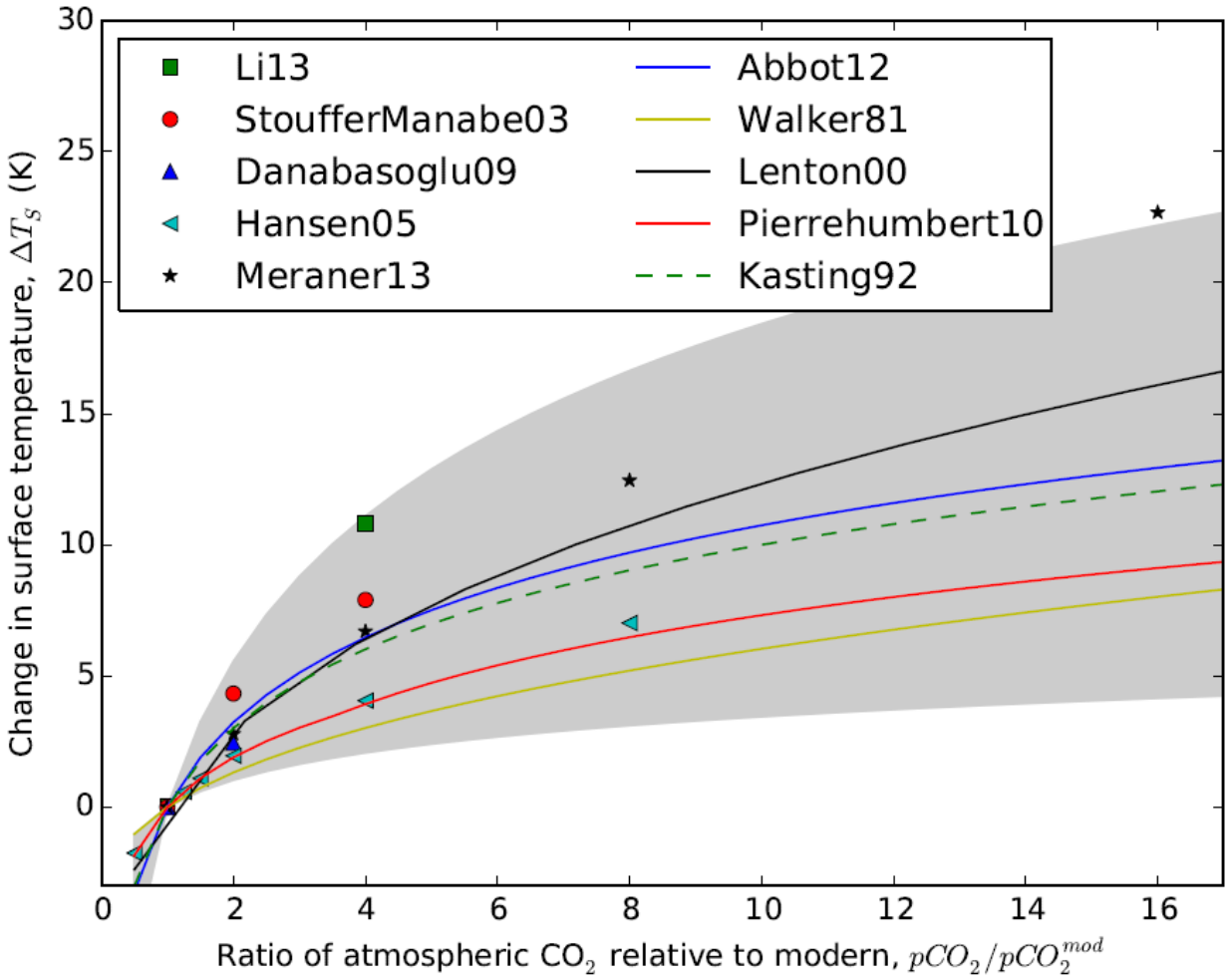

Supplementary Figure 9: A selection of GCM outputs (colored symbols) and simple climate models (lines) from the literature. The grey shaded region is the range of climate parameterizations considered in our model, equation (9), where the climate sensitivity, ΔT_{2x} =1.5 to 8.0 K. We see our range of climate parameterizations broadly encompasses the range of climate models. See Supplementary Note 1 for full references and further explanation.

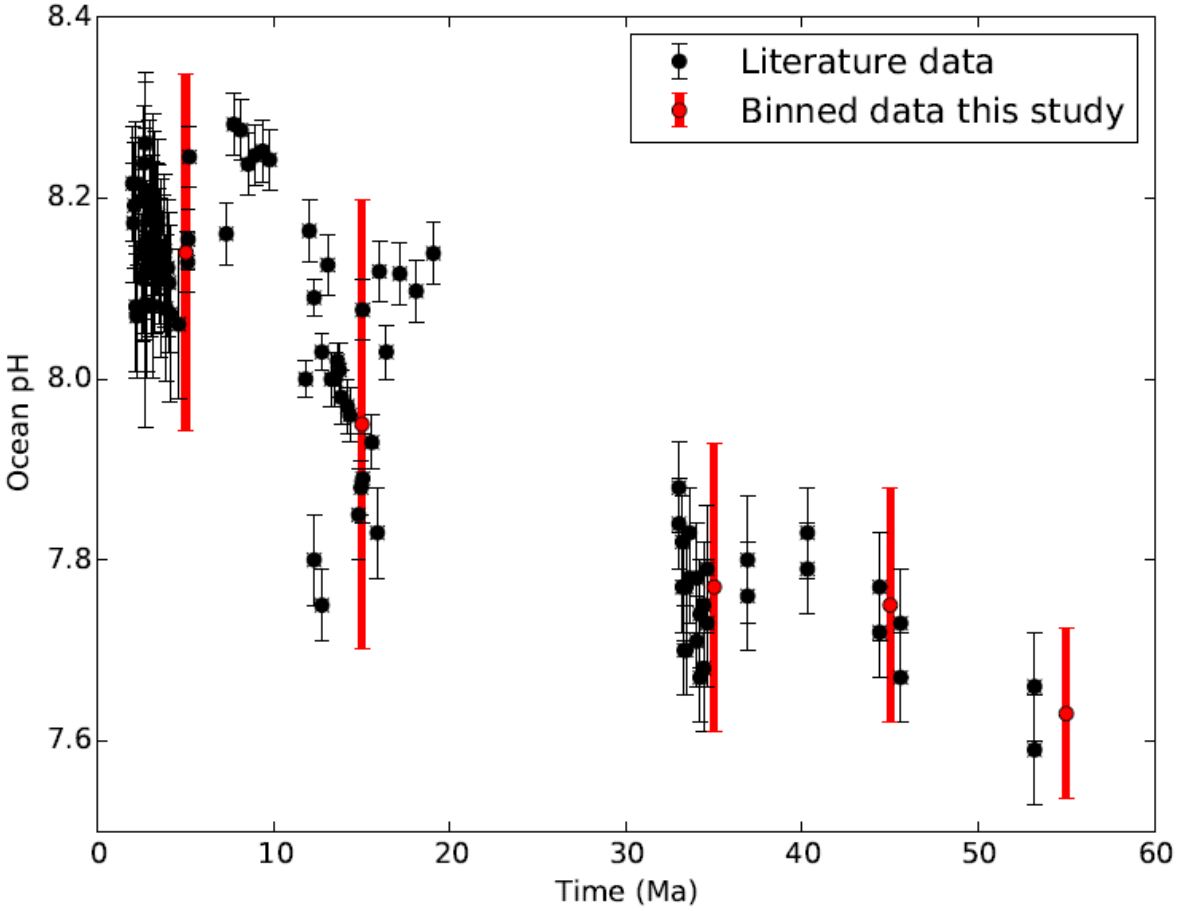

Supplementary Figure 10: Black squares show proxy estimates of ocean pH from the literature[4-9]. The red circles are the 10 Ma binned data used in this study. The uncertainty envelope for each binned data point is taken to be the range of proxy values within each 10 Ma bin.

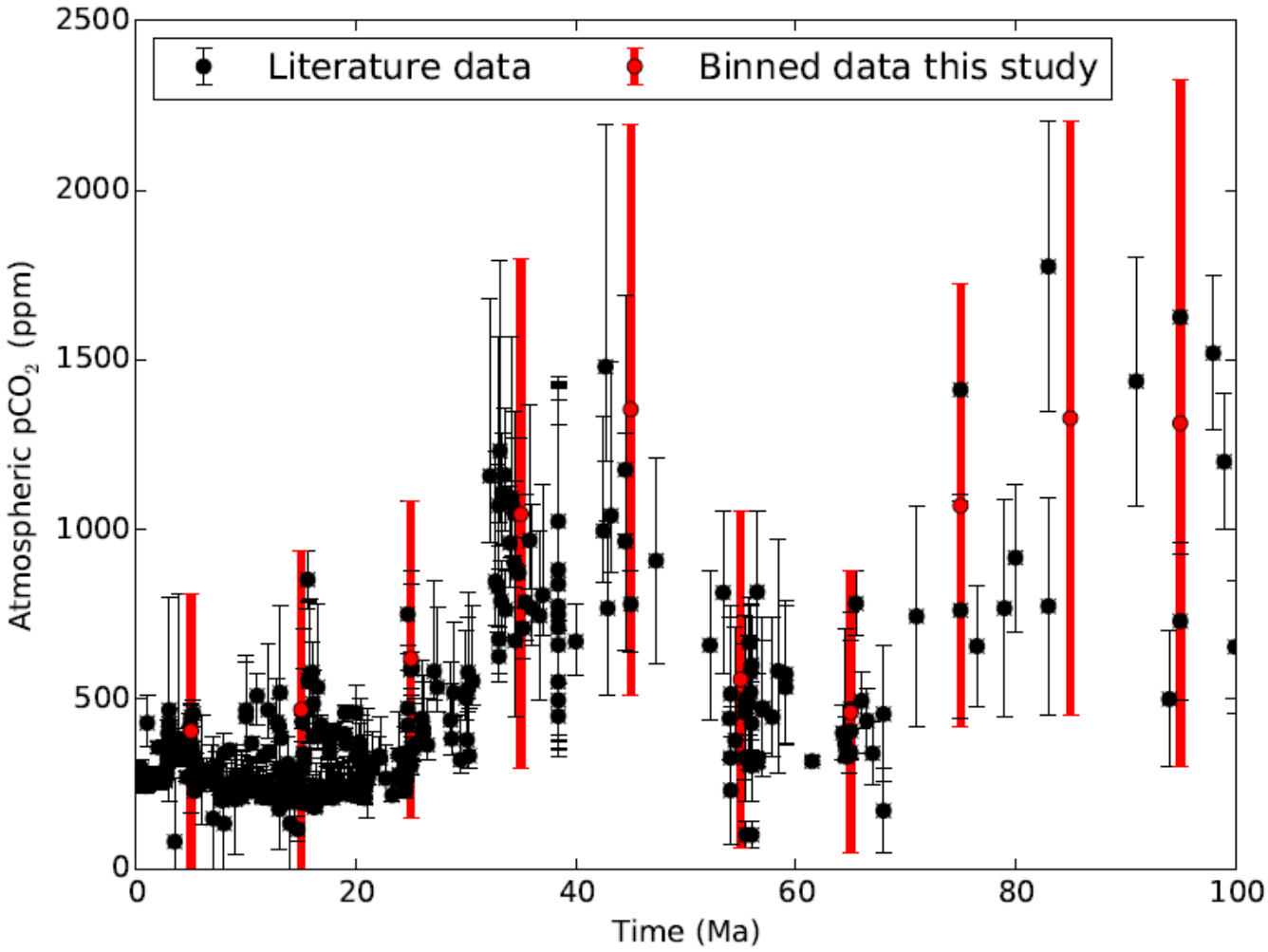

Supplementary Figure 11: Black squares show proxy estimates of atmospheric pCO_2 from the literature[10-16]. The red circles are the 10 Ma binned data used in this study. The uncertainty envelope for each binned data point is taken to be the range of proxy values within each 10 Ma bin.

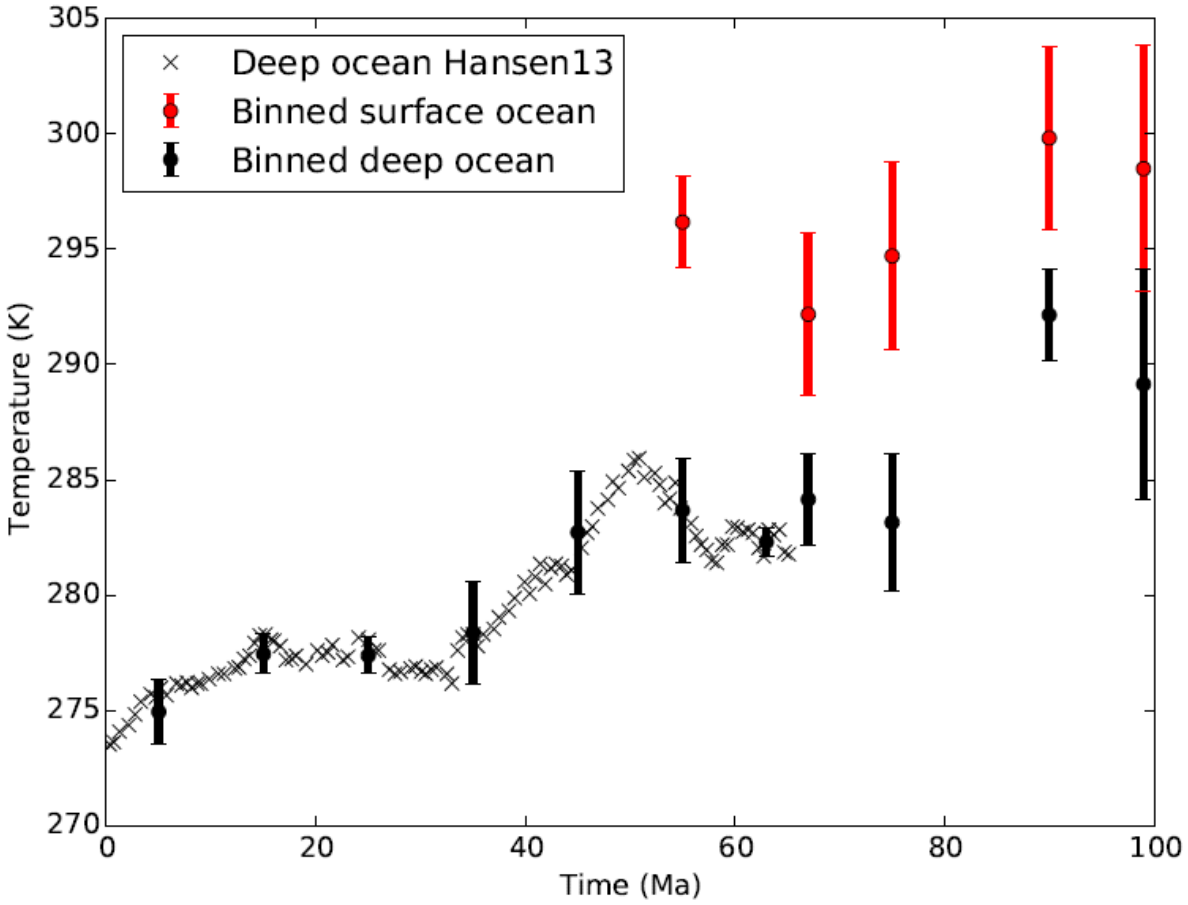

Supplementary Figure 12: Black and red circles show binned mean temperature values for the deep ocean and the surface, respectively. The proxy data used to construct these ranges is described in Supplementary Methods. Black crosses show Cenozoic deep ocean temperatures from Hansen *et al.*[17].

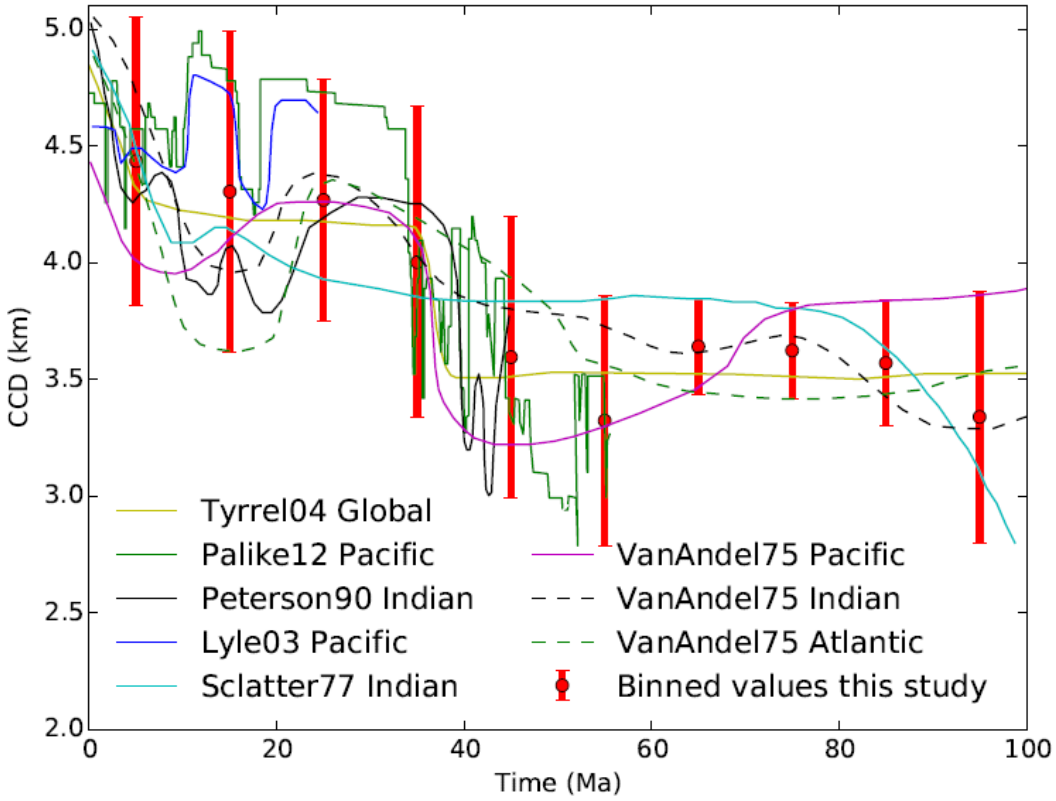

Supplementary Figure 13: Colored lines show estimates of Calcite Compensation Depth (CCD) for various ocean basins from the literature[3,18-22]. The red circles are the 10 Ma binned data used in this study. The uncertainty envelope for each binned data point is taken to be the range of reconstructions within that 10 Ma bin.

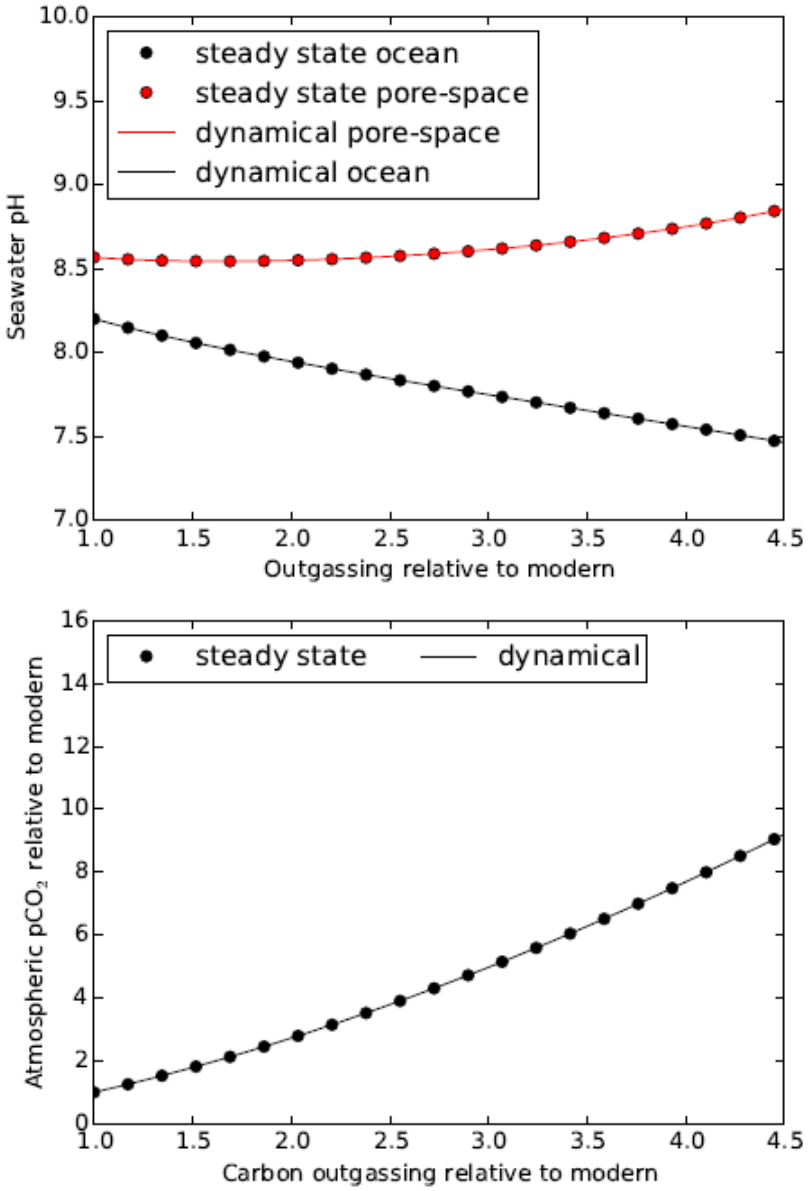

Supplementary Figure 14: Comparison of dynamical model (solid lines) and steady state calculations (circles). Supplementary Note 3 describes steady state calculations in full detail. There is excellent agreement between the two methods.

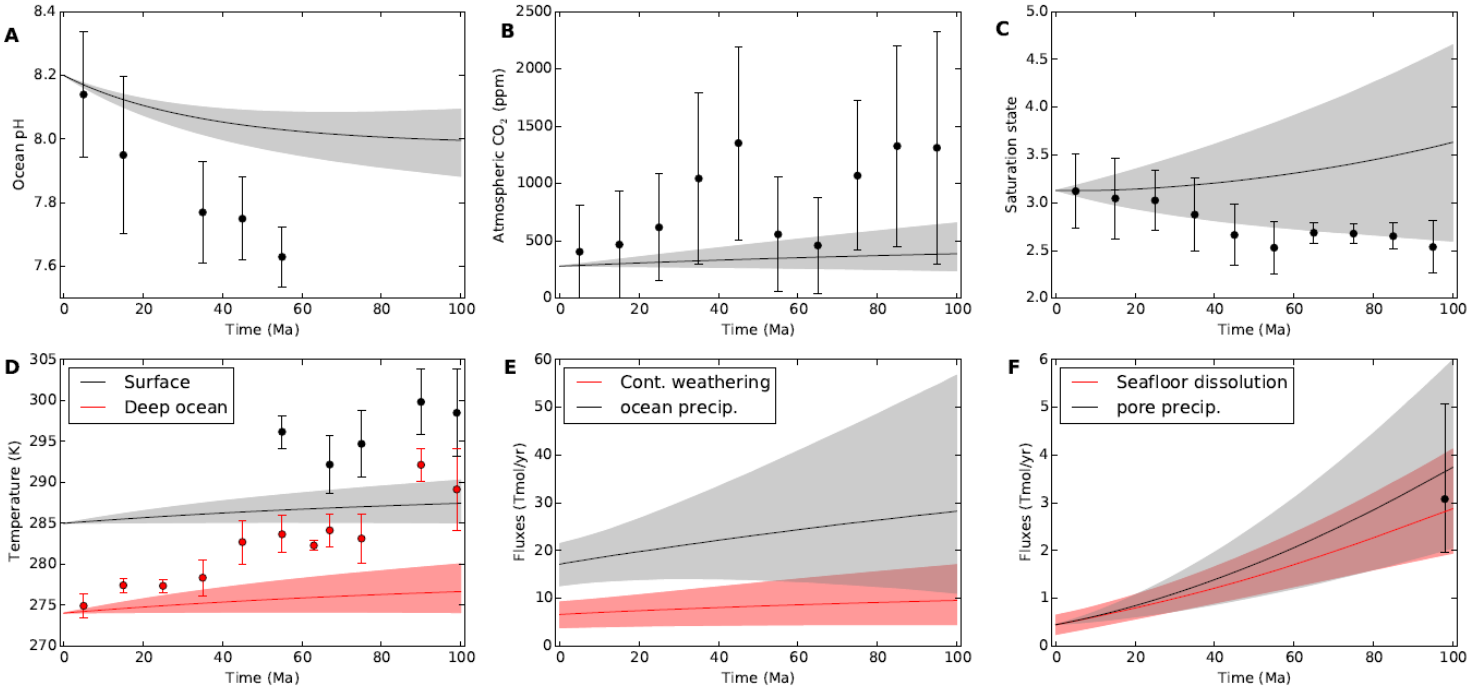

Supplementary Figure 15: An additional alkalinity source has been introduced in the pore space to account for K-feldspar formation (see Supplementary Note 4). Grey and red shaded regions represent the model output 90% confidence obtained from 10,000 forward model runs using the parameter ranges described in Table 1. The grey and red solid lines are the median model outputs. Black and red dots represent binned geochemical proxy data, and error bars denote the range of binned proxy estimates (see main text for references and explanation). The fit with pore-space precipitation is improved at the expense of a temperature and pH mismatch.

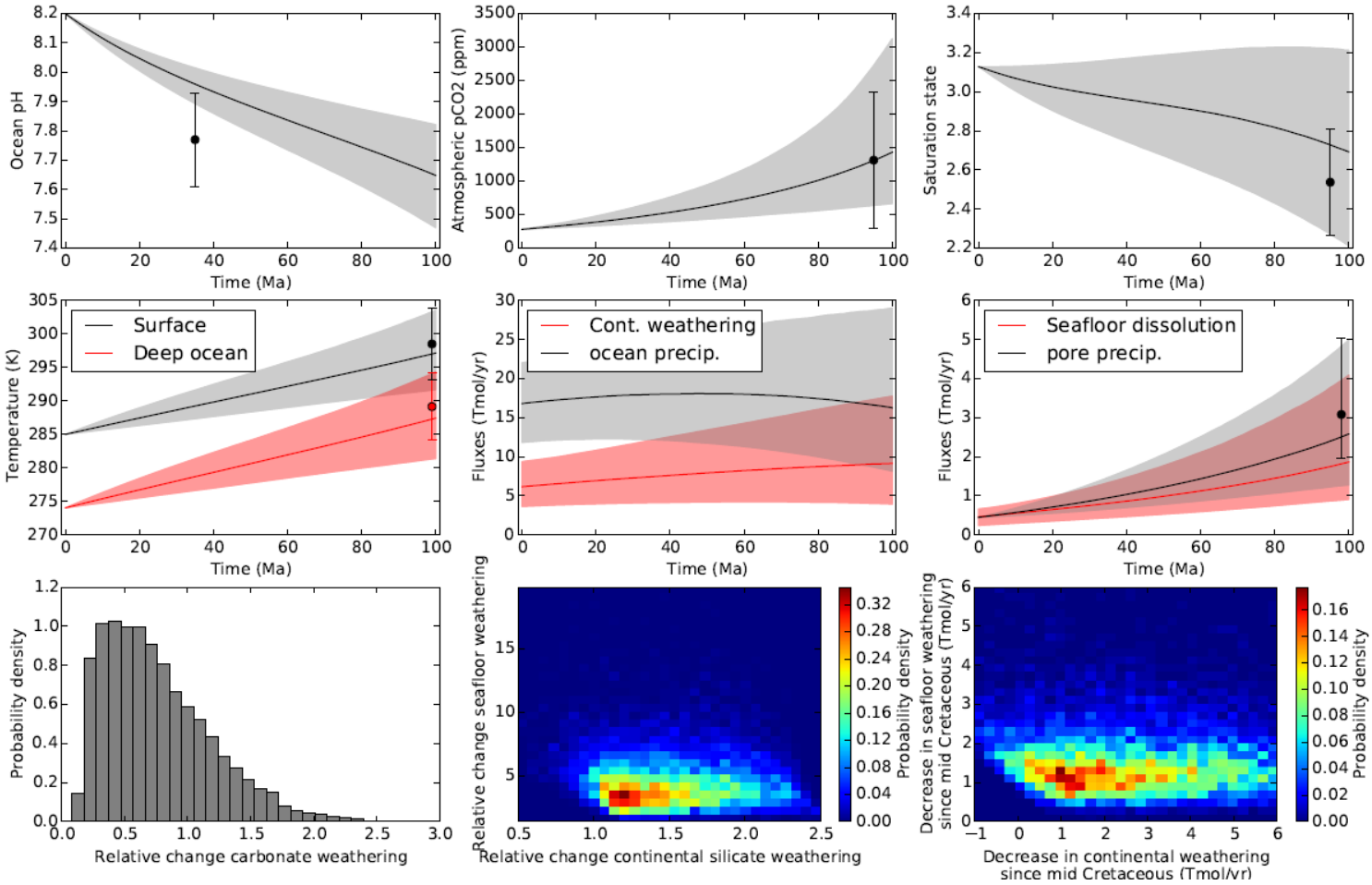

Supplementary Figure 16: Results of Bayesian inversion with limited data set. Each variable is fitted to a single mid Cretaceous data point (Cenozoic data point used for pH since no Cretaceous data exist). 1σ uncertainties in each data point are plotted, and shaded regions represent 95% credible intervals.

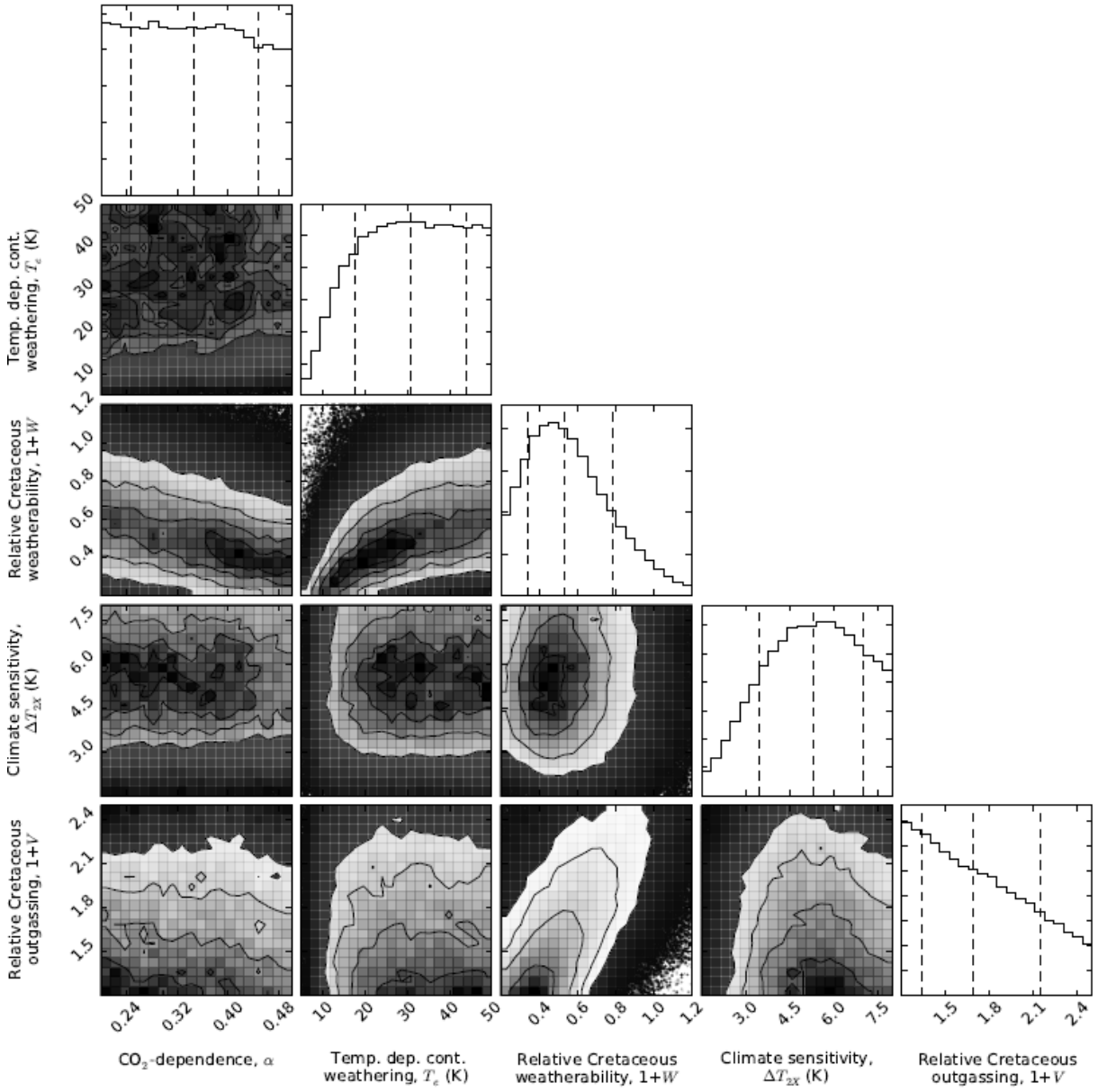

Supplementary Figure 17: Selected posterior probability distributions for the Bayesian inversion in Supplementary Fig. 16. Dotted lines represent the median value with 1σ error bars. The off-diagonal elements are joint probability distributions, which show how each pair of variables co-varies. Even when fitting a single mid Cretaceous data point for each variable – and thereby limiting the potential biases from underfitting and linearizing parameters - the general conclusions reported in the main text remain unchanged. Specifically, T_e is likely to be large, relative Cretaceous weatherability, 1+*W*, is approximately half modern weatherability, ΔT_{2x} is probably higher than fast feedback estimates.

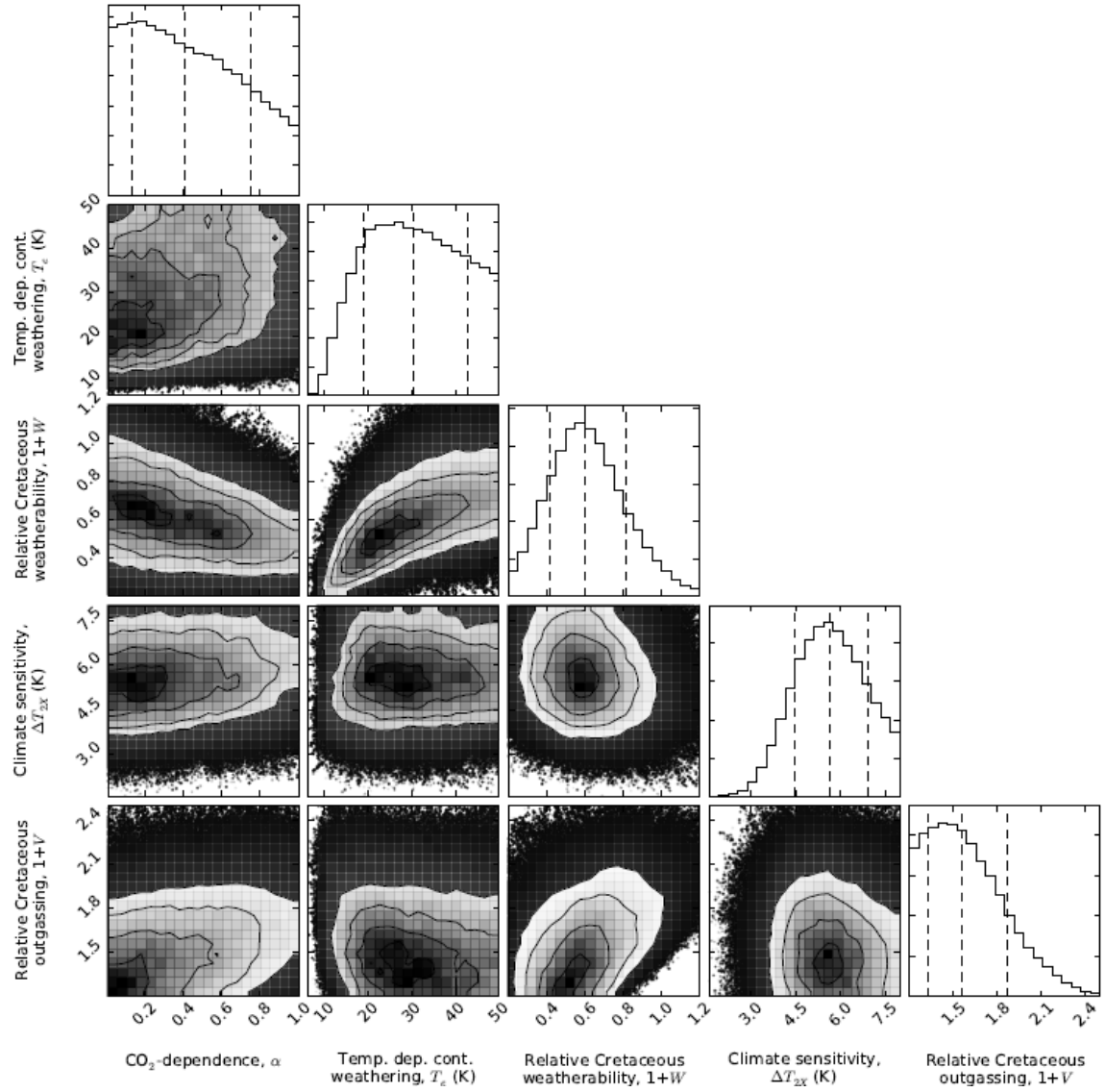

Supplementary Figure 18: Selected posterior probability distributions for a modified continental weathering function. The outer diagonal elements are the marginal distributions, and the off-diagonal elements are joint probability distributions, which show how each pair of variables co-varies. Dotted lines represent the median value with 1σ error bars. In this case the Michaelis-Menton law is adopted for the direct pCO_2 dependence of continental weathering (case 1). The 90% confidence intervals are $T_e = 14-48\,\mathrm{K}$, $1+W = 0.31-0.96$, and $\Delta T_{2x} = 3.8-7.6\,\mathrm{K}$.

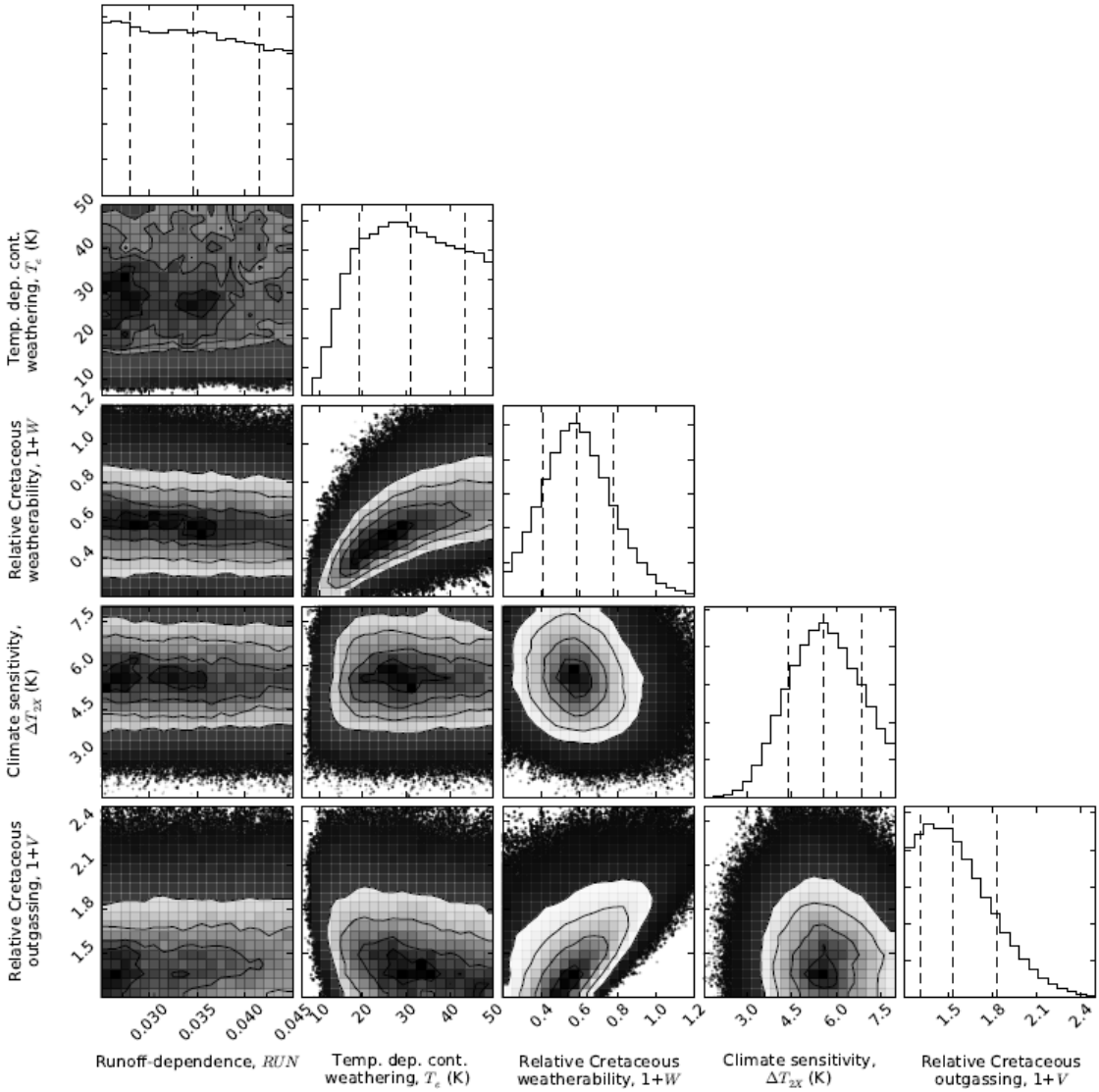

Supplementary Figure 19: Selected posterior probability distributions for a modified continental weathering function. The outer diagonal elements are the marginal distributions, and the off-diagonal elements are joint probability distributions, which show how each pair of variables co-varies. Dotted lines represent the median value with 1σ error bars. In this case the direct pCO_2 dependence of continental weathering is omitted and a linear runoff dependence is added (case 2). The 90% confidence intervals are $T_e = 14-48\,\mathrm{K}$, $1+W = 0.31-0.91$, and $\Delta T_{2x} = 3.7-7.5\,\mathrm{K}$.

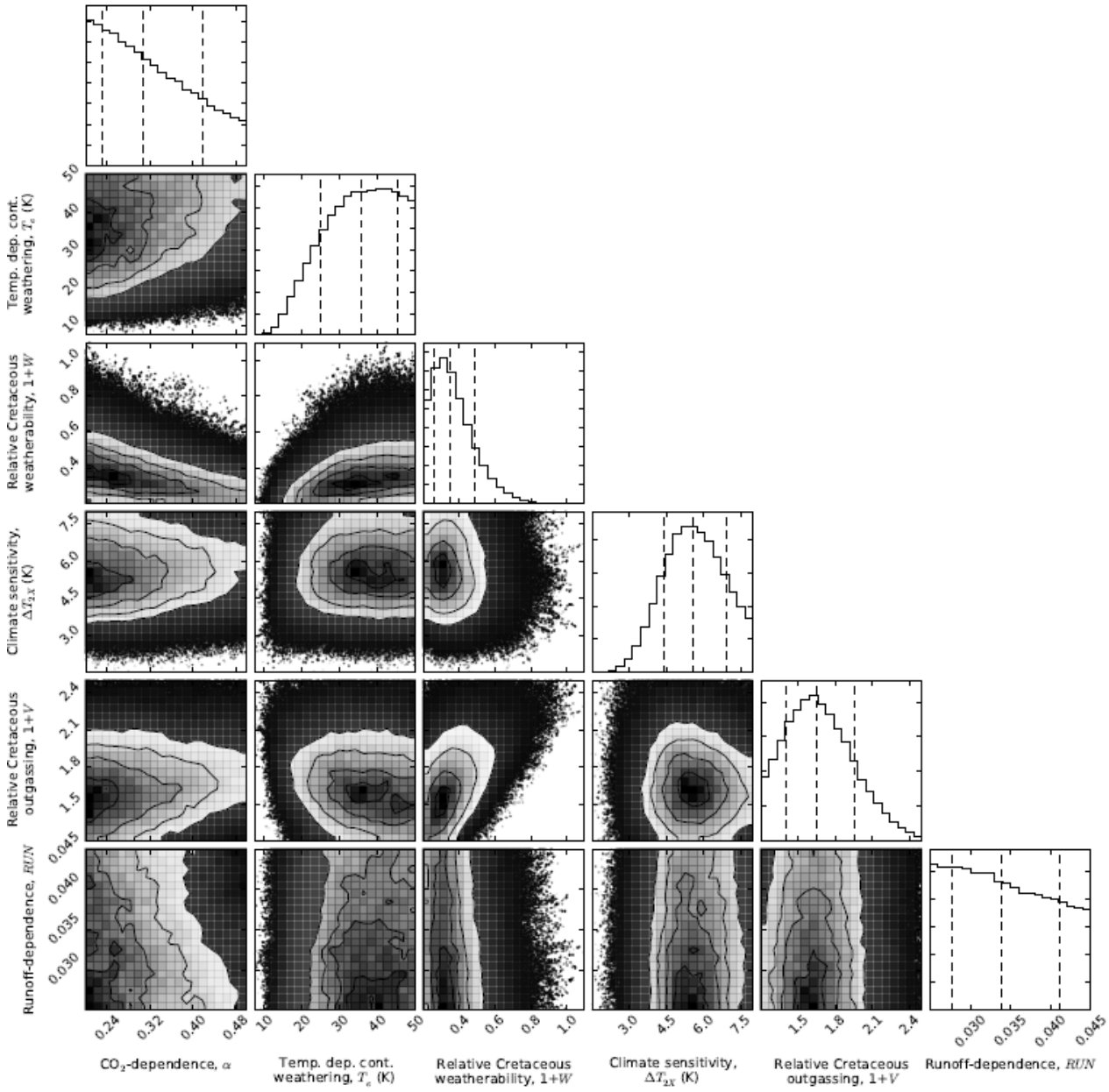

Supplementary Figure 20: Selected posterior probability distributions for a modified continental weathering function. The outer diagonal elements are the marginal distributions, and the off-diagonal elements are joint probability distributions, which show how each pair of variables co-varies. Dotted lines represent the median value with 1σ error bars. In this case the power law direct pCO_2 dependence of continental weathering is retained and a linear runoff dependence is added (case 3). The 90% confidence intervals are $T_e = 19-48\,\mathrm{K}$, $1+W = 0.22-0.60$, and $\Delta T_{2\mathrm{x}} = 3.7-7.6\,\mathrm{K}$.

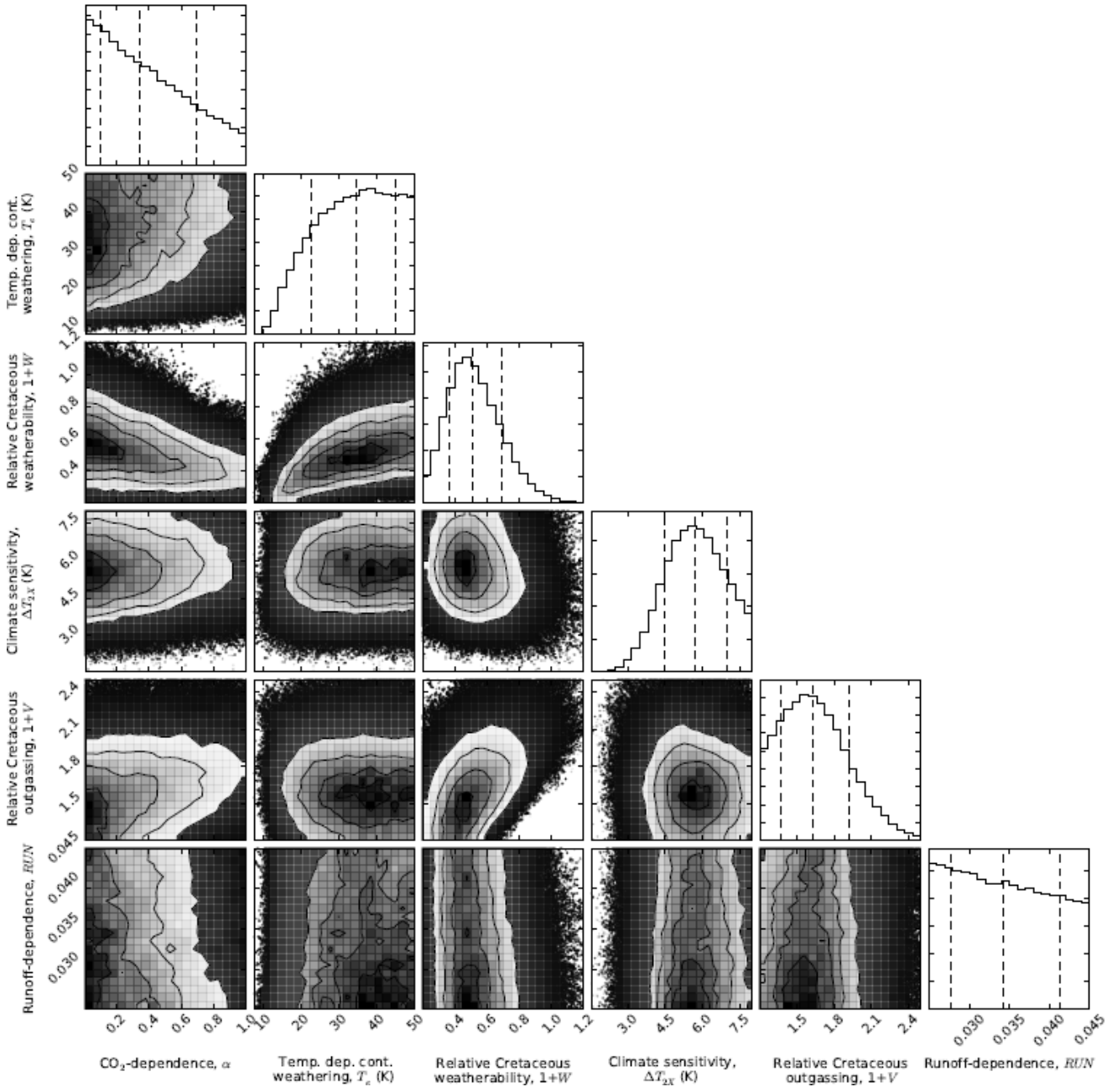

Supplementary Figure 21: Selected posterior probability distributions for a modified continental weathering function. The outer diagonal elements are the marginal distributions, and the off-diagonal elements are joint probability distributions, which show how each pair of variables co-varies. Dotted lines represent the median value with 1σ error bars. In this case the Michaelis-Menton law is adopted for the direct pCO_2 dependence of continental weathering and a linear runoff dependence is added (case 4). The 90% confidence intervals are $T_e = 17 - 48\ \mathrm{K}$, $1+W = 0.28 - 0.83$, and $\Delta T_{2x} = 3.8 - 7.6\ \mathrm{K}$.

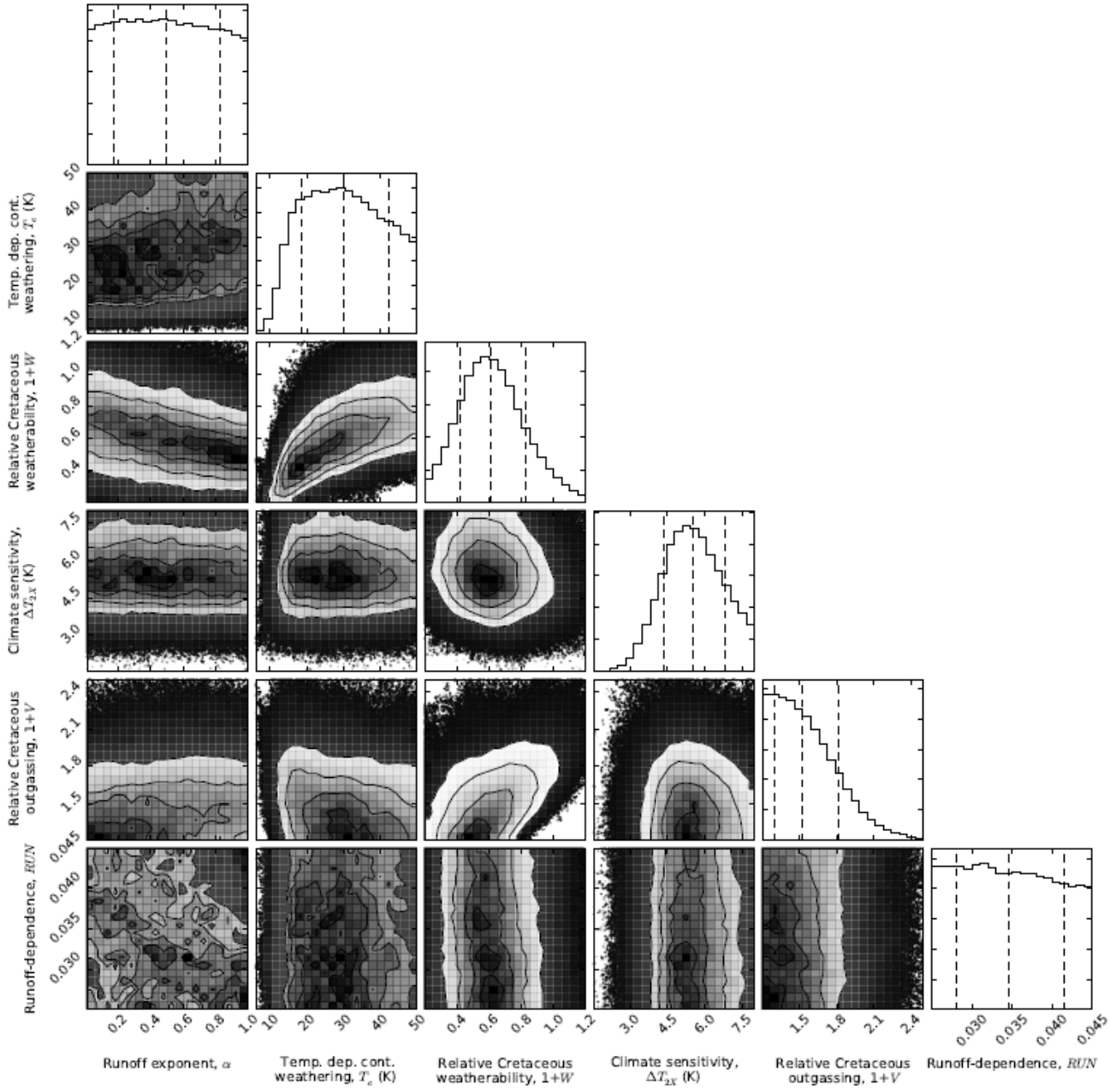

Supplementary Figure 22: Selected posterior probability distributions for a modified continental weathering function. The outer diagonal elements are the marginal distributions, and the off-diagonal elements are joint probability distributions, which show how each pair of variables co-varies. Dotted lines represent the median value with 1σ error bars. In this case the direct pCO_2 dependence of continental weathering is omitted and a linear runoff dependence is added with an additional runoff exponent (case 5). The 90% confidence intervals are $T_e = 14-47$ K, $1+W = 0.31-0.98$, and $\Delta T_{2x} = 3.7-7.5$ K.

Supplementary Note 1: Climate and deep-ocean temperature parameterizations

The Global Circulation Model (GCM) outputs used in Fig. 8 were taken from Li *et al.*[23], Stouffer and Manabe[24], and Danabasoglu and Gent[25]. These studies were chosen because they used fully coupled atmosphere-ocean GCMs with complete ocean circulation. Each GCM was run for thousands of years, which is sufficient time for the deep ocean to reach equilibrium.

Paleocene-Eocene Thermal Maximum (PETM) temperatures were sourced from Jones *et al.*[26]. The peak-PETM mean surface temperature, 27.3°C, was obtained by averaging all the reported temperatures in Table 1 of Jones *et al.*[26], and weighting each measurement by the cosine of its latitude. The pre-PETM mean surface temperature, 23.03°C, was obtained by subtracting the best-fit warming (4.3°C) from the peak-PETM temperature, although directly averaging pre-PETM measurements produced a similar result. Deep ocean pre-PETM and peak-PETM temperatures were estimated from Table 2 of Jones *et al.*[26]. Observed deep ocean temperatures were weighted by the areas of their respective ocean basins, and the pre-PETM and peak-PETM averages were found to be 12.1°C and 16.5°C, respectively. Error bars for PETM proxy temperatures were estimated as follows: McInerney and Wing[27] and Higgins and Schrag[28] estimate 5-8°C surface warming during the PETM, and so we adopted an error of 2°C in both the peak-PETM and pre-PETM surface temperatures.

Last Glacial Maximum (LGM) temperatures were estimated as follows. Clark *et al.*[29] gave the modern deep sea temperature as 1.3°C and the change since the LGM as 3.25±0.55°C. This implies the LGM deep ocean temperature was -2.2±0.55°C. Similarly, Schneider von Deimling *et al.*[30] estimated the mean surface cooling during the LGM to be 5.8±1.4°C, whereas Annan and Hargreaves[31] estimated the surface cooling to be 4±0.8°C. We averaged these estimates to obtain the mean surface cooling as 4.9±1.6°C, or equivalently the mean surface temperature 8.8±1.6°C.

Supplementary Fig. 9 shows the range of climate parameterizations considered in our model alongside selected GCM outputs and other simple climate models from the literature. The GCM outputs were taken from Li *et al.*[23], Stouffer and Manabe[24], Danabasoglu and Gent[25], Hansen *et al.*[32], and Meraner *et al.*[33]. The simple climate models were sourced from Abbot *et al.*[34], Walker *et al.*[35], Lenton[36], Pierrehumbert[37], and Kasting[38].

Supplementary Note 2: Climate model

The solar luminosity term in our climate model (equation (9)) was derived as follows. Doubling atmospheric CO_2 is equivalent to a 3.7 W m^{-2} radiative forcing[39]. Taking into account the geometry of insolation and assuming an albedo of 0.3, the solar luminosity decrease required to offset a 3.7 W m^{-2} radiative forcing is:

$$\left(4\times 3.7\ \mathrm{W/m^2}\right)\Big/\left(0.7\times 1366\ \mathrm{W/m^2}\right)=0.01548=1.5\% \qquad \text{(S1)}$$

Following Catling and Kasting[40] the evolution of relative solar luminosity, L, is approximated by:

$$L = \frac{1}{\left(1 + 0.4\left(t/4600\ \mathrm{Ma}\right)\right)} \tag{S2}$$

We seek the time, t (in Ma), that luminosity was 1.5% reduced relative to modern. Solving $0.9485 = 1/\left(1 + 0.4\left(t/4600\ \mathrm{Ma}\right)\right)$ yields $t = 181\ \mathrm{Ma}$ for the time at which the solar forcing was $-3.7\ \mathrm{W/m^2}$. If we were to assume that global temperatures respond to pCO_2 forcings in the same way as equivalent luminosity forcings then our climate equation would have the form (neglecting paleogeography):

$$\Delta T_{\mathrm{S}} = \Delta T_{2\mathrm{x}} \left(\frac{\ln\left(\mathrm{pCO_2}/\mathrm{pCO_2^{mod}}\right)}{\ln\left(2\right)} - \frac{t}{181\,Ma} \right) \tag{S3}$$

However, mean surfaces are slightly more sensitive to pCO_2 changes than to luminosity changes because the CO_2 forcing is more effective at high latitudes[41]. Hansen *et al.*[41] reported CO_2 forcings to be 1.26 times more effective than luminosity forcings and so we adopt this correction in our climate equation (neglecting paleogeography):

$$\Delta T_{\mathrm{S}} = \Delta T_{2\mathrm{x}} \left(\frac{\ln\left(\mathrm{pCO_2}/\mathrm{pCO_2^{mod}}\right)}{\ln\left(2\right)} - \frac{t}{1.26 \times 181\,Ma} \right) \tag{S4}$$

The linear paleogeography term is described in the main text.

Supplementary Note 3: Validation of dynamical model with steady-state calculations

To validate our model we compared outputs to equivalent steady state calculations. To make the steady state calculations analytically tractable, it is necessary to simplify the dynamical equations somewhat. Many different cases were validated, and here we present one illustrative example. In this example the only sources/sinks are carbon outgassing, pore-space precipitation, and pore space basalt dissolution, i.e. no carbonate or silicate weathering. We also assume $s = 0$. Equation (6) can therefore be simplified to:

$$\begin{aligned}
\frac{dC_{\mathrm{O}}}{dt} &= -J\left(C_{\mathrm{O}} - C_{\mathrm{P}}\right)/M_{\mathrm{O}} + F_{\mathrm{out}}/M_{\mathrm{O}} \\
\frac{dA_{\mathrm{O}}}{dt} &= -J\left(A_{\mathrm{O}} - A_{\mathrm{P}}\right)/M_{\mathrm{O}} \\
\frac{dC_{\mathrm{P}}}{dt} &= J\left(C_{\mathrm{O}} - C_{\mathrm{P}}\right)/M_{\mathrm{P}} - P_{\mathrm{pore}}/M_{\mathrm{P}} \\
\frac{dA_{\mathrm{P}}}{dt} &= J\left(A_{\mathrm{O}} - A_{\mathrm{P}}\right)/M_{\mathrm{P}} + 2F_{\mathrm{diss}}/M_{\mathrm{P}} - 2\,P_{\mathrm{pore}}/M_{\mathrm{P}}
\end{aligned} \tag{S5}$$

The model was forced by increasing outgassing from modern to 4.5x modern levels over several billion years. Rather than specify calcium abundances, in this example we let $\left[\mathrm{Ca^{2+}}\right]$ evolve dynamically with alkalinity:

$$\left[\mathrm{Ca}^{2+}\right] = 0.5(\left[\mathrm{ALK}\right] - \left[\mathrm{ALK}\right]_{\mathrm{initial}}) + \left[\mathrm{Ca}^{2+}\right]_{\mathrm{initial}} \quad \text{(S6)}$$

Additionally, we ignore the pH dependence of basalt dissolution and assume dissolution is purely a function of temperature: $F_{\mathrm{diss}} = k_{\mathrm{T}} \exp\left(-E_{\mathrm{bas}} / RT_{\mathrm{pore}}\right)$. Selected model outputs from this dynamical calculation are plotted in Supplementary Fig. 14.

The same problem was also solved by computing successive steady states. Starting from the initial (modern) steady state for the ocean and pore space, outgassing was incrementally increased up to 4.5x modern levels, and the new steady state was found at each outgassing level. This calculation is described in full below. In the equations that follow, P-subscripts denote pore-space variables, and O-subscripts denote ocean variables.

Steady state in equations (S5) implies that $F_{\mathrm{diss}} = P_{\mathrm{pore}} = F_{\mathrm{out}}$. Because dissolution is a function of deep ocean temperature only, T_{D}, T_{S} and pCO_2 can be calculated from equations (9) and (12). Similarly, since P_{pore} is known, Ω_{P} can be calculated from equation (19). In other words the steady state conditions allow us to determine pCO_2 and Ω_{P} for any given level of outgassing, and from these two variables the complete carbon chemistry of the ocean and pore space can be solved simultaneously. By substituting equations (23) and (24) into equations (21) we obtain:

$$\begin{aligned}
\mathrm{ALK}_{\mathrm{P}} &= \left[\mathrm{CO}_3^{2-}\right]_{\mathrm{P}} \left(2 + \frac{\left[\mathrm{H}^+\right]_{\mathrm{P}}}{\mathrm{K}_2^*} \right) \\
\mathrm{DIC}_{\mathrm{P}} &= \left[\mathrm{CO}_3^{2-}\right]_{\mathrm{P}} \left(1 + \frac{\left[\mathrm{H}^+\right]_{\mathrm{P}}}{\mathrm{K}_2^*} + \frac{\left[\mathrm{H}^+\right]_{\mathrm{P}}^2}{\mathrm{K}_1^*\mathrm{K}_2^*} \right) \\
\therefore \mathrm{ALK}_{\mathrm{P}} - \mathrm{DIC}_{\mathrm{P}} &= \left[\mathrm{CO}_3^{2-}\right]_{\mathrm{P}} \left(1 - \frac{\left[\mathrm{H}^+\right]_{\mathrm{P}}^2}{\mathrm{K}_1^*\mathrm{K}_2^*} \right)
\end{aligned} \quad \text{(S7)}$$

Next, the first expression in equation (S7) can be rearranged and substituted into the third expression as follows:

$$
\begin{aligned}
\left[H^+\right]_P &= K_2^* \left(\frac{ALK_P}{\left[CO_3^{2-}\right]_P} - 2 \right) \\
\therefore \left[H^+\right]_P^2 &= \left(K_2^*\right)^2 \left(\frac{ALK_P - 2\left[CO_3^{2-}\right]_P}{\left[CO_3^{2-}\right]_P} \right)^2 \\
\therefore ALK_P - DIC_P &= \left[CO_3^{2-}\right]_P \left(1 - \frac{K_2^*}{K_1^*} \left(\frac{ALK_P - 2\left[CO_3^{2-}\right]_P}{\left[CO_3^{2-}\right]_P} \right)^2 \right) \\
&= \left[CO_3^{2-}\right]_P - \frac{K_2^*}{K_1^*} \left(\frac{ALK_P^{\,2} - 4\,ALK_P\left[CO_3^{2-}\right]_P + 4\left[CO_3^{2-}\right]_P^2}{\left[CO_3^{2-}\right]_P} \right)
\end{aligned}
\tag{S8}
$$

This can then be rearranged to obtain a quadratic in $\left[CO_3^{2-}\right]_P$:

$$
\begin{aligned}
\left(ALK_P - DIC_P\right)\left[CO_3^{2-}\right]_P &= \left[CO_3^{2-}\right]_P^2 - \frac{K_2^*}{K_1^*}\left(ALK_P^{\,2} - 4\,ALK_P\left[CO_3^{2-}\right]_P + 4\left[CO_3^{2-}\right]_P^2\right) \\
\therefore \left[CO_3^{2-}\right]_P^2 \left(1 - 4\frac{K_2^*}{K_1^*}\right) + \left[CO_3^{2-}\right]_P \left(4\frac{K_2^*}{K_1^*}ALK_P + DIC_P - ALK_P\right) - \frac{K_2^*}{K_1^*}ALK_P^{\,2} &= 0
\end{aligned}
\tag{S9}
$$

Denote the solution to this quadratic $\left[CO_3^{2-}\right]_P = X\left(ALK_P, DIC_P\right)$. The steady state condition also implies $DIC_P = DIC_O - F_{out}/J$, and so we can substitute this into the quadratic solution to obtain

$$
\left[CO_3^{2-}\right]_P = X\left(ALK_P, DIC_O - F_{out}/J\right) \tag{S10}
$$

Next, we use equations (23) and (21) to express $1/\left[H^+\right]_O$ in terms of pCO_2 and ALK_P:

$$
\begin{aligned}
\frac{K_1^*\left[CO_2\,aq\right]_O}{\left[H^+\right]_O} = \left[HCO_3^-\right]_O &= \left(ALK_O - 2\left[CO_3^{2-}\right]_O\right) = \left(ALK_O - \frac{2K_1^*K_2^*\left[CO_2\,aq\right]_O}{\left[H^+\right]_O^2}\right) \\
\therefore \frac{2K_1^*K_2^*}{\left[H^+\right]_O^2} + \frac{K_1^*}{\left[H^+\right]_O} - \frac{ALK_P}{\left[CO_2\,aq\right]_O} &= 0 \\
\therefore \frac{1}{\left[H^+\right]_O} = -K_1^* + \sqrt{\left(K_1^*\right)^2 + \frac{4K_1^*K_2^*ALK_O}{\left[CO_2\,aq\right]_O}} &= -K_1^* + \sqrt{\left(K_1^*\right)^2 + \frac{4K_1^*K_2^*ALK_P}{pCO_2 \times H_{CO_2}}}
\end{aligned}
\tag{S11}
$$

In the last line, we make use of the steady state condition $\mathrm{ALK_O}=\mathrm{ALK_P}$ and equation (22). Next, we use equations (21) to (24) to express $\mathrm{DIC_O}$ in terms of $1/\left[\mathrm{H^+}\right]_\mathrm{O}$ and $\mathrm{pCO_2}$:

$$\begin{aligned}\mathrm{DIC_O} &= \left[\mathrm{CO_3^{2-}}\right]_\mathrm{O} + \left[\mathrm{HCO_3^-}\right]_\mathrm{O} + \left[\mathrm{CO_2aq}\right]_\mathrm{O} \\ &= \left[\mathrm{CO_2aq}\right]_\mathrm{O}\left(\frac{\mathrm{K_1^*K_2^*}}{\left[\mathrm{H^+}\right]_\mathrm{O}^2} + \frac{\mathrm{K_1^*}}{\left[\mathrm{H^+}\right]_\mathrm{O}} + 1\right) \\ &= \mathrm{pCO_2}\times\mathrm{H_{CO_2}}\left(\frac{\mathrm{K_1^*K_2^*}}{\left[\mathrm{H^+}\right]_\mathrm{O}^2} + \frac{\mathrm{K_1^*}}{\left[\mathrm{H^+}\right]_\mathrm{O}} + 1\right)\end{aligned} \tag{S12}$$

Equation (S11) can now be substituted into equation (S12), yielding $\mathrm{DIC_O}$ as a function of purely $\mathrm{pCO_2}$ and $\mathrm{ALK_P}$. This combined expression can be substituted into our quadratic solution (S10), which results in an expression for $\left[\mathrm{CO_3^{2-}}\right]_\mathrm{P}$ that is purely a function of $\mathrm{ALK_P}$ and $\mathrm{pCO_2}$:

$$\left[\mathrm{CO_3^{2-}}\right]_\mathrm{P} = \mathrm{X}\left(\mathrm{ALK_P}, \mathrm{DIC_O}\left(\mathrm{pCO_2}\right) - F_{\mathrm{out}}/J\right) \tag{S13}$$

Finally, from equations (20) and (S6) we have the pore-space saturation state:

$$\begin{aligned}\Omega_\mathrm{P} &= \frac{\left[\mathrm{Ca^{2+}}\right]_\mathrm{P}\left[\mathrm{CO_3^{2-}}\right]_\mathrm{P}}{\mathrm{K_{sp}}} = \frac{\left(1/2\left(\left[\mathrm{ALK}\right]_\mathrm{P} - \left[\mathrm{ALK}\right]_{\text{P-initial}}\right) + \left[\mathrm{Ca^{2+}}\right]_{\text{P-initial}}\right)\left[\mathrm{CO_3^{2-}}\right]_\mathrm{P}}{\mathrm{K_{sp}}} \\ &= \frac{\left(1/2\left(\left[\mathrm{ALK}\right]_\mathrm{P} - \left[\mathrm{ALK}\right]_{\text{P-initial}}\right) + \left[\mathrm{Ca^{2+}}\right]_{\text{P-initial}}\right)\mathrm{X}\left(\mathrm{ALK_P}, \mathrm{DIC_O}\left(\mathrm{pCO_2}\right) - F_{\mathrm{out}}/J\right)}{\mathrm{K_{sp}}}\end{aligned} \tag{S14}$$

In this expression, the only unknown is $\mathrm{ALK_P}$ (recall that Ω_P and $\mathrm{pCO_2}$ are readily calculated from steady state conditions). It is therefore possible to solve this equation numerically to find $\mathrm{ALK_P}$. Once $\mathrm{ALK_P} = \mathrm{ALK_O}$ is known, $\mathrm{DIC_O}$ can be calculated from equations (S12) and (S11), and the remaining carbon chemistry is trivially solved using equations (21) to (26) in the main text. The results from this steady state calculation are plotted in Supplementary Fig. 14 and compared to equivalent dynamical model outputs. They are in agreement, which implies that the numerical integration is working correctly, and that the carbon cycle is in quasi-steady state.

Supplementary Note 4: Modified models – K-feldspar uptake

A caveat on our results is that the assumed functional relationship for seafloor weathering (equation (13)) does not accommodate the influence of changing seawater chemistry on basalt dissolution other than pH changes and imposed [Ca^{2+}] variation. Despite variations in the

continental weathering source, seawater [K^+] concentration has remained remarkably constant over the Phanerozoic[42]. This could be explained by uptake in K-feldspar in the seafloor[43]. A seafloor buffer on [K^+] is potentially significant for the carbon cycle because K-uptake in K-feldspar formation releases [Ca^{2+}] with ~7:2 stoichiometric ratio (see below), and so enhanced continental supply of K^+ could result in alkalinity release and carbonate formation in the seafloor, thereby providing an additional negative feedback on pCO_2 [43].

The stoichiometry of K-feldspar formation implies that the addition of 2.5 wt% CO_2 to oceanic crust requires the addition of 0.75 wt% of K_2O [43]:

$$\begin{aligned} &2NaAlSi_3O_8 + 7CaAl_2Si_2O_8 + 2K^+ + 8SiO_2 \\ &+5CO_2 + 2HCO_3^- + 5H_2O \\ &= 2KAlSi_3O_8 + 2NaAl_7Si_{11}O_{30}(OH)_6 + 7CaCO_3 \end{aligned} \quad \text{(S15)}$$

Varying K-feldspar uptake can be incorporated in our model with an additional alkalinity source in the pore-space. Cretaceous crust K_2O content is approximately 0.4 wt% greater than Cenozoic crust [43], which implies up to 1.3 wt% CO_2 added from K-feldspar formation. To crudely incorporate this ALK source into our model we modified equation (6) as follows:

$$\frac{dA_P}{dt} = J\left(A_O - A_P\right)/M_P + 2F_{diss}/M_P - 2P_{pore}/M_P + \frac{t \times 1.3 \times 10^{12}\left(F_{out}/F_{out}^{mod}\right)}{100\ Ma \times M_P} \quad \text{(S16)}$$

For typical changes in crustal production, $F_{out}/F_{out}^{mod} = 1.5$, the alkalinity source due to K-feldspar formation will be ~2 Tmol eq yr^{-1} at 100 Ma and 0 Tmol eq yr^{-1} in the modern pore-space.

Including this alkalinity source does not affect our conclusions. For the base case (no weatherability change, *W*=0, and conventional temperature dependence of silicate weathering, $T_e = 5-15$ K) the seafloor precipitation flux at 100 Ma is a better fit with data, however the fit with temperature and CO_2 is worsened. The combination of a strong silicate weathering feedback and a large seafloor sink due to K-feldspar formation draws down too much pCO_2 and makes the Cretaceous climate unreasonably cold (Supplementary Fig. 15). If either the temperature sensitivity of silicate weathering is weakened or a large weatherability increase is imposed, then the fit with temperature and CO_2 is marginal. The best fit is achieved by assuming both a weak climate sensitivity ($T_e = 30-40$ K) and a large weatherability change (*W*=0.4-0.6), not shown. In short, a sizeable change in weatherability and/or a low temperature dependence of silicate weathering is still required to fit proxy data.

Supplementary Note 5: Modified models –Fitting the mid Cretaceous mean state

One potential criticism of our methodology is that by imposing linear trends on some variables in our model we do not fully capture shorter timescale fluctuations. By fitting binned time series data in this way we are arguably underfitting and potentially underestimating the true uncertainty in unknown variables. To test this we repeated the MCMC inversion but simplified the data to include only one mid Cretaceous data point for each variable. By only fitting the mid Cretaceous

endpoint the misfit from imposing linear trends is minimized. In this calculation we are no longer fitting a time series but rather fitting mean Cretaceous conditions with broad uncertainties.

The model outputs for this calculation are shown in supplementary figures 16 and 17. Although the uncertainties in fitted parameters are somewhat larger than the nominal case, key conclusions are unchanged: a large weatherability increase is probable, the temperature sensitivity of continental weathering is weak, and Earth system climate sensitivity is likely to be higher than fast-feedback estimates. A high Earth system climate sensitivity is supported by numerous paleoclimate studies[44-47].

Supplementary Note 6: Modified models – Different functional forms for continental weathering

The precise functional form for continental weathering is uncertain, and so we repeated our inverse analysis using five different functional forms for continental silicate and carbonate weathering to see how the choice of function affected the probability distributions for key parameters).

Case 1 (Table 1 and Fig. 6 main text): Replace power law pCO_2 dependence with Michaelis-Menton law[48,49]:

$$F_{\mathrm{sil}} = \omega F_{\mathrm{sil}}^{\mathrm{mod}} \left(\frac{2R_{\mathrm{CO_2}}}{1+R_{\mathrm{CO_2}}} \right)^{\alpha} \exp\left(\Delta T_{\mathrm{S}}/T_e\right)$$
$$F_{\mathrm{carb}} = \omega_{\mathrm{carb}} \omega F_{\mathrm{carb}}^{\mathrm{mod}} \left(\frac{2R_{\mathrm{CO_2}}}{1+R_{\mathrm{CO_2}}} \right)^{\alpha} \exp\left(\Delta T_{\mathrm{S}}/T_e\right) \quad \text{(S17)}$$

This expression represents the effect of CO_2 fertilization on vascular land plants. The unknown exponent, α, represents the efficiency of CO_2 fertilization. We vary α across the full range from 0 to 1 in our inverse analysis such that it encompasses the endmember case where there is no direct pCO_2 dependence. For most of this range, the Michaelis-Menton law provides a weaker pCO_2 dependence than the original power law. For simplicity we adopt the same functional form for carbonate weathering as for silicate weathering, but recall the carbonate weathering function contains an additional free weatherability parameter to account for any differences with silicate weathering. Selected case 1 results are presented in the main text in Table 1 and Fig. 6.

Case 2: No direct pCO_2 dependence and linear runoff dependence. The direct pCO_2 dependence of silicate weathering adopted in the main text is uncertain and potentially overstated. Here, we omit any pCO_2 dependence and instead use the functional forms for silicate weathering adopted in field studies (e.g. [50,51]) with an Arrhenius temperature dependence and linear runoff dependence. We relate runoff to temperature using an expression from the COPSE model[52], $runoff = (1 + RUN \times \Delta T)^{0.65}$.

$$F_{\mathrm{sil}} = \omega F_{\mathrm{sil}}^{\mathrm{mod}} \left(1 + RUN \times \Delta T_{\mathrm{S}}\right)^{0.65} \exp\left(\Delta T_{\mathrm{S}} / T_e\right)$$
$$F_{\mathrm{carb}} = \omega_{\mathrm{carb}} \omega F_{\mathrm{carb}}^{\mathrm{mod}} \left(1 + RUN \times \Delta T_{\mathrm{S}}\right)^{0.65} \exp\left(\Delta T_{\mathrm{S}} / T_e\right) \quad \text{(S18)}$$

Here, *RUN* is a proportionality constant that relates changes in surface temperature to changes in runoff. We adopt the range *RUN*=0.025-0.045 which spans glacial to greenhouse conditions[53].

Case 3: Power law direct pCO_2 dependence and linear runoff dependence.

$$F_{\mathrm{sil}} = \omega F_{\mathrm{sil}}^{\mathrm{mod}} \left(R_{\mathrm{CO_2}}\right)^{\alpha} \exp\left(\Delta T_{\mathrm{S}} / T_e\right)\left(1 + RUN \times \Delta T_{\mathrm{S}}\right)^{0.65}$$
$$F_{\mathrm{carb}} = \omega_{\mathrm{carb}} \omega F_{\mathrm{carb}}^{\mathrm{mod}} \left(R_{\mathrm{CO_2}}\right)^{\alpha} \exp\left(\Delta T_{\mathrm{S}} / T_e\right)\left(1 + RUN \times \Delta T_{\mathrm{S}}\right)^{0.65} \quad \text{(S19)}$$

Here α ranges from 0.2 to 0.5 as in the main text, and *RUN* ranges from 0.025 to 0.045 as above.

Case 4: Michaelis-Menton law for pCO_2 dependence and linear runoff dependence.

$$F_{\mathrm{sil}} = \omega F_{\mathrm{sil}}^{\mathrm{mod}} \left(\frac{2R_{\mathrm{CO_2}}}{1 + R_{\mathrm{CO_2}}}\right)^{\alpha} \exp\left(\Delta T_{\mathrm{S}} / T_e\right)\left(1 + RUN \times \Delta T_{\mathrm{S}}\right)^{0.65}$$
$$F_{\mathrm{carb}} = \omega_{\mathrm{carb}} \omega F_{\mathrm{carb}}^{\mathrm{mod}} \left(\frac{2R_{\mathrm{CO_2}}}{1 + R_{\mathrm{CO_2}}}\right)^{\alpha} \exp\left(\Delta T_{\mathrm{S}} / T_e\right)\left(1 + RUN \times \Delta T_{\mathrm{S}}\right)^{0.65} \quad \text{(S20)}$$

Here α=0-1 and *RUN*=0.025-0.045.

Case 5: No direct pCO_2 dependence and linear runoff dependence with unknown exponent. Rather than adopt the runoff expression adopted in the COPSE[52] model, we instead assume the runoff exponent is unknown and allow it to vary freely from 0 to 1. This allows for a wide range of runoff sensitivities to climate:

$$F_{\mathrm{sil}} = \omega F_{\mathrm{sil}}^{\mathrm{mod}} \exp\left(\Delta T_{\mathrm{S}} / T_e\right)\left(1 + RUN \times \Delta T_{\mathrm{S}}\right)^{\alpha}$$
$$F_{\mathrm{carb}} = \omega_{\mathrm{carb}} \omega F_{\mathrm{carb}}^{\mathrm{mod}} \exp\left(\Delta T_{\mathrm{S}} / T_e\right)\left(1 + RUN \times \Delta T_{\mathrm{S}}\right)^{\alpha} \quad \text{(S21)}$$

Here α=0-1 is the runoff exponent and *RUN*=0.025-0.045 is the runoff sensitivity.

Supplementary figures 18-22 show the posterior distributions for key parameters for cases 1-5, respectively. We observe that the distribution for climate sensitivity is virtually unchanged by the choice of weathering function. This is unsurprising since climate sensitivity is controlled by the functional form of the climate equation and pCO_2 and temperature proxies. Similarly, weak temperature sensitivity of continental weathering (large T_e) is required in all five cases, consistent with our original analysis (T_e=17-48 K, 90% confidence). A slightly stronger temperature dependence is more probable for cases 1, 2 and 5 (T_e≈14-48 K, 90% confidence). This is expected because if the direct pCO_2 dependence of continental weathering is weak

(case 1, Michaelis-Menton law) or absent (cases 2 and 5), then some temperature sensitivity is required to ensure continental weathering can respond to changes in climate and fit proxies. In the cases with a stronger pCO_2 dependence (case 3) or an additional temperature dependence (case 4, runoff dependence), a weaker Arrhenius relationship (larger T_e) is more probable.

Finally, a smaller increase in weatherability since 100 Ma is more probable in cases 1, 2, and 5 than in the original results. This can also be understood in terms of a weaker or absent direct pCO_2 dependence: without a pCO_2 dependence decreasing continental weathering since 100 Ma, the counterbalancing increase in weatherability does not need to be as large in order to fit proxies.

In summary, the choice of functional form for continental weathering does not change any of our qualitative conclusions, namely climate sensitivity is large, the temperature dependence of continental weathering is weak, and there has been a sizeable increase in weatherability since 100 Ma due to factors other than climate. However, our quantitative estimates of key variables – particularly the weatherability change – could be refined by a better mechanistic understanding of continental weathering on the global scale.

Supplementary Note 7: Silicate weathering and outgassing

From equation (2) we have $F_{\mathrm{sil}} \propto F_{\mathrm{sil}}^{\mathrm{mod}} \exp\left(\Delta T_{\mathrm{S}}/T_e\right)$. This can be rearranged to obtain $\Delta T_{\mathrm{S}} \propto T_e \ln\left(F_{\mathrm{sil}}/F_{\mathrm{sil}}^{\mathrm{mod}}\right)$, and so the change in surface temperature required to double the silicate weathering flux is given by $\Delta T_{\mathrm{S}} \propto T_e \ln\left(2\right)$. This expression and the 1σ values for T_e in Table 1 were used to compute the doubling temperatures reported in the abstract.

The outgassing reconstructions in Fig. 7 are sourced from Van Der Meer *et al.*[54] (blue), Vérard *et al.*[55] (red), Cogné and Humler[56] (aqua), Seton *et al.*[57] (purple), Hansen and Wallmann[58] (green), and Berner[48] (GEOCARB, yellow). These reconstructions were chosen because they rely on several independent lines of evidence: reconstructions of plate extent and plate motion based on field geology, paleogeography and paleomagentic data[55], seismic imaging of subducted plates to infer variations in subducted plate length over time[54], and reconstructions of seafloor age and depth[56,57]. As noted in the main text, the outlying Cogné and Humler[56] reconstruction is disputed[57,59].

Supplementary Methods

Ocean chemistry

The saturation state for calcite is calculated using the following expression from Pilson[60], p. 410-411:

$$\log\left(\mathrm{K_{sp}}\right) = \log\left(\mathrm{K_{sp}^{o}}\right) + \left(-0.77712 + 0.0028426T + 178.34/T\right)35^{0.5} - 0.07711\times 35 + 0.0041249\times 35^{1.5} \quad \text{(S22)}$$

$$\textit{where} \quad \log\left(\mathrm{K_{sp}^{o}}\right) = -171.9065 - 0.077993T + \frac{2839.319}{T} + 71.595\log\left(T\right)$$

Here, T is the temperature of the ocean or pore-space. A constant salinity of 35 parts per thousand is assumed in this expression. Note that we have not included a correction for changing Mg^{2+} abundances (e.g. ref [3]). Hain *et al.*[61] showed that including an Mg^{2+} correction factor introduced significant error to $\mathrm{K_{sp}}$. This is because the empirical correction factor is normally offset by changes in $\mathrm{K_2^*}$ (defined in equation (S23)). The most accurate approach, short of implementing the Pitzer equations, is to use the standard, fixed thermodynamic constants[61]. We omit the pressure dependence of the solubility product because pressure is not varying through time (multiplication by a constant would not change model outputs since fluxes are scaled to fit modern fluxes).

The Henry's law constant, $\mathrm{H_{CO_2}}$, and the first and second apparent dissociation constants of carbonic acid, $\mathrm{K_1^*}$ and $\mathrm{K_2^*}$ respectively, were calculated using the expressions in Pilson[60], p. 111:

$$\begin{aligned} &\log\left(\mathrm{H_{CO_2}}\right) = \frac{9345.17}{T} - 167.8108 + 23.3585\log\left(T\right) \\ &+\left(.023517 - 2.3656\times 10^{-4}T + 4.7036\times 10^{-7}T^2\right)\times 35 \\ &p\mathrm{K_1^*} = 17.788 - 0.073104T - 0.0051087\times 35 + 1.1463\times 10^{-4}T^2 \\ &p\mathrm{K_2^*} = 20.919 - 0.064209T - 0.011887\times 35 + 8.7313\times 10^{-5}T^2 \end{aligned} \quad \text{(S23)}$$

For simplicity and computational efficiency we used a constant T=291.15 K in equation (S23), which is the modern surface ocean temperature (surface oceans are warmer than the continents plus oceans average of 285 K). We conducted test model runs with large changes in T and found that it doesn't change observable parameters (pH, CO_2, carbon fluxes, saturation state) appreciably. Using temperature-dependent constants results in only moderate changes in alkalinity and carbonate speciation.

Derivation of equation (25)

From the definition of carbon abundance (Tmol C kg^{-1}) in the atmosphere-ocean box we have:

$$
\begin{aligned}
C &= \mathrm{DIC} + s \times \mathrm{pCO_2} \\
&= \left[\mathrm{CO_3^{2-}}\right] + \left[\mathrm{HCO_3^-}\right] + \left[\mathrm{CO_2aq}\right] + \frac{s\left[\mathrm{CO_2aq}\right]}{\mathrm{H_{CO_2}}} \\
&= \left[\mathrm{CO_3^{2-}}\right] + \frac{\left[\mathrm{H^+}\right]\left[\mathrm{CO_3^{2-}}\right]}{\mathrm{K_2^*}} + \frac{\left[\mathrm{H^+}\right]^2\left[\mathrm{CO_3^{2-}}\right]}{\mathrm{K_1^*K_2^*}} + \frac{s\left[\mathrm{H^+}\right]^2\left[\mathrm{CO_3^{2-}}\right]}{\mathrm{H_{CO_2}\,K_1^*K_2^*}} \\
&= \left[\mathrm{CO_3^{2-}}\right]\left(1 + \frac{\left[\mathrm{H^+}\right]}{\mathrm{K_2^*}} + \frac{\left[\mathrm{H^+}\right]^2}{\mathrm{K_1^*K_2^*}}\left(1 + \frac{s}{\mathrm{H_{CO_2}}}\right)\right)
\end{aligned}
\tag{S24}
$$

For the atmosphere-ocean reservoir, $s = n_{\mathrm{atm}} / M_{\mathrm{O}}$, where $n_{\mathrm{atm}} = 1.8 \times 10^{20}$ is the total number of moles in the atmosphere and M_{O} is the ocean mass in kg. For the pore-space $s = 0$ because the pore-space is not in contact with any gaseous reservoir of carbon.

Next, from the definition of alkalinity in the atmosphere-ocean box we have:

$$
\begin{aligned}
\mathrm{ALK} &= 2\left[\mathrm{CO_3^{2-}}\right] + \left[\mathrm{HCO_3^-}\right] \\
&= 2\left[\mathrm{CO_3^{2-}}\right] + \frac{\left[\mathrm{H^+}\right]\left[\mathrm{CO_3^{2-}}\right]}{\mathrm{K_2^*}} \\
&= \left[\mathrm{CO_3^{2-}}\right]\left(2 + \frac{\left[\mathrm{H^+}\right]}{\mathrm{K_2^*}}\right)
\end{aligned}
\tag{S25}
$$

Combining equations (S24) and (S25) gives:

$$
\begin{aligned}
&\mathrm{ALK}\left(1 + \frac{\left[\mathrm{H^+}\right]}{\mathrm{K_2^*}} + \frac{\left[\mathrm{H^+}\right]^2}{\mathrm{K_1^*K_2^*}}\left(1 + \frac{s}{\mathrm{H_{CO_2}}}\right)\right) = C\left(2 + \frac{\left[\mathrm{H^+}\right]}{\mathrm{K_2^*}}\right) \\
&\frac{\mathrm{ALK}}{\mathrm{K_1^*K_2^*}}\left(1 + \frac{s}{\mathrm{H_{CO_2}}}\right)\left[\mathrm{H^+}\right]^2 + \left(\frac{\mathrm{ALK} - C}{\mathrm{K_2^*}}\right)\left[\mathrm{H^+}\right] + \mathrm{ALK} - 2C = 0
\end{aligned}
\tag{S26}
$$

This quadratic can be solved to find the $\left[\mathrm{H^+}\right]$ molality in either the ocean or the pore space.

Proxy records

This section describes the geochemical proxy data plotted in Fig. 2, 3, 4, 5, and supplementary figures 2, 15, and 16.

Ocean pH

Ocean pH estimates were taken from Anagnostou *et al.*[4], Tripati *et al.*[5], Foster *et al.*[6] and Bartoli *et al.*[7]. Data from Edgar *et al.*[8] and Pearson *et al.*[9] recalculated using the methodology of

Anagnostou *et al.*[4] were also used. Supplementary Fig. 10 shows all the data considered in this study and the 10 Ma binned data that were used in the forward modeling and inverse analyses described in the main text.

Ocean pH is typically inferred from boron isotope data. Boron speciation is pH dependent, and so ocean pH can be estimated from boron isotopes in carbonates, assuming the boron isotopic composition of seawater and the fractionation factor are known[62]. Anagnostou *et al.*[4] rigorously constrained Cenozoic ocean pH using a broad range of estimates for boron isotope vital effects and seawater isotopic composition. The resulting data form the basis of the pH dataset in this study. However, the uncertainty in these ocean pH estimates may still be underestimated if the computed values do not reflect a globally integrated signal. In the modern ocean, surface pH varies by at least 0.2 log units[63].

Atmospheric CO_2

Supplementary Fig. 11 shows the CO_2 proxy data considered in this analysis and the 10 Ma binned data that were used in the forward modeling and inverse analyses described in the main text. Cenozoic pCO_2 proxies were taken from Beerling and Royer[10]. This exhaustive compilation includes stomatal, paleosol, phytoplankton, liverwort, and boron-based estimates and represents a consensus reconstruction.

Cretaceous pCO_2 proxies were taken from Hong and Lee[11] (pedogenic carbonates), Franks *et al.*[12] (stomatal model), Fletcher *et al.*[13] (fossil bryophytes), Retallack[14] (stomatal index), Quan *et al.*[15] (stomatal index) and Barclay *et al.*[16] (stomatal index). Traditionally, isotopic methods such as those using pedogenic carbonates yield higher pCO_2 estimates than those from stomatal methods[64]. This discrepancy was partially resolved by Breecker *et al.*[65] who revaluated soil CO_2 concentrations downward yielding lower atmospheric pCO_2 estimates from pedogenic carbonates. However, Cretaceous pCO_2 estimates based on the Breecker *et al.*[65] methodology[11] remain significantly higher than recent contemporaneous stomatal estimates[12]. These recent stomatal estimates are based on a mechanistic model of leaf exchange rather than an empirical fit to stomatal indices and are arguably more accurate at high pCO_2[12]. However, the sensitivity of this model-based approach to parameter assumptions was highlighted by McElwain *et al.*[66], who concluded that Franks *et al.*[12] could have underestimated atmospheric pCO_2. In short, the discrepancy between stomatal and paleosol pCO_2 estimates remains unresolved. Consequently, we include data from both methods in Supplementary Fig. 11 and use the full range of proxy estimates to define the uncertainty in each 10 Ma interval.

Temperature

Paleocene-Eocene Thermal Maximum (PETM) temperatures are described in Supplementary Note 1. Cretaceous temperatures were estimated as follows. Deep ocean temperatures were taken from Fig. 3 in Huber *et al.*[67]. The four timespans reported in Huber *et al.*[67] are 66.5-68.5 Ma, 75.4-76.4 Ma, 92-94 Ma, 99-100 Ma, and for each interval deep ocean temperatures from benthic foraminifera were averaged across all latitudes to obtain 11°C, 10°C, 19°C, 16°C, respectively. The errors in these temperature estimates were taken to be 2°C, 3°C, 2°C, 5°C, respectively, based on the spread of data points in Fig. 3 in Huber *et al.*[67].

There is a broad range of estimates for Cretaceous mean surface temperatures in the literature. For example Hay and Floegel[68] presented a time series curve based on Frakes[69] and Frakes *et al.*[70] that gives the following surface averages: 22.6°C, 25.6°C, 30.7°C and 30.7°C for 65-70 Ma, 70-80 Ma, 85-95 Ma, and 95-105 Ma, respectively. However, a simple latitudinal average of temperatures in Frakes[69] (weighted by latitude) yields 15.5°C, 17.5°C, 22.7°C, and 20°C for the same set of intervals. Huber *et al.*[67] doesn't report mean surface temperatures, but a crude averaging of surface temperatures in their Fig. 4 suggests values of 17°C, 20°C, 27°C, and 28°C for the same time intervals. Simple latitude-weighted SST averages from Li and Keller[71] yields 18.5°C for 75 Ma and 15.4°C for 65 Ma. In this study we take a conservative approach by letting the smallest and largest reported surface temperatures for each timespan define our confidence interval, and use the midpoint as the best estimate. This yields the following Cretaceous mean surface temperatures: 19.0±3.5°C for 65-70 Ma, 21.6±4.1°C for 70-80 Ma, 26.7±4.0°C for 85-95 Ma, and 25.4±5.4°C for 95-105 Ma.

Cenozoic deep ocean temperatures were sourced from Hansen *et al.*[17]. We omit plotting Cenozoic surface temperatures for lack of a consensus time-series for globally averaged temperatures. Supplementary Fig. 12 summarizes all the temperature data used in this study, and shows the binned ranges used in the inverse analysis and forward modeling.

Saturation state

Supplementary Fig. 13 shows the variety of CCD reconstructions considered in this study[3,18-22]. The ranges of CCD reconstructions in each 10 Ma interval were used as the consensus CCD in this study. The CCD was converted to a saturation state using equation 4 in Jansen *et al.*[72]:

$$\Omega = k_{CCD} \exp\left(0.189\left(Z_{CCD} - 3.82\right)\right) \quad \text{(S27)}$$

Here k_{CCD} is chosen to match the modern saturation state in our model. Uncertainty in the Cretaceous saturation state is potentially underestimated because only a small number of independent studies sample this timespan.

Seafloor weathering

Estimates of the Cenozoic and Cretaceous seafloor precipitation fluxes were based on Gillis and Coogan[73]: The upper 300 m of Cenozoic-aged drill cores have CO_2 contents of 0.4±0.2 and 0.5±0.2 wt% (excluding young warm sites with extensive sediment cover). Thus the mean upper crust carbon content is 0.45±0.2 wt%. Gillis and Coogan[73] convert this to a carbon flux by assuming the modern crustal formation rate is 3 $km^2\ yr^{-1}$, and then multiplying the resultant flux by a factor of 1.5 to correct for the lower crust contribution. Conveniently, the net effect of this conversion is equivalent to multiplying by $(10^{12}/1.5)\times1.5$, and so wt% CO_2 can be easily converted to Tmol C yr^{-1} by multiplication by 10^{12}. Thus the initial value for the Cenozoic pore-space precipitation flux is 0.45 Tmol C yr^{-1} (Table 2). In contrast, Mills *et al.*[74] assumed a modern seafloor sink of 1.72 Tmol C yr^{-1} in their carbon cycle model. However, this flux was obtained from indiscriminately averaging the carbonate content in both Cenozoic and Mesozoic

oceanic crust. Overestimating the modern seafloor weathering flux will inflate the importance of the seafloor weathering sink at earlier times in Earth's history.

The upper 300 m of Cretaceous-aged drill cores have CO_2 contents of 2.4±0.7, 1.9±0.3, which gives a best-estimate of 2.35±0.75 wt% using the range method adopted for the other proxies. The cretaceous seafloor precipitation flux will therefore be (2.35±0.75)×(1+V)$^{\beta}$ Tmol C yr^{-1}, where we have multiplied by the Cretaceous crustal production rate relative to modern. The error bars for the Cretaceous pore-space flux in Fig. 2, 3, 4, 5, and supplementary figures 2, 15, and 16 were obtained by sampling our assumed range for V and calculating the inferred range of fluxes. For the Bayesian analysis, the observed precipitation sink was calculated for each forward model call by multiplying by (1+V)$^{\beta}$.

Isotopic constraints

Isotopic records provide potentially powerful constraints on carbon cycle processes e.g. ref [75]. However, we have deliberately avoided using Sr, Os, or Li isotope records to constrain our model due to uncertainties in their respective interpretations. For example, the upward trend in $^{87}Sr/^{86}Sr$ over the Cenozoic has multiple interpretations (see main text), and the Li isotope record cannot be straightforwardly related to continental weathering fluxes[76-78].

Bayesian inversion

The log-likelihood function used in the Bayesian inversion is defined as follows[79]:

$$\log\left(L\right) = -\frac{1}{2}\left(\sum_{k}\sum_{i}\frac{\left(OBS_{i,k} - MOD_{i,k}\right)^{2}}{\sigma_{i,k}^{2}}\right) - \frac{1}{2}\sum_{k}\sum_{i}\log\left(2\pi\sigma_{i,k}^{2}\right) \qquad \text{(S28)}$$

Here, $OBS_{i,k}$, $MOD_{i,k}$, and $\sigma_{i,k}$ are the observed (proxy) value, model value, and uncertainty in the observed value of the i-th data point of the k-th variable, respectively. The k summation is over the six variables for which we have proxy records: mean surface temperature, mean deep ocean temperature, atmospheric pCO_2, ocean saturation state, ocean pH, and pore-space precipitation flux. The i summation is over the binned data plotted in the time series figures in the main text (Fig. 2, 3, 4, 5, and supplementary figures 2, 15, and 16), and described above.

The Bayesian analysis was implemented using the 'emcee' package in Python[80] and posterior distribution figures were created using the 'corner' module in Python. The emcee package implements an affine-invariant MCMC ensemble sampler. We used 1000 walkers and 10,000 model steps – that is a total of 10 million forward model calls – to build posterior distributions for our parameters. After accounting for autocorrelation in the walkers, the effective sample size was ~100,000. The initial walker positions were randomized, and a 1000 step burn-in was discarded. Approximately three quarters of walkers have crossed the median parameter value by 1000 steps, indicating that this burn-in is adequate. The 95% credible intervals plotted in Fig. 5 are the 2.5th-97.5th percentile range in the distribution of walkers.

A small number of studies have applied Bayesian methods to carbon cycle models. For

example, Royer *et al.*[81] and Park and Royer[45] adopted GEOCARBSULF[82] as a forward model and pCO_2 proxies to constrain Earth system climate sensitivity. Because these studies used pCO_2 proxies for the entire Phanerozoic they could estimate climate sensitivity separately for glacial and non-glacial periods. However, their retrieval only used pCO_2 to constrain model parameters and did not make use of temperature, saturation state, pH, and seafloor carbonate proxies. Additionally, the retrieval in Park and Royer[45] is dependent on the detailed parameterizations within GEOCARBSULF. Although some parameters such as silicate weathering activation energy and biological modifiers on weatherability were allowed to vary in Park and Royer[45], assumptions about the carbon and strontium isotope records and continental land area through time are 'hard-wired' into GEOCARBSULF. In contrast, we have deliberately designed our forward model to be as general as possible: isotope records were not used to force our model, and outgassing, carbonate and silicate weatherability, and modern-day fluxes are all free parameters. Consequently, the conclusions from our Bayesian analysis are more robust to model assumptions.

Supplementary References

1 Volk, T. Feedbacks between weathering and atmospheric CO2 over the last 100 million years *Am. J. Sci* **287,** 763-779 (1987).

2 Walker, L. J., Wilkinson, B. H. & Ivany, L. C. Continental drift and Phanerozoic carbonate accumulation in shallow-shelf and deep-marine settings *The Journal of Geology* **110,** 75-87 (2002).

3 Tyrrell, T. & Zeebe, R. E. History of carbonate ion concentration over the last 100 million years *Geochimica et Cosmochimica Acta* **68,** 3521-3530 (2004).

4 Anagnostou, E., John, E. H., Edgar, K. M., Foster, G. L., Ridgwell, A., Inglis, G. N. *et al.* Changing atmospheric CO2 concentration was the primary driver of early Cenozoic climate *Nature* **533,** 380-384 (2016).

5 Tripati, A. K., Roberts, C. D. & Eagle, R. A. Coupling of CO2 and ice sheet stability over major climate transitions of the last 20 million years *science* **326,** 1394-1397 (2009).

6 Foster, G. L., Lear, C. H. & Rae, J. W. The evolution of pCO 2, ice volume and climate during the middle Miocene *Earth and Planetary Science Letters* **341,** 243-254 (2012).

7 Bartoli, G., Hönisch, B. & Zeebe, R. E. Atmospheric CO2 decline during the Pliocene intensification of Northern Hemisphere glaciations *Paleoceanography* **26,** (2011).

8 Edgar, K. M., Anagnostou, E., Pearson, P. N. & Foster, G. L. Assessing the impact of diagenesis on δ 11 B, δ 13 C, δ 18 O, Sr/Ca and B/Ca values in fossil planktic foraminiferal calcite *Geochimica et Cosmochimica Acta* **166,** 189-209 (2015).

9 Pearson, P. N., Foster, G. L. & Wade, B. S. Atmospheric carbon dioxide through the Eocene–Oligocene climate transition *Nature* **461,** 1110-1113 (2009).

10 Beerling, D. J. & Royer, D. L. Convergent cenozoic CO2 history *Nature Geoscience* **4,** 418-420 (2011).

11 Hong, S. K. & Lee, Y. I. Evaluation of atmospheric carbon dioxide concentrations during the Cretaceous *Earth and Planetary Science Letters* **327,** 23-28 (2012).

12 Franks, P. J., Royer, D. L., Beerling, D. J., Van de Water, P. K., Cantrill, D. J., Barbour, M. M. *et al.* New constraints on atmospheric CO2 concentration for the Phanerozoic *Geophysical Research Letters* **41,** 4685-4694 (2014).

13 Fletcher, B. J., Beerling, D. J., Brentnall, S. J. & Royer, D. L. Fossil bryophytes as recorders of ancient CO2 levels: experimental evidence and a Cretaceous case study *Global Biogeochemical Cycles* **19,** (2005).

14 Retallack, G. J. A 300-million-year record of atmospheric carbon dioxide from fossil plant cuticles *Nature* **411,** 287-290 (2001).

15 Quan, C., Sun, C., Sun, Y. & Sun, G. High resolution estimates of paleo-CO 2 levels through the Campanian (Late Cretaceous) based on Ginkgo cuticles *Cretaceous Research* **30,** 424-428 (2009).

16 Barclay, R. S., McElwain, J. C. & Sageman, B. B. Carbon sequestration activated by a volcanic CO2 pulse during Ocean Anoxic Event 2 *Nature Geoscience* **3,** 205-208 (2010).

17 Hansen, J., Sato, M., Russell, G. & Kharecha, P. Climate sensitivity, sea level and atmospheric carbon dioxide *Philosophical Transactions of the Royal Society of London A: Mathematical, Physical and Engineering Sciences* **371,** 20120294 (2013).

18 Pälike, H., Lyle, M. W., Nishi, H., Raffi, I., Ridgwell, A., Gamage, K. *et al.* A Cenozoic record of the equatorial Pacific carbonate compensation depth *Nature* **488,** 609-614 (2012).

19 Van Andel, T. H. Mesozoic/Cenozoic calcite compensation depth and the global distribution of calcareous sediments *Earth and Planetary Science Letters* **26,** 187-194 (1975).

20 Lyle, M. Neogene carbonate burial in the Pacific Ocean *Paleoceanography* **18,** (2003).

21 Sclater, J. G., Abbott, D. & Thiede, J. Paleobathymetry and sediments of the Indian Ocean *Indian Ocean Geology and Biostratigraphy* 25-59 (1977).

22 Peterson, L. C. & Backman, J. in *ODP, Texas A&M University, College Station; UK distributors, IPOD Committee, NERC, Swindon.*

23 Li, C., von Storch, J.-S. & Marotzke, J. Deep-ocean heat uptake and equilibrium climate response *Climate Dynamics* **40,** 1071-1086 (2013).

24 Stouffer, R. & Manabe, S. Equilibrium response of thermohaline circulation to large changes in atmospheric CO2 concentration *Climate Dynamics* **20,** 759-773 (2003).

25 Danabasoglu, G. & Gent, P. R. Equilibrium climate sensitivity: Is it accurate to use a slab ocean model? *Journal of Climate* **22,** 2494-2499 (2009).

26 Jones, T. D., Lunt, D. J., Schmidt, D. N., Ridgwell, A., Sluijs, A., Valdes, P. J. *et al.* Climate model and proxy data constraints on ocean warming across the Paleocene–Eocene Thermal Maximum *Earth-Science Reviews* **125,** 123-145 (2013).

27 McInerney, F. A. & Wing, S. L. The Paleocene-Eocene Thermal Maximum: A perturbation of carbon cycle, climate, and biosphere with implications for the future *Annual Review of Earth and Planetary Sciences* **39,** 489-516 (2011).

28 Higgins, J. A. & Schrag, D. P. Beyond methane: towards a theory for the Paleocene–Eocene thermal maximum *Earth and Planetary Science Letters* **245,** 523-537 (2006).

29 Clark, P. U., Dyke, A. S., Shakun, J. D., Carlson, A. E., Clark, J., Wohlfarth, B. *et al.* The last glacial maximum *science* **325,** 710-714 (2009).

30 Schneider von Deimling, T., Ganopolski, A., Held, H. & Rahmstorf, S. How cold was the last glacial maximum? *Geophysical Research Letters* **33,** (2006).

31 Annan, J. & Hargreaves, J. A new global reconstruction of temperature changes at the Last Glacial Maximum *Climate of the Past* **9,** 367-376 (2013).

32 Hansen, J., Sato, M., Ruedy, R., Nazarenko, L., Lacis, A., Schmidt, G. *et al.* Efficacy of climate forcings *Journal of Geophysical Research: Atmospheres* **110,** (2005).

33 Meraner, K., Mauritsen, T. & Voigt, A. Robust increase in equilibrium climate sensitivity under global warming *Geophysical Research Letters* **40,** 5944-5948 (2013).

34 Abbot, D. S., Cowan, N. B. & Ciesla, F. J. Indication of insensitivity of planetary weathering behavior and habitable zone to surface land fraction *The Astrophysical Journal* **756,** 178 (2012).

35 Walker, J. C., Hays, P. & Kasting, J. F. A negative feedback mechanism for the long-term stabilization of Earth's surface temperature *Journal of Geophysical Research: Oceans (1978–2012)* **86,** 9776-9782 (1981).

36 Lenton, T. M. Land and ocean carbon cycle feedback effects on global warming in a simple Earth system model *Tellus B* **52,** 1159-1188 (2000).

37 Pierrehumbert, R. T. *Principles of planetary climate*. (Cambridge University Press, 2010).

38 Kasting, J. Proterozoic climates: the effect of changing atmospheric carbon dioxide concentrations *The Proterozoic Biosphere* 165-168 (1992).

39 IPCC. Climate change 2001: the scientific basis. Contribution of working group I to the third assessment report of the intergovernmental panel on climate change. Report No. 1477-8696, (Intergovernmental Panel on Climate Change, Cambridge, UK, 2001).

40 Catling, D. C. & Kasting, J. *Atmospheric Evolution on Inhabited and Lifeless Worlds*. (Cambridge University Press, 2017).

41 Hansen, J., Sato, M. & Ruedy, R. Radiative forcing and climate response *Journal of Geophysical Research: Atmospheres* **102,** 6831-6864 (1997).

42 Horita, J., Zimmermann, H. & Holland, H. D. Chemical evolution of seawater during the Phanerozoic: Implications from the record of marine evaporites *Geochimica et Cosmochimica Acta* **66,** 3733-3756 (2002).

43 Coogan, L. A. & Gillis, K. M. Evidence that low-temperature oceanic hydrothermal systems play an important role in the silicate-carbonate weathering cycle and long-term climate regulation *Geochemistry, Geophysics, Geosystems* **14,** 1771-1786 (2013).

44 Royer, D., Pagani, M. & Beerling, D. Geobiological constraints on Earth system sensitivity to CO2 during the Cretaceous and Cenozoic *Geobiology* **10,** 298-310 (2012).

45 Park, J. & Royer, D. L. Geologic constraints on the glacial amplification of Phanerozoic climate sensitivity *American Journal of Science* **311,** 1-26 (2011).

46 Royer, D. L. Climate Sensitivity in the Geologic Past *Annual Review of Earth and Planetary Sciences* 277-293 (2016).

47 Hansen, J., Sato, M., Kharecha, P., Beerling, D., Berner, R., Masson-Delmotte, V. *et al.* Target Atmospheric CO2: Where Should Humanity Aim? *Open Atmospheric Science Journal* **2,** 217-231 (2008).

48 Berner, R. A. *The Phanerozoic carbon cycle: CO2 and O2*. (Oxford University Press, 2004).

49 Volk, T. Rise of angiosperms as a factor in long-term climatic cooling *Geology* **17,** 107-110 (1989).

50 Dessert, C., Dupré, B., Gaillardet, J., François, L. M. & Allegre, C. J. Basalt weathering laws and the impact of basalt weathering on the global carbon cycle *Chemical Geology* **202,** 257-273 (2003).

51 Oliva, P., Viers, J. & Dupré, B. Chemical weathering in granitic environments *Chemical Geology* **202,** 225-256 (2003).

52 Bergman, N. M., Lenton, T. M. & Watson, A. J. COPSE: a new model of biogeochemical cycling over Phanerozoic time *American Journal of Science* **304,** 397-437 (2004).

53 Berner, R. A. & Kothavala, Z. GEOCARB III: a revised model of atmospheric CO2 over Phanerozoic time *American Journal of Science* **301,** 182-204 (2001).

54 Van Der Meer, D. G., Zeebe, R. E., van Hinsbergen, D. J., Sluijs, A., Spakman, W. & Torsvik, T. H. Plate tectonic controls on atmospheric CO2 levels since the Triassic *Proceedings of the National Academy of Sciences* **111,** 4380-4385 (2014).

55 Vérard, C., Hochard, C., Baumgartner, P. O., Stampfli, G. M. & Liu, M. Geodynamic evolution of the Earth over the Phanerozoic: Plate tectonic activity and palaeoclimatic indicators *Journal of Palaeogeography* **4,** 167-188 (2015).

56 Cogné, J. P. & Humler, E. Trends and rhythms in global seafloor generation rate *Geochemistry, Geophysics, Geosystems* **7,** (2006).

57 Seton, M., Gaina, C., Müller, R. & Heine, C. Mid-Cretaceous seafloor spreading pulse: Fact or fiction? *Geology* **37,** 687-690 (2009).

58 Hansen, K. W. & Wallmann, K. Cretaceous and Cenozoic evolution of seawater composition, atmospheric O2 and CO2: a model perspective *American Journal of Science* **303,** 94-148 (2003).

59 Müller, R. D., Sdrolias, M., Gaina, C., Steinberger, B. & Heine, C. Long-term sea-level fluctuations driven by ocean basin dynamics *science* **319,** 1357-1362 (2008).

60 Pilson, M. E. *An Introduction to the Chemistry of the Sea*. (Prentice-Hall, Inc., 1998).

61 Hain, M. P., Sigman, D. M., Higgins, J. A. & Haug, G. H. The effects of secular calcium and magnesium concentration changes on the thermodynamics of seawater acid/base chemistry: Implications for Eocene and Cretaceous ocean carbon chemistry and buffering *Global Biogeochemical Cycles* **29,** 517-533 (2015).

62 Hemming, N. G. & Hönisch, B. Chapter Seventeen Boron Isotopes in Marine Carbonate Sediments and the pH of the Ocean *Developments in Marine Geology* **1,** 717-734 (2007).

63 Takahashi, T., Sutherland, S. C., Chipman, D. W., Goddard, J. G., Ho, C., Newberger, T. *et al.* Climatological distributions of pH, pCO 2, total CO 2, alkalinity, and CaCO 3 saturation in the

global surface ocean, and temporal changes at selected locations *Marine Chemistry* **164,** 95-125 (2014).

64 Wang, Y., Huang, C., Sun, B., Quan, C., Wu, J. & Lin, Z. Paleo-CO 2 variation trends and the Cretaceous greenhouse climate *Earth-Science Reviews* **129,** 136-147 (2014).

65 Breecker, D., Sharp, Z. & McFadden, L. Atmospheric CO2 concentrations during ancient greenhouse climates were similar to those predicted for AD 2100 *Proceedings of the National Academy of Sciences* **107,** 576-580 (2010).

66 McElwain, J. C., Montañez, I., White, J. D., Wilson, J. P. & Yiotis, C. Was atmospheric CO 2 capped at 1000ppm over the past 300 million years? *Palaeogeography, Palaeoclimatology, Palaeoecology* **441,** 653-658 (2016).

67 Huber, B. T., Norris, R. D. & MacLeod, K. G. Deep-sea paleotemperature record of extreme warmth during the Cretaceous *Geology* **30,** 123-126 (2002).

68 Hay, W. W. & Floegel, S. New thoughts about the Cretaceous climate and oceans *Earth-Science Reviews* **115,** 262-272 (2012).

69 Frakes, L. A. Estimating the global thermal state from Cretaceous sea surface and continental temperature data *SPECIAL PAPERS-GEOLOGICAL SOCIETY OF AMERICA* 49-58 (1999).

70 Frakes, L. A., Probst, J.-L. & Ludwig, W. Latitudinal distribution of paleotemperature on land and sea from early Cretaceous to middle Miocene *Sciences de la terre et des planètes (Comptes rendus de l'Académie des sciences)* **318,** 1209-1218 (1994).

71 Li, L. & Keller, G. Variability in Late Cretaceous climate and deep waters: evidence from stable isotopes *Marine Geology* **161,** 171-190 (1999).

72 Jansen, H., Zeebe, R. E. & Wolf-Gladrow, D. A. Modeling the dissolution of settling CaCO3 in the ocean *Global Biogeochemical Cycles* **16,** (2002).

73 Gillis, K. & Coogan, L. Secular variation in carbon uptake into the ocean crust *Earth and Planetary Science Letters* **302,** 385-392 (2011).

74 Mills, B., Daines, S. J. & Lenton, T. M. Changing tectonic controls on the long-term carbon cycle from Mesozoic to present *Geochemistry, Geophysics, Geosystems* **15,** 4866-4884 (2014).

75 Li, G. & Elderfield, H. Evolution of carbon cycle over the past 100 million years *Geochimica et Cosmochimica Acta* **103,** 11-25 (2013).

76 von Strandmann, P. A. P., Burton, K. W., Opfergelt, S., Eiríksdóttir, E. S., Murphy, M. J., Einarsson, A. *et al.* The effect of hydrothermal spring weathering processes and primary productivity on lithium isotopes: Lake Myvatn, Iceland *Chemical Geology* (2016).

77 von Strandmann, P. A. P. & Henderson, G. M. The Li isotope response to mountain uplift *Geology* **43,** 67-70 (2015).

78 Wanner, C., Sonnenthal, E. L. & Liu, X.-M. Seawater δ 7 Li: A direct proxy for global CO 2 consumption by continental silicate weathering? *Chemical Geology* **381,** 154-167 (2014).

79 MacKay, D. J. *Information theory, inference and learning algorithms*. (Cambridge university press, 2003).

80 Foreman-Mackey, D., Hogg, D. W., Lang, D. & Goodman, J. emcee: the MCMC hammer *Publications of the Astronomical Society of the Pacific* **125,** 306 (2013).

81 Royer, D. L., Berner, R. A. & Park, J. Climate sensitivity constrained by CO2 concentrations over the past 420 million years *Nature* **446,** 530-532 (2007).

82 Berner, R. A. GEOCARBSULF: a combined model for Phanerozoic atmospheric O 2 and CO 2 *Geochimica et Cosmochimica Acta* **70,** 5653-5664 (2006).